2020

ELECTROSTATIC FOCUSING AND IMPACT CONSOLIDATION OF AEROSOL PARTICLES

Rayhan Ahmed

ELECTROSTATIC FOCUSING AND IMPACT CONSOLIDATION OF AEROSOL PARTICLES

by

Rayhan Ahmed

A Dissertation

Submitted in Partial Fulfilment of the

Requirements for the Degree of

Doctor of Philosophy

Major: Engineering

The University of Memphis

May 2020

Dedication

I would like to dedicate my dissertation to my beloved parents and my wife.

Acknowledgments

I am forever in debt to my advisor, professor Ranganathan Gopalakrishnan for his fundamental role in my doctoral work as well as his supporting role in building up my life. To me, Ranga has always been a great mentor, a supportive instructor, and an outstanding team leader. He gave me the freedom to do whatever I wanted, at the same time continued to contribute valuable feedback, advice, and encouragement. In addition, I greatly value the close personal rapport we have during this tenure. I quite simply cannot imagine a better advisor.

I would like to thank my committee members Professor John I. Hochstein, Professor Jeffrey G. Marchetta, Professor Sanjay R. Mishra, and Professor Thang Ba Hoang for their time and valuable suggestions during my graduate studies. Under the direct guidance of Dr. Hochstein and Dr. Marchetta, I learned a lot and improved my fluid dynamic knowledge to a great extent. I learned about material characterization with the help of Dr. Mishra and Dr. Hoang. Thanks again to Dr. Mishra for allowing me to use his lab facility.

A part of my work involves material characterization using Scanning Electron Microscopy (SEM). I am very much grateful and would like to say thanks to Dr. Felio A Perez and Dr. Omar Skalli for their time and for giving me training and instructions in using SEM facilities.

I would like to express my gratitude to the machine shop technicians, Barry Craig Wymore and Jason Scott Presley, for their intense support and guidance tin developing my experimental setup. Barry is very friendly and always gave me support beyond my expectations.

I feel very much lucky to have some very friendly lab mates and colleagues. My life would be tough without their bountiful support throughout my graduate life. Special thanks to Vikram, Li Li, Prashant, Lekhnath, Ewe Jiun, Nadim, Alireza, Behzad, and Deepa.

Special thanks go to my wife, Sharmin, who always encouraged and supported me throughout this journey. I Thank my other family members who always tried to make me focused. In addition, I am blessed with the support and love from my friends in Memphis, who made my life easy. Thanks to my friends and seniors, Nadim, Faruk, Sultan, Salam, Mahfuz, Milu, Rakib, Ashek, and many others.

Abstract

Aerosol systems play a vital role in controlling the global environment, ecology and biodiversity. Engineering applications of aerosol, such as drug delivery, mass spectrometry, aerosol jet printing, and some others, evolve to understand the importance of aerosol in nature and to replicate the natural benefit of aerosol in engineering products. With the advancement of science and technology, aerosol research is progressing in terms of its better characterization and application in different fields. This dissertation addresses three specific engineering applications of aerosol particles – focusing of aerosol-based nanoparticles, aerosol generation from powder phase materials, and application of TiO_2 aerosol for thin-film fabrication. The first part of the dissertation proposes a new method of focusing aerosol-based nanoparticles through a computational study that would help to break the Brownian diffusion limit of particle focusing as well as to obtain a highly collimated beam of nanoparticles. In the second part of the dissertation, a novel concept of aerosol generation method from powder phase materials has been experimentally evaluated, some modifications and suggestions have been made to establish the concept of aerosolization into a product. This aerosol generation method is scalable and can be used to obtain a high yet tunable concentration of aerosol from powder phase materials. In addition, this method also offers better particle de-agglomeration. The last part of the dissertation presents an experimental study in conjunction with computational analysis to understand and optimize the critical parameters of the TiO_2 thin film fabrication process on glass substrate using aerosol impact consolidation method. It was observed that although repeated coating initially builds up the thickness of the film, however, there is a point of diminishing returns at which continued attempts at deposition starts to erode and can even completely remove the film afterwards. Also, the study reveals the effect of chamber pressure and nozzle geometry on the deposition performance.

TABLE OF CONTENTS

List of Figures viii
Introduction 1
Computational study of electrostatic focusing of aerosol nanoparticles using an einzel lens 8
Abstract 8
Introduction 9
Computational Methods 14
Electrostatic potential in the einzel lens: 14
Particle trajectory simulations in vacuum ($\boldsymbol{P} = \boldsymbol{0}$): 15
Particle trajectory simulations at finite pressure ($\boldsymbol{P} \neq \boldsymbol{0}$): 17
Results and Discussion 21
Effect of $\boldsymbol{\chi e}$ and $\boldsymbol{Bo}$ on particle focusing in vacuum: 21
Constraints in particle focusing using single einzel lens: 26
Effect of finite pressure on particle focusing: 29
Conclusions 43
Scalable High Concentration Aerosol from Commercial Powders 45
Abstract 45
Introduction 46
Experimental Methods 50
Ultrasonic Aerosol Generator (UAG) setup: 50
Aerosol dilution, deagglomeration and measurement setup: 52
Materials: 54
Results and Discussion 55
Scalable steady aerosol concentration: 55
Particle size classification and deagglomeration: 59
Conclusions 62
Fabrication of thin TiO_2 film on glass substrate: an exploratory research 64
Abstract 64
Introduction 65
Experimental Methodology - Powder preparation 67
Particle size growth by sintering 68

Particle agglomeration and deagglomeration 70
Experimental setup and procedure 72
Basic experimental setup: 73
Numerical investigation of Nozzle and chamber pressure 75
Results 81
Coating of TiO2 on glass: 81
Effect of deposition chamber pressure: 85
Addition of virtual impactor: 85
Effect of multiple layering: 88
Micro scratch resistance testing: 90
Conclusions 93
Conclusions 95
References 97

List of Figures

Figure 1:Particle beam width measured after aerodynamic lens for various sizes of DOS particles and lens configuration. Reprinted from Liu et al. (1995)..... 6

Figure 2: A) Schematic representation of the einzel lens geometry (**not to scale**) and the simulation domain considered in this study. B) & C) Schematic representation of the particle trajectories and definitions of influential focusing parameters..... 21

Figure 3: Calculated particle trajectories in vacuum A) $\chi e = 0.01$ B) $\chi e = 0.2$ C) $\chi e = 0.3$ D) $\chi e = 1$..... 23

Figure 4: Reproduced with permission from the publisher from Chapter 2.2 ELECTROSTATIC LENSES by K.-J. Hanszen and R. Lauer. Original caption: Particle trajectory and positions of the image side focal and principal points of an electrostatic single lens accordin according to Heise and Rang (1949). The electrical excitation increases from Fig. 2a to Fig. 2d (a, b first operating range, c second range, d third range). ..." 25

Figure 5: Calculated particle trajectories in vacuum for A) χ_e=3 B) χ_e=4 C) χ_e=10 D) χ_e=275..... 26

Figure 6: A) Variation of focal length with χ_e. B) Effect of initial radial distance Bo on focal length for various χ_e..... 27

Figure 7: A) Spherical aberration as a function of the initial radial distance Bo for various χe. B) The maximum spherical aberration ($\Delta rmax$ corresponding to $Bo = 1$) as a function χe. C) Divergence angle as a function of Bo for various χe. D) The maximum spherical aberration ($\alpha o, max$ corresponding to $Bo = 1$) as a function χe..... 29

Figure 8: Calculated trajectories of 10 nm gold particles ($\chi e = 0.3$) at various pressures 0.001 – 100 Pa using Henderson correlation (top panels) and Langevin equation (bottom panels) with pressure noted above each panel. 35

Figure 9: Calculated trajectories of 50 nm gold particles ($\chi e = 0.3$) at various pressures 0.001 – 200 Pa using Henderson correlation (top panels) and Langevin equation (bottom panels) with pressure noted above each panel. 36

Figure 10: Calculated trajectories of 100 nm gold particles $\chi e = 0.3$) at various pressures 0.001 – 400 Pa using Henderson correlation (top panels) and Langevin equation (bottom panels) with pressure noted above each panel. An additional case of trajectories in a vacuum is also presented for comparison. 37

Figure 11: A comparison of the calculated focal length from Henderson's correlation and Langevin equation for different Knudsen numbers. 38

Figure 12: A) Variation of calculated average focal length with particle Knudsen number Knp (or gas pressure) for different χe. B) A comparison of the variation in average focal length with particle Knudsen number Knp (or gas pressure) for particles of different materials and sizes at $\chi e = 0.4$ 39

Figure 13: A) Effect of particle Knudsen number Knp (or gas pressure) on the maximum spherical aberration for various χe.. B) Effect of particle Knudsen number Knp (or gas pressure) on the maximum divergence angle for various χe. 40

Figure 14: Schematic representation of the modified Ultrasonic Aerosol Generation system 52

Figure 15: Schematic diagram of dilution, deagglomeration and measurement setup 54

Figure 16: SEM image and size distribution of the raw TiO_2 Powder 55

Figure 17: (a)&(b) Aerosol number and mass concentration, respectively, measured at OPS. Each scan was averaged over 15 seconds runtime. Data presented here is for 1hr and 15 minutes runtime; (c) Aerosol concentration measured using CPC for both raw and milled powder where each measurement window is for 5 minutes only. 57

Figure 18: (a) SEM image of the milled powder and (b) size distribution of powders milled for different durations. 59

Figure 19: (a) Particles collected from the diluted gas-phase aerosol before going to OPS and DMA. (b) Particle size distribution in figure (a). (c) Lognormal distribution of particle sizes from OPS measurement. 60

Figure 20: (a) Mobility size distribution from DMA; (b),(c)&(d) SEM image of mobility classified 100 nm, 200 nm & 300 nm particles collected after DMA. 62

Figure 21: 100 nm TiO_2 heated at different temperatures for 8 hrs at ambient air 69

Figure 22: Normal distribution of TiO_2 particles after sintering for 8 hours at different temperatures 70

Figure 23: SEM image of sintered TiO_2 particles at 1100 ^oC for 8 hrs 71

Figure 24: Effect of ball milling on powder preparation. a) SEM image of 8hrs ball-milled powder at 250 rpm, b) Mean size of particles with number of hours at two different rpm, c) particle size ranges with ball milling time for 250 rpm d) particle size ranges with ball milling time for 450 rpm 72

Figure 25: Schematic diagram of the experimental setup for aerosol deposition 74

Figure 26: Slit and Slit CD nozzle boundary conditions and velocity contours 79

Figure 27: Gas and particle velocity for Slit CD nozzle 80

Figure 28: Particle impinging velocities at the substrate for different chamber pressure 81

Figure 29: TiO_2 coated glass substrates 83

Figure 30: Cross-sectional image of the TiO_2 Coating on a glass substrate 83

Figure 31: Top view of coating and XRD results 84

Figure 32: Surface roughness of coating measured by digital microscope 84

Figure 33: Thin film of TiO_2 developed under various chamber pressure. Here chamber pressure varied from 650 to 7000 Pa 85

Figure 34: Schematic diagram of the virtual impactor 87

Figure 35: SEM images of particles collected before after and from virtual impactor 87

Figure 36: TiO_2 film on glass substrate with and without virtual impactor 88

Figure 37: Images of TiO_2 thin films for a different number of passes. 89

Figure 38: Film thickness vs. number of passes 89

Introduction

'Aerosol', suspension of solid and/or liquid particles in a gas, is an integral part of the Earth's 4 spheres (Atmosphere, Biosphere, Hydrosphere, and Lithosphere) (Cao 2017). Hence, aerosol science and engineering have wide application areas ranging from environment, energy to health industries (Ren-Jian, Kin-Fai et al. 2012, Wang, Hsu et al. 2020). Aerosol measurement (McMurry 2000) and characterization (Core 1991, Johnston and Kerecman 2019), and aerosol based additive manufacturing (Wilkinson, Smith et al. 2019) are the most widely used aerosol engineered systems. Focusing of aerosol into a tight beam is an integral part of both aerosol measurement and aerosol-based additive manufacturing process (Ziemann, Kittelson et al. 1995, Pan, Kalume et al. 2018). Moreover, aerosol based direct write manufacturing methods such as aerosol jet printing (Secor 2018) and aerosol deposition method (Lee, Cho et al. 2019) are promising for additive manufacturing of thin films and 3D structures.

The ever-increasing need for aerosol measurement and analysis is pushing the demand for highly precise and sophisticated instruments for aerosol measurements. For example, mass spectrometry (Awad, Khamis et al. 2015), aerosol jet printing, and micro-patterning require a highly collimated beam of particles(Hoey, Lutfurakhmanov et al. 2012). However, due to the thermodynamic diffusion properties of aerosolized nanoparticles it is very difficult to reduce the aerosol beam width below a certain limit, which is termed as Brownian limit of particle focusing(Ziemann, Kittelson et al. 1995).

On the other hand, the aerosol-based direct-write technology has enormous potential for manufacturing 3D microstructures and thin film fabrication because of its ease of operation and environment-friendly manufacturing process. Among aerosol-based direct-write methods aerosol deposition method (AD) (Akedo, Ichiki et al. 1998) is widely recognized for fabricating thin

ceramic films at room temperature. In AD nano and micron-size particles are accelerated through nozzles and impacted on a surface placed in a vacuum chamber to form thin films on the surface. In addition to the room temperature manufacturing benefit, the method is also attractive because it is etching free, solvent-free, requires minimal or no post heat treatment and reportedly attains higher bonding strength between the substrate and the film. The one-step room temperature deposition method makes AD more popular for fabricating thin ceramic films as the conventional ceramic film fabrication techniques require either very high heat involvement or chemical reaction which limit the methods to use for non-metallic substrates (Hanft, Exner et al. 2015).

Ceramic coatings have broad application areas from semiconductors to biomedical industries.(Wang, Lee et al. 2006, Kim, Hahn et al. 2011, Schubert, Hanft et al. 2019). For instance, ceramic thin film of Titanium dioxide (TiO_2) has wide applications because of its photocatalytic and photochromic properties, and have been in use as antibacterial coating, solar cell and decomposing organic substances (Evtushenko, Romashkin et al. 2015). Conventional methods of fabricating TiO_2 thin film either involve expensive chemical reactions or high heat involvement and attains a low substrate to film bonding strength. However, the fabrication of TiO_2 thin film by AD reportedly attains higher bonding strength and is a solvent free, chemical reaction free room temperature deposition method. Although the method has several advantages over the conventional thin-film fabrication process, however, this method needs optimization of the several process flow parameters and needs further research to standardize the manufacturing method.

While aerosol-based manufacturing methods are getting high demand, therefore it is also necessary to look at the aerosol generation methods. A tunable and stable supply of high concentration aerosol is a precursor for the aerosol-based manufacturing process. Aerosol generation from powder phase materials is most attractive for AD because of its availability and simplicity to use in pure form. Conventional techniques of generating aerosol from powder phase materials uses fluidized bed and vibration, which often suffers from high agglomeration and poor control over generated aerosol(Tiwari, Fields et al. 2013). There are some non-contact-based aerosol generators such as ultrasonic aerosol disperser which uses ultrasonic waves for levitating powder particles from the powder bed and makes aerosol (Dunst, Bornmann et al. 2018, Pokharel, Parajuli et al. 2019). This method is potential over the conventional methods for better control over the concentration and scalability.

Based on the generation of aerosol, focusing of aerosol particles and application of aerosol for thin-film fabrication, the key objectives of this research include -

1) Introduction of a new focusing method that has the potential to overcome the Brownian diffusion limit of particle focusing.
2) Development of an aerosol generator which would have better control over supplied aerosol and could be scalable to any size for industrial production.
3) A brief introduction of the aerosol deposition method and a detailed study of the process parameters and their limitations for fabricating thin ceramic films of TiO_2 on a glass substrate.

The remainder of the introduction discusses the shortcomings of the existing methods for focusing, aerosol generation and the aerosol deposition method that worked as a motivation for this thesis.

The pioneering research on ‘Aerosol’ was started at the hand of John Aitken (Aitken 1881). However, the focusing of aerosol was explored after around 80 years by Murphy and Sears (Murphy and Sears 1964). The initial idea of focusing was the use of a capillary tube to experimentally analyze the particle beam contraction. Between the 1970s and 1990s several theoretical works enriched the fluid dynamic analysis of focusing devices (De La Mora and Riesco-Chueca 1988) and also some new methods of focusing evolved such as sheath flow (Dahneke and Flachsbart 1972). After the 1990’s the breakthrough in aerosol particle focusing occurred through the invention of the Aerodynamic lens by Peng Liu (Ziemann, Kittelson et al. 1995). Aerodynamic lens is a series of concentric orifices connected to each other with a spacer in between them. While aerosol passes through those orifices particles gets closer to the axis of the orifices due to the particle inertia. Aerodynamic lens has been successfully applied in many devices including, mass spectrometry and nanopatterning.

Nanoparticles are very small and undergo Brownian diffusion. Due to Brownian diffusion particle gets random movement with a random kinetic energy which a function of the thermal energy of that system. It was observed that the final beam width by the aerodynamic lens is limited by Brownian diffusion (Ziemann, Kittelson et al. 1995).

Figure 1: Particle beam width measured after aerodynamic lens for various sizes of DOS particles and lens configuration. Reprinted from Liu et al. (1995)

represents the final beam width for dioctyl sebacate particles after passing through the aerodynamic lens. The solid black line represents the Brownian limit of beam width based on the particle diameter. From

Figure 1: Particle beam width measured after aerodynamic lens for various sizes of DOS particles and lens configuration. Reprinted from Liu et al. (1995)

it can be observed that none of the lens configuration and particle size combination crossed the Brownian diffusional limit. To overcome this limitation, a new focusing mechanism has been proposed a based-on electrostatics and aerodynamics. 0 of this dissertation describes the new particle focusing mechanism in detail.

The application of aerosol requires the production of aerosol within the application facility. This gave an opportunity to develop an aerosol generate aerosol at our facility. Despite of having several methods available for generating aerosol, this dissertation will only focus on describing the dry dispersion of aerosol particles. Aerosol generated from commercially available power phase materials offers a great benefit over aerosol generated from gas phase particle synthesize in respect to the control over particle size ranges, better control on centration and scalability. Conventional methods of generating aerosol from powder phase materials are - use of fluidized beds with/without vibrating plates (Prenni, Siefert et al. 2000), fluidized nozzles and/or rotating brushes (Ding and Riediker 2016, Schubert, Hanft et al. 2019). All of these contact-based methods sometimes cause re-agglomeration of particles and settles as a compacted layer in the aerosol bed and needs a constant feeder unit in order to keep the generation steady. On the other hand, an ultrasonic aerosol generator, a new concept of generating aerosol from powder phase materials, is a very promising method of generating aerosol which uses ultrasonic standing waves to levitate powder particles from powder bed and generate aerosol. This method benefits

over the vibrating plate in terms of better de-agglomeration of particles and doesn't need a constant feeder unit to keep up the concentration. However, the method needs more optimization and control to make a steady source of aerosol which gives the motivation of this study. 0 of this dissertation describes in detail the design and analysis of the remodeled ultrasonic aerosol generator.

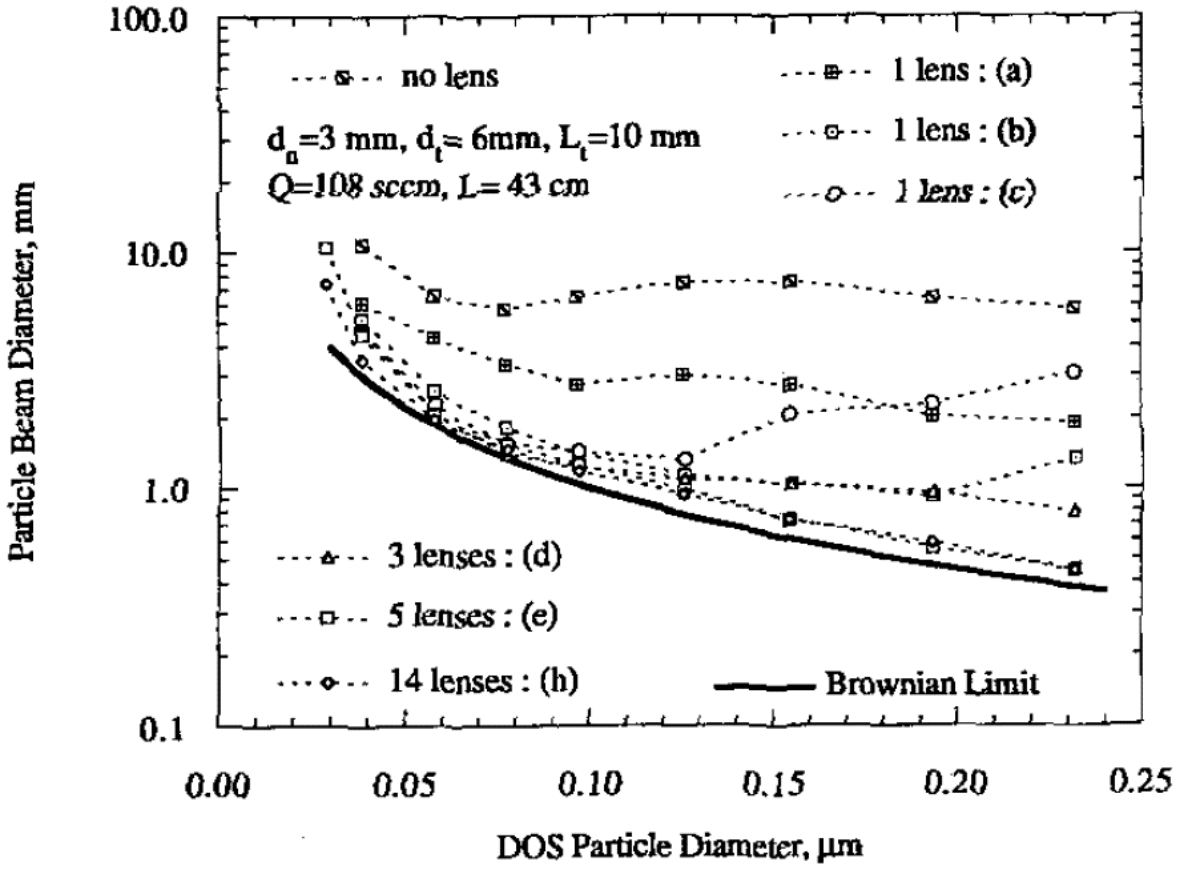

Figure 1: Particle beam width measured after aerodynamic lens for various sizes of DOS particles and lens configuration. Reprinted from Liu et al. (1995)

Aerosol based direct-write technology got much favored over other contemporary techniques because of its ease of operation and one-step fabrication process. As such, the Aerosol

Deposition method (AD) gained a lot of attention because of its one-step fabrication process of ceramic coatings. Although the aerosol deposition method evolved in 1980's however the method has yet to be commercialized, and maximum research is lab-scale and the majority of the works area based on some specific geographic region (Hanft, Exner et al. 2015). Although there are a good number of research articles on these AD methods; however, none of them have a solid conclusion about the tunable parameters to get an optimum coating, which is the main motivation of this study. In addition, although there is a high potential of TiO_2 thin film, however, there are few researches on the fabrication of thin TiO_2 film using AD (Chun, Kim et al. 2008, Ryu, Hahn et al. 2010, Buesser, Gröhn et al. 2011, Yuuki, Uemichi et al. 2013). Therefore, this study is based on the exploration of the critical parameters in fabricating TiO_2 thin film on glass substrate using AD process. The 4^{th} chapter of this dissertation describes the critical parameters of the AD process to fabricate thin TiO_2 film and shares some parametric analysis.

The last chapter of this dissertation summarizes all the new proposals and findings in this study and gives an indication of future research works.

Computational study of electrostatic focusing of aerosol nanoparticles using an einzel lens

Abstract

This study computationally explores the possibility of focusing charged aerosol nanoparticles using electrostatics, similar to focusing of electrons and ions. A non-dimensional electrostatic focusing parameter χ_e, defined as the ratio of electrostatic potential energy to the kinetic energy of an aerosol nanoparticle, significantly determines focusing performance. The focusing device considered here is a 3-electrode electrostatic ("einzel") lens. The average focal length of the lens is seen to have an inverse power relationship with χ_e. For low values of χ_e ~ 3 in this study, the particles are seen to cross the lens axis once, while at higher χ_e multiple axis cross-over points appear. Similar to electron and ion optics, nanoparticle focusing is also limited by spherical aberration and beam divergence due to finite spread of particles in the inlet cross section of the lens and spatial non-uniformity of the focusing electric field. Other factors that influence focusing performance such as the electrostatic lens geometry, and the distribution of velocity and kinetic energy of the particles at the inlet of the lensing region are recognized, but not considered here for simplicity. In vacuum, good focusing performance (i.e.) a narrow beam of nanoparticles with minimum spherical aberration and small divergence angle is theoretically possible if χ_e<1 and if spread of particles in the inlet is confined to 20% of radius of the cylindrical lens. The effect of gas pressure is also probed to understand the degradation of focusing performance due to particle-gas interactions. It is seen that, for particles of specified size and density, a certain maximum pressure exists beyond which the device can no longer be efficiently used to focus nanoparticles. Likewise, below a certain pressure, the focusing performance is nearly independent of gas pressure, thereby enabling the selection of an operating pressure for such devices.

Introduction

Focusing of aerosol (gas-phase) nanoparticles into narrow beams is motivated by applications in aerosol mass spectrometry (Schreiner, Schild et al. (1999), Huffman, Jayne et al. (2005), Deng, Zhang et al. (2008)), particle jet printing applications (Lin, Cole et al. 2010, Tse and Barton 2015), micro-patterning (Di Fonzo, Gidwani et al. 2000, Dong, Bapat et al. 2004, Qi, McMurry et al. 2010),, and the fabrication of three-dimensional microstructures (Akedo, Ichiki et al. 1998). Murphy and Sears (1964) pioneered the generation of aerosol particle beams by flowing particles through a series of capillaries, later adopted by others (Hall and Beeman 1976, Allen and Gould 1981, Seapan, Selman et al. 1982, Sinha and Friedlander 1986, Kievit, Marijnissen et al. 1992). Although experimentally demonstrated, this method was not supported by analysis of particle motion to enable the systematic design of such focusing devices. Alternative to vacuum focusing is the use of sheath gas flow to confine particle beams to narrow cross sections by limiting their transverse diffusional broadening. While the sheath flow reduces the beam diameter effectively by a factor of ~10 (Dahneke and Flachsbart 1972, Dahneke and Cheng 1979), it also dilutes the particle concentration leading to decreased particle detection sensitivity for mass spectrometry or low throughput for patterning applications.

To overcome the difficulties associated with the sheath gas and to obtain higher aerosol transport efficacy than capillaries, Liu, Ziemann et al. (1995) designed the aerodynamic lens that consists of a series of contractions and expansions of flow cross section achieved by the use of orifice plates. For a particle-laden flow, the aerodynamic lens provides the same focusing effect as sheath air without additional gas handling. The aerodynamic focusing of particles is based on their propensity to move towards the centerline of an axisymmetric flow when moving through successive contractions and expansions (Robinson 1956), provided their inertia is less than the critical inertia to avoid collision with the walls of the flow tube (Hinds 2012). Prior to Liu et al.,

Fernandez De La Mora and Riesco-Chueca (2006) showed that particle inertia (described by a Stokes number that compares particle relaxation time to the fluid advection time scale) leads to focusing of particles onto a single spot and a crossover point on the axis of a flow. Their conclusions were drawn from calculated trajectories of particles in an incompressible flow through a nozzle, with Brownian motion neglected. The computational investigation described in this paper draws inspiration from Fernandez de la Mora's approach of quantifying focusing outcomes as well as the calculation of trajectories with one-way coupling to an advection field (Fernandez de la Mora 2006, Fernandez De La Mora and Riesco-Chueca 2006) – in that work, incompressible flow field was employed, while we investigate the effect of electrostatic field in vacuum and at finite pressures (without a systematic fluid flow field). The minimum beam width achieved using the inertial focusing method of Liu, Ziemann et al. (1995) approaches ~0.4 mm, that increases with decreasing particle size as demonstrated using spherical dioctyl sebacate particles in the range of ~50 – 250 nm (Liu, Ziemann et al. 1995). Several designs of aerodynamic lenses have been used to effectively collimate nanoparticles in the range of 100–900 nm (Schreiner, Schild et al. 1999), 340–4000 nm (Schreiner, Voigt et al. 1998), 60–600 nm (Zhang, Smith et al. 2004), 3–30 nm (Wang, Kruis et al. 2005), 30–300 nm (Lee, Cho et al. 2008), 5–50 nm (Lee, Kim et al. 2009) and 30 nm–10 μm (Lee, Hwang et al. 2013). The beam width produced by this method is limited by Brownian motion and lift forces on the particles during expansion through the orifices and the exit nozzle of the lens. Overcoming the Brownian limit of beam broadening is theoretically impossible without the application of radial forces by external means (such as electric fields for example). Thus, reduction of beam width beyond those achieved by the aerodynamic lens has been challenging and has not been accomplished so far.

Alternate to the inertial particle focusing mechanism of the aerodynamic lens, several attempts have been made to use electrostatic and electrodynamic forces or a combination of both fluid and electric forces to focus particles. Electron and ion focusing devices using applied electric fields have been harnessed for many applications such as electron microscopes, cathode ray tubes, ion beam milling apparatus and drift tube mobility spectrometry (Fernández-Maestre 2012, Cumeras, Figueras et al. 2015, Oberreit and Hogan Jr 2015). The ion/electron trajectories in these devices are manipulated using a series of ring/planar electrodes with an applied voltage gradient to confine them to a narrow region around the axis. The analogous use of electric fields to focus aerosol nanoparticles could potentially mitigate beam broadening by Brownian motion and be instrumental in producing narrow beams than is currently possible using inertial focusing alone. The charge and electrical mobility (which is dependent on the gas pressure) of particles determine their response to an applied electric field. Electric fields have been used numerously to manipulate the trajectories of aerosol particles for measurement and patterning. Knutson and Whitby (1975) developed the differential mobility analyzer that spatially separates particles based on their electrical mobility or size (for spheres). The experimental verification Liu, Ziemann et al. (1995)'s design of aerodynamic lens (Liu, Ziemann et al. 1995) used electrostatic fields to deflect charged particles to measure their nominal velocity in a focused beam. Kane et al. (2001) used an electrostatic lens to concentrate nanoparticles before introducing into the time-of-flight detector of a mass spectrometer for improved sensitivity. They have observed that electrostatic focusing increases the hit rate (sensitivity) by increasing the overlap of the laser beam with the particle beam. The deposition of charged nanoparticles (<5 nm) of diverse materials using photoresists (for selective area deposition) and external biasing of voltages has enable the creation of nano-patterns and are successful demonstrations of the utility of electric

fields to control particle motion advantageously (Krinke, Deppert et al. 2002, Kim, Kim et al. 2006, You and Choi 2007, Lin, Cole et al. 2010, You, Han et al. 2010, Park, Jeong et al. 2013, Choi, Kang et al. 2015).

Masuda et al. (1972) used a set of parallel cylindrical electrodes, separated by insulating spacers and connected to an alternating voltage source that produced a spatially periodic electric field in the focusing region. Charged aerosol particles were shown to have periodic motion along the curved lines of force and were repulsed from the electrode due to the action of centrifugal force and electric force. Based on the different electrode configurations, the particles can either levitate or levitate and accelerate simultaneously along the lens axis. Based on the same methodology, Holm and Addison (1991) designed a cone frustum shaped screen having an entrance and exit diameter of 7.0 cm and 2.5 cm respectively with a length of 17.0 cm for electrodynamic focusing of charged particles and achieved minimum beam width ~ 1 mm. They have observed that 5.2 μm particles could be focused to ~2 – 4 mm beam widths for electric elementary charges of 2000 to 6000, positive or negative charges on the particles. As aerosol particles are much heavier and have lower velocities than electrons and ions, it is conceivable that they require considerably higher number of electric charges to respond to the applied field ($\vec{F} = q\vec{E}$).

Heise and Rang (1949) have used a simple 3-electrode einzel lens to focus electron beams experimentally, analogous to light. An einzel lens is made of three ring electrodes (separated by insulating spacers), with the first and third electrodes held at the same voltage (and of the same length) while the second electrode is held at a different voltage to create a voltage gradient for focusing. The numerical calculations of electron focusing using einzel lenses that relate the focal length and the operating parameters (voltage and geometry) developed by Adams

and Read (1972) have been used numerously to design charged particle focusing devices (Odenthal 1991, Chang, Thomson et al. 1996). Computational studies have been used to understand electrostatic particle deposition and inspires our use of trajectory simulations to parameterize focusing using electrostatic fields (Rusinque, Fedianina et al. 2019). A systematic exploration of the motion of charged nanoparticles particles to understand electrostatic focusing using a cylindrical einzel lens with a simple 3-electrode geometry is carried out in this study. Motivated by ion and electron focusing using einzel lenses, it is desirable to deduce the operating parameters (particle velocity and charge, strength of electric fields and gas pressure) for successful focusing of nano- and micro-particles beyond the Brownian diffusion limit. This study, using trajectory simulations, computationally explores the electrostatic focusing of aerosol nanoparticles to understand the effect of particle parameters (material, kinetic energy/velocity, size, number of charges), lens geometry, operating voltage/applied electric field and gas pressure on focusing performance (quantified by the focal length, spherical aberration and divergence angle of particle beams). The comparison between the electric potential energy of the particle to kinetic energy determines the ease with which they are deflected towards the lens axis by the applied electric field. The thermal energy of the particles as well as the drag exerted by the gas medium on their motion are also important in determining focusing outcomes. We also identify conditions in which the spherical aberration and divergence angle of the focused beam can be minimized and deduce the upper limit of gas pressure at which an einzel lens acts as a focusing device without significant distortion by collisions between particles and background gas molecules. Lastly, we elucidate qualitative relationships between focal length, spherical aberration and the divergence angle with the ratio of the electric potential energy to the kinetic

energy of the particles, the particle Knudsen number as well as particle diameter and material density.

Computational Methods

Electrostatic potential in the einzel lens:

The electrostatic focusing of nanoparticles using a 3-electrode einzel lens is investigated through particle trajectory simulations. Assuming that the concentration of charged aerosol particles injected into the focusing region is low, the distortion of the electric field by space charge due to the particles is neglected and a one-way coupling is assumed to exist between the electric field due to the einzel lens and particles. The electrostatic potential φ (and the electrostatic field $\vec{E} = -\nabla\varphi$) inside the einzel lens is obtained by solving the Poisson equation, assuming the space charge is zero, using the commercial software COMSOL®:

$$\nabla^2\varphi = 0 \tag{1}$$

Eq. 1 is solved in an axisymmetric einzel lens geometry, shown in **Figure 2-A**, representing a cylindrical einzel lens whose dimensions are expressed in multiples of the radius of the lens R. The lens geometry consists of three cylindrical electrodes of identical radius. The length of the first electrode (L_1) and third (L_3) electrode was chosen to be $4.5R$ by trial and error such that the particles enter and leave the lens under electric field-free conditions $\vec{E} \approx 0$. The length of the second electrode (L_2) is set to $1.5R$ for simplicity. The length of the dielectric spacer between the electrodes δ defines the strength of the electrostatic field existing in the focusing region (Adams and Read 1972, Ciric, Terzic et al. 1976). Although there are multiple choices for δ, we again set $\delta = R$ for simplicity. All results presented in the reminder of this article correspond to these set of geometrical choices to probe the effect of applied voltage, gas pressure and particle parameters (size, density, and incoming velocity). The effect of lens geometry, though important, is not the focus of this computational investigation of electrostatic focusing. The electrostatic

potential φ and electric field $\vec{E}$ components were exported from COMSOL® to particle trajectory simulation routines to investigate focusing in vacuum and at finite gas pressures.

Particle trajectory simulations in vacuum ($\boldsymbol{P = 0}$)*:*
The trajectories of nanoparticles inside the einzel (assumed to be operated in vacuum) are calculated by solving Newton's second law of motion:

$$\frac{d\vec{v}}{dt} = \chi_e \vec{E} \tag{2}$$

Eq. 2 was integrated in time using the velocity-Verlet numerical scheme (Verlet 1967):

$$\vec{x}(t + \Delta t) = \vec{x}(t) + \vec{v}(t)\,\Delta t + \frac{1}{2}\,\chi_e \vec{E}\big(\vec{x}(t)\big)\left(\frac{R}{\delta}\right)\Delta t^2 \tag{3a}$$

$$\vec{v}(t + \Delta t) = \vec{v}(t) + \frac{1}{2}\,\chi_e\left(\vec{E}\big(\vec{x}(t)\big) + \vec{E}\big(\vec{x}(t + \Delta t)\big)\right)\left(\frac{R}{\delta}\right)\Delta t \tag{3b}$$

Here, $\vec{x}(t)$ and $\vec{v}(t)$ are the non-dimensional position and velocity vector of a particle, respectively. All lengths are expressed in multiples of the electrode radius R, while velocities are scaled using U_o, the initial velocity of the particles at the entrance of the einzel lens. $\vec{E}(\vec{x})$ is the non-dimensional electrostatic field obtained by normalizing the electric field exported from COMSOL® (with unit of V/m) by the nominal electric field calculated as $\frac{\Delta V}{\delta}$. Here ΔV is the applied voltage difference across the tube electrodes, $\Delta V = V_1 - V_2 = V_3 - V_2$. $\chi_e \equiv \frac{n_p e \Delta V}{m_p U_o^2}$ is a ratio of the electrostatic potential energy to the initial kinetic energy of the particle carrying n_p units of electronic charge e, of density ρ_p and having a mass of m_p. The particles are assumed to be spherical with a diameter of d_p such that $m_p = \frac{\pi}{6}\rho_p d_p^3$. χ_e compares the electrostatic potential energy of the particles to the kinetic energy (inertia). **Table 1** shows the variation of χ_e as a function of d_p and n_p for different materials. The values of χ_e were calculated considering a particle velocity of $U_o = 100$ m/s and a voltage difference $\Delta V = 1000\ V$ across the electrodes of

the einzel lens. Our choice of 100 m/s is based on the measured exit velocities of particles from focusing devices such as the aerodynamic lens (Liu, Ziemann et al. 1995), that will be presumably used for accelerating and focusing particles that can be further improved using an einzel lens in series. For a 100 nm gold particle, $\chi_e = 0.0016 - 0.1584$ as n_p is varied from 1 – 100. The maximum value of χ_e for a given material and particle size is limited by the charge limit n_L set by the self-generated field strength for spontaneous emission of electrons or positive ions from the particle surface assuming an ion evaporation mechanism (Thomson and Iribarne 1979, Gamero-Castaño and Mora 2000):

$$n_L = \frac{d_p^2 E_L}{4K_E e} \tag{4}$$

E_L is the material-dependent surface field strength required for spontaneous emission of electrons or positively charged ions. Further, the emission field strength is also dependent on the composition of the charge carrier. For electrons, typical values of $E_L \sim 10^8\ V/m$, and for positive charged ions $E_L \sim 10^{10}$ V/m. The electrostatic constant of proportionality $K_E = 9.0 \times 10^9$ Nm^2C^{-2}. The maximum value of χ_e for a 100 nm gold particle is 2.4755 based on the charge limit for gold. Similarly, for the highest value of χ_e for a 10 nm silicon particle is 210.12 based on the corresponding charge limit. Therefore, it is clear that χ_e increases with the inverse of mass to charge ratio of the aerosol nanoparticle. For an electron with a velocity of $\sim 10^7$ m/s and voltage difference of 1000 V across electrodes, $\chi_e \sim 1.76 - 0.0176$ signifies the possibility of focusing particles like electrons and ions by einzel lenses. In results that will be presented in subsequent sections, we probe the effect of χ_e on the focusing performance of the einzel lens in vacuum and at finite gas pressure.

Table 1: Possible range of χ_e values for different combination of variables

Particle diameter d_p (nm)	**Number of charges n_p**	Initial particle velocity $U_o = 100\ m/s$ and voltage difference $\Delta V = 1000\ V$ Electrostatic focusing parameter $\chi_e = \frac{n_p e \Delta V}{m_p U_o^2}$				
		Gold 19320 kg/m^3	**Silver** 10490 kg/m^3	**Copper 8960** kg/m^3	**Germanium** 5323 kg/m^3	**Silicon** 2330 kg/m^3
100	1	0.0016	0.0029	0.0034	0.0057	0.0131
	100	0.1584	0.2917	0.3415	0.5749	1.3133
	Max (1563)	2.4755	4.5593	5.3378	8.9849	20.5265
50	1	0.0127	0.0233	0.0273	0.0460	0.1051
	100	1.2671	2.3336	2.7321	4.5988	10.5062
	Max (391)	4.9542	9.1244	10.6824	17.9813	41.0793
10	1	1.5838	2.9170	3.4151	5.7485	13.1328
	10	15.8382	29.1700	34.1510	57.4851	131.3276
	Max (16)	25.3411	46.6720	54.6416	91.9762	210.1241
χ_e of an electron is ~ 1.76 - 0.0176, for a potential difference of 1000V, velocity ~10^7 m/s						

Particle trajectory simulations at finite pressure ($\boldsymbol{P \neq 0}$)*:*
In addition to electrostatic interactions quantified by χ_e, the finite gas pressure in focusing devices leads to hydrodynamic drag on particles exerted by the gas medium and Brownian motion due to collisions with gas molecules. At low pressures considered here, Brownian motion is neglected. This assumption is justified posteriori by the lack of significant difference between trajectories simulated with and without Brownian motion. Particle trajectory simulations were carried out by solving the non-dimensional equation of motion considering only the hydrodynamic drag and electrostatic force on the particles:

$$\frac{d\vec{v}}{dt} = \chi_e \vec{E} - \frac{3}{4}\frac{C_H\ \rho_g\ \delta\ |\vec{v}|^2}{\rho_p d_p}\frac{\vec{v}}{|\vec{v}|} \tag{5}$$

C_H is the drag coefficient and for subsonic particle velocities, the Henderson correlation (1976) was used:

$$C_H = 24\left[1.77\,\frac{S}{Kn_p} + S\left\{4.33 + \left(\frac{3.65 - 1.53\frac{T_p}{T_g}}{1\ + 0.353\frac{T_p}{T_g}}\right) \times \exp\left(-\frac{0.438}{Kn_p}\right)\right\}\right]^{-1}$$

$$+ \exp\left(-0.447\sqrt{\frac{Ma_p Kn_p}{\gamma^{0.5}}}\right)\left[\frac{4.5Kn_p + 0.38\left(0.053\,S + 0.639\,\sqrt{Kn_p S}\right)}{Kn_p + 0.053\,S + 0.639\sqrt{Kn_p S}}\right.$$

$$\left. + 0.1Ma_p^2 + 0.2Ma_p^8\right] + 0.6S\left[1 - \exp\left(-0.798\frac{Kn_p}{\gamma^{0.5}}\right)\right] \qquad (6)$$

where $Kn_p \equiv \frac{2\lambda_g}{d_p} = \frac{Ma_p}{Re_p}\sqrt{\frac{\gamma\pi}{2}}$ is the Knudsen number of particle, Re_p is the Reynolds number based on particle diameter, $Ma_p = \frac{v_p}{c}$ is the Mach number of the particle defined as particle speed v_p to the speed of sound c, λ_g is the mean free path of the gas molecules, molecular speed ratio $S = Ma_p\sqrt{\gamma/2}$ (γ is the ratio of gas specific heats at constant pressure and constant volume). For the pressures considered here, most of the calculations fall in the free-molecular limit of $Kn_p \to \infty$. Finally, T_p is the particle temperature assumed to be equal to the gas temperature T_g (i.e.) $\frac{T_p}{T_g} = 1$. Eq. 5 was solved considering Henderson's correlation (eq. 6) using a leap-frog variant of the velocity-Verlet method with damping terms to capture the effect of drag:

$$\vec{x}(t + \Delta t) = \vec{x}(t) + \vec{v}(t)\Delta t + \frac{1}{2}\Delta t^2\vec{a}\left(\vec{x}(t), \vec{v}(t)\right) \qquad (7a)$$

$$\vec{v}^I = \vec{v}(t) + \vec{a}\left(\vec{x}(t), \vec{v}(t)\right)\Delta t;\ \vec{a}^I = \vec{a}(\vec{x}(t + \Delta t), \vec{v}^I) \qquad (7b)$$

$$\vec{v}^{II} = \vec{v}(t) + \frac{\left[\vec{a}\left(\vec{x}(t), \vec{v}(t)\right) + \vec{a}^I\right]}{2}\Delta t;\ \vec{a}^{II} = \vec{a}(\vec{x}(t + \Delta t), \vec{v}^{II}) \qquad (7c)$$

$$\vec{v}(t + \Delta t) = \vec{v}(t) + \frac{\left[\vec{a}\left(\vec{x}(t), \vec{v}(t)\right) + \vec{a}^{II}\right]}{2}\Delta t \qquad (7d)$$

where $\vec{a}\left(\vec{x}(t), \vec{v}(t)\right) = \chi_e \vec{E}\left(\vec{x}(t)\right) - \frac{3}{4}\frac{C_H\, \rho_g\, \delta\, |\vec{v}|^2}{\rho_p d_p}\frac{\vec{v}}{|\vec{v}|}$ to include acceleration due to both electrostatic force and hydrodynamic drag force.

Particle trajectory simulations are analyzed in subsequent sections to elucidate electrostatic particle focusing using einzel lenses. For cases considering focusing in vacuum ($P = 0$), equations 3a and 3b were used to obtain particle position and velocity as a function of time. Likewise, equations 7a – 7d were used for finite pressure cases considering drag due to gas molecules and electrostatic force on the particles. **Figure 2-B** illustrates the parameters that influence, and metrics to quantify focusing performance. In the trajectory simulations described in this paper, charged particles are introduced into the simulation domain with a dimensionless velocity of 1.0, parallel to the optic axis. Particle focusing through the einzel lens is like electron/ion optics wherein charged particles respond to the applied electrostatic field and are deflected towards the center line. The "reference plane" shown in **Figure 2-B** is used as the reference datum to measure all lengths subsequently discussed and the center line of the cylindrical electrodes is termed as optic axis. The point of first cross-over on the optic axis is referred to as focal point (analogous to electron/light optics) and the distance of focal point is termed the focal length f_L – the particle trajectories are assumed to be axi-symmetric. The initial radial distance of the particles from the optic axis, B_o at the entrance of the einzel lens is varied from 0 to 1 (measured in multiples of R, the radius of the cylindrical electrode). Throughout this study, the particles at the entrance of the lens are assumed to have a velocity *parallel* to the optic axis - the angle α_i (not shown on **Figure 2-B**) between the initial velocity and the optic axis is set to zero. We elect to focus on quantifying the principal focusing parameters χ_e and B_o and defer the variation of the incoming particle velocity direction α_i to future investigations. As depicted in **Figure 2-C**, the trajectory of a particle starting close to the optic axis is referred to as

the paraxial trajectory ($B_o = 0.005$ in this work). Likewise, the trajectory of a particle starting close to the electrode is referred to as the peripheral trajectory ($B_o = 1$). The angle between a particle trajectory and the optic axis after cross-over is referred to as the divergence angle α_o. The point of cross-over of the paraxial trajectory with the optic axis is the paraxial focal point. The transverse spherical aberration Δr is the radial distance of a particle measured in the plane of the paraxial focal point. The effect of χ_e and B_o on focusing performance quantified by focal length f_L, divergence angle α_o and the transverse spherical aberration Δr is investigated computationally in the reminder of this paper. The charged particles are assumed to be dilute in concentration inside the einzel lens – hence, all particle-particle interactions are neglected in considering their trajectories through the lensing region and at the point of cross-over. We note that the electrostatic repulsion between like-charged particles will restrict their focusing onto a single point and will cause a finite focal volume through which all the particles nominally pass through. In this investigation, we also elect to ignore this effect for simplicity.

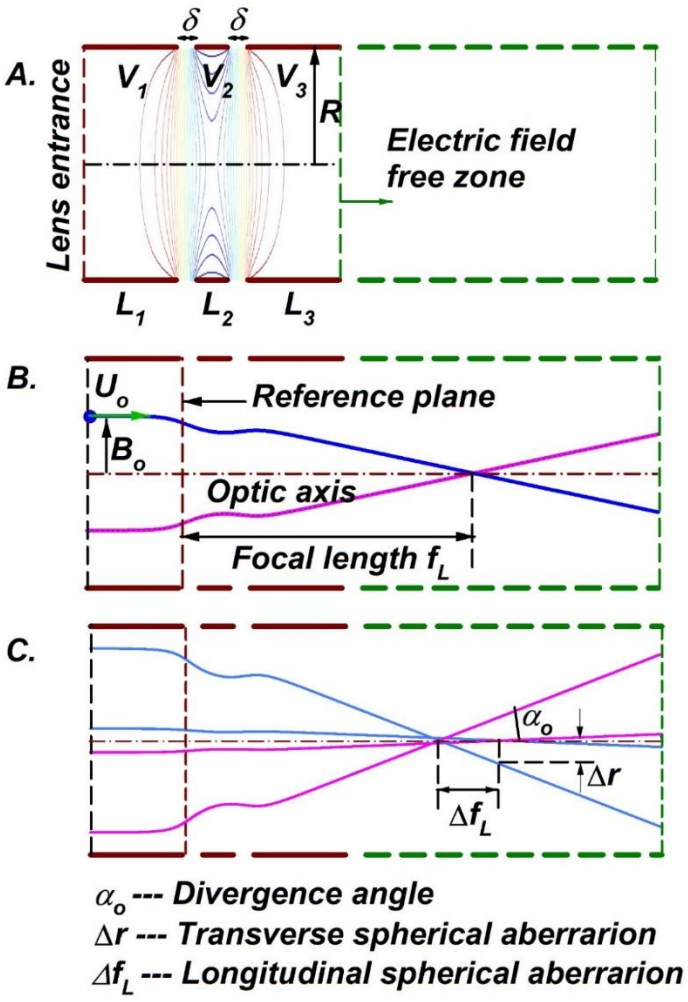

Figure 2: A) Schematic representation of the einzel lens geometry (**not to scale**) and the simulation domain considered in this study. B) & C) Schematic representation of the particle trajectories and definitions of influential focusing parameters.

Results and Discussion

Effect of χ_e and B_o on particle focusing in vacuum:

100 particle trajectories were calculated for each χ_e and for various values of the radial distance of the particle from the optic axis at the entrance of the einzel lens, B_o varied between 0.0 to 1.0. Only trajectories for $B_o \leq 0.5$ are included in **Figure 3** and **Figure 5** for the sake of clarity and to illustrate specifically, the cross-over of particles starting at different radial locations on the starting plane. As χ_e increases from zero, the particles are deflected increasingly strongly

towards the optic axis. *Figure 3*-**A –D** shows the dependence of the focal length f_L on χ_e in the range of 0.01 – 1. The first cross-over point shifts closer to the reference plane as χ_e increases. This behavior is similar to electron trajectories in an einzel lens for different focusing electric field strengths as observed by Heise and Rang (1949) and shown in **Figure 4-A** and **Figure 4-B**. **Figure 4** is a reproduction from the original work of Heise and Rang that highlights the similarity between experimentally-observed electron trajectories and aerosol particle trajectories calculated here. Heise and Rang further observed that for higher strengths of the focusing electric field, the electron trajectories cross the optic axis multiple times as shown in **Figure 4-C** and **D**. From **Figure 5**, representing calculated particle trajectories for $\chi_e = 3 - 275$, it can be observed that for $\chi_e = 3$ the particle trajectories cross the optic axis once near the center of the lensing region and for a second time further downstream. For $\chi_e = 4$ and 10, the first cross-over points are closer to the reference plane and the second cross-over points have also shifted towards the lensing region compared to $\chi_e = 3$. For $\chi_e = 275$, three cross-over points are found in the particle trajectories. A wide dynamic range of χ_e could be obtained by manipulating either the number of charges on the particle n_p, operating voltage difference ΔV and the design of the einzel lens (principally, the electrode spacing distance δ) as shown in **Table 1**.

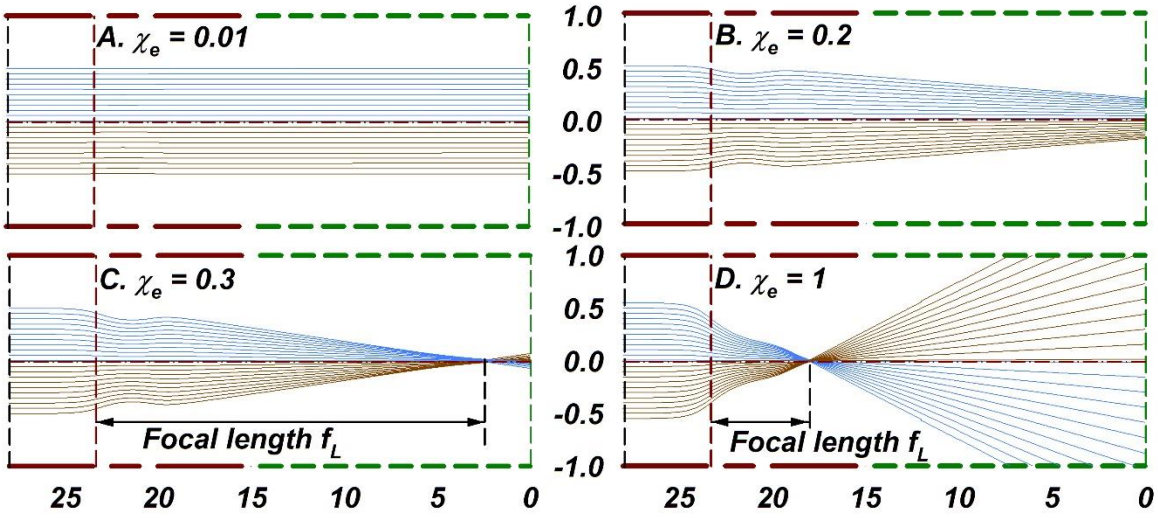

Figure 3: Calculated particle trajectories in vacuum A) $\chi_e = 0.01$ B) $\chi_e = 0.2$ C) $\chi_e = 0.3$ D) $\chi_e = 1$

Figure 3 and **Figure 5** show that charged nanoparticles can be focused analogous to electrons/ions across a wide range of particle size and material, thus making the einzel lens a promising mechanism for particle focusing. The number and location of multiple axis cross-overs shown here are dependent also on the dimensions of the simulation domain and geometric design of the einzel lens. Nevertheless, the trajectory simulations carried out here offer proof of concept for focusing aerosol nanoparticles onto a single spot using einzel lenses for applications such as surface nanopatterning and mass-spectrometry.

The focal length of the particle beam depends on χ_e, B_o and the angle between the velocity vector and the optic axis α_i at the inlet of the einzel lens. In this study, for simplicity, we have set $\alpha_i = 0$ to focus on the effect of χ_e, B_o (i. e.) $f_L = f_L(\chi_e, B_o, \alpha_i = 0)$. For a given χ_e, the average focal length $\langle f_L \rangle$ is calculated based on 100 particle trajectories with B_o distributed randomly between 0 and 0.1. As seen in **Figure 6-A**, the average focal length $\langle f_L \rangle$, shown as a

solid line, decreases with increasing χ_e which offers an operating map to select χ_e to achieve a targeted focal length or particle cross-over distance. The inverse relationship between $\langle f_L \rangle$ and χ_e is approximately represented as:

$$\langle f_L \rangle \approx A\chi_e^{-C} \tag{8}$$

where fit constant A=5.687 and C=1.103 are specific to the dimensions of the domain used here but reveal a general inverse power-law relationship between focal length and focusing voltage expressed in terms of χ_e. Also shown on **Figure 6-A**, are the maximum and minimum focal lengths corresponding to the paraxial ($B_o = 0.005$) and peripheral ($B_o = 1$) particle trajectories. It is seen that the difference between the extreme values of the focal lengths is up to ~20% compared to the average focal length at low χ_e and the difference decreases with increasing χ_e. The minimum and maximum focal lengths shown on **Figure 6-A** reveal that at $\chi_e = 0.34$, the difference is ~20% and at $\chi_e = 3$, the difference is ~5%. This is also confirmed by **Figure 6-B**, that shows the variation of the focal length f_L as a function of the initial radial distance of the particle B_o for various χ_e values. We note that, for $B_o < 0.2$, the difference between the two focal lengths is small compared to the average focal length $\langle f_L \rangle$ – in practical terms, particles that start within 20% of the radius of the cylinder could be focused effectively onto a tight spot with minimum beam spreading.

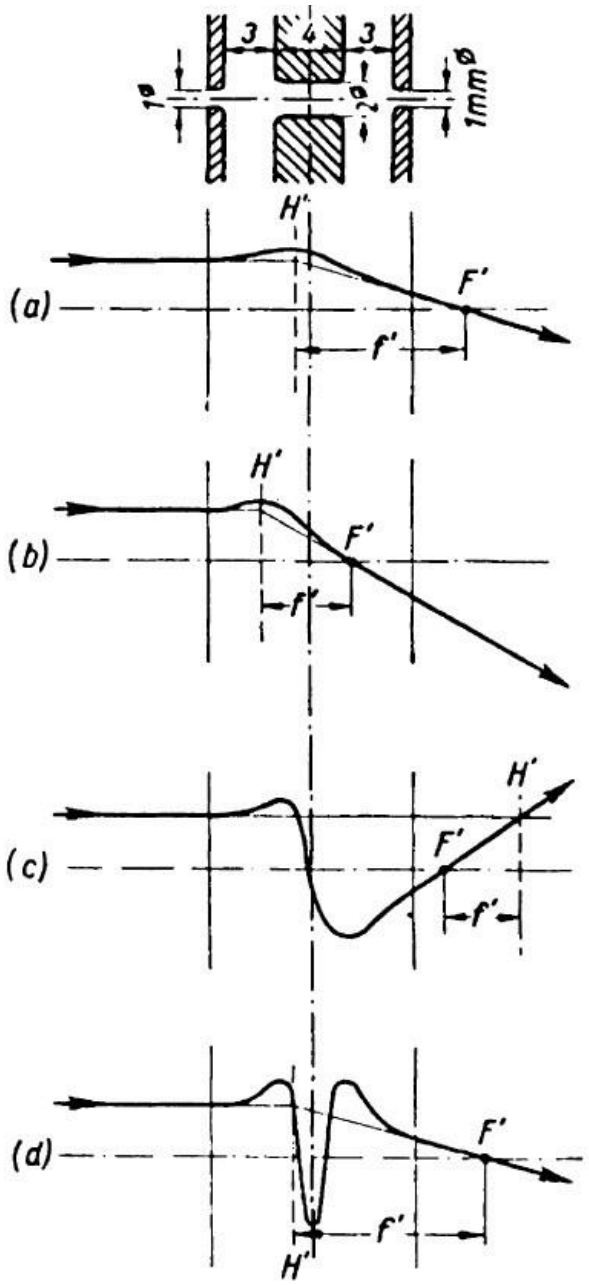

Figure 4: Reproduced with permission from the publisher from Chapter 2.2 ELECTROSTATIC LENSES by K.-J. Hanszen and R. Lauer. Original caption: Particle trajectory and positions of the image side focal and principal points of an electrostatic single lens accordin according to Heise and Rang (1949). The electrical excitation increases from Fig. 2a to Fig. 2d (a, b first operating range, c second range, d third range). ..."

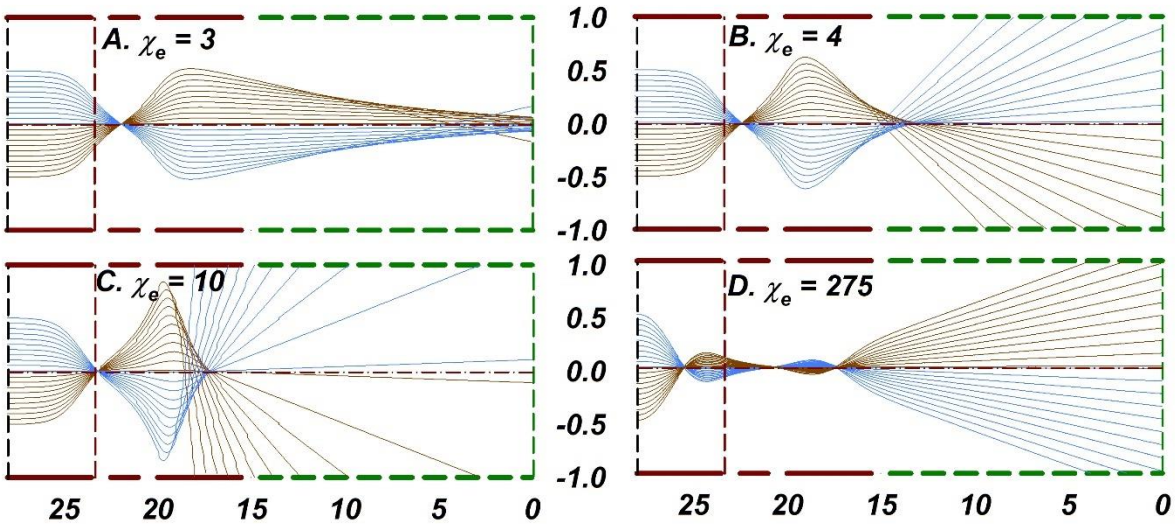

Figure 5: Calculated particle trajectories in vacuum for A) χ_e=3 B) χ_e=4 C) χ_e=10 D) χ_e=275

Constraints in particle focusing using single einzel lens:

The spatial non-uniformity in the focusing electric field of the einzel lens and finite spread of the particle radial location at the inlet plane of the lens causes different degrees of deflection of the particle trajectories. This leads to the particles crossing the optic axis at different points that are located on planes that are parallel (axial direction) and perpendicular (radial direction) to the optic axis. The spread of the focal points *along* the optic axis, known as the longitudinal spherical aberration Δf_L (depicted in **Figure 2-C**), was quantified in **Figure 6-A** using the average focal length with maximum and minimum bounds. The spread of the focal point in the radial direction (*perpendicular* to the optic axis) is defined as the transverse spherical aberration Δr (depicted in **Figure 2-C**). We calculate Δr as the radial distance of a particle trajectory measured in the plane of the paraxial focal point. Along with the focal length, the transverse spherical aberration Δr is also used to quantify focusing performance as a function of χ_e, B_o with $\alpha_i = 0$ i.e. $\Delta r = \Delta r(\chi_e, B_o, \alpha_i = 0)$. Like light and electron optics, particle focusing is also

limited by spherical aberration (Weißbäcker and Rose 2001, Abdelsalam and Stanislas 2017). The spread of the particle beam after cross-over is quantified by the divergence α_o that is the angle between the optic axis and the particle trajectory measured in the plane of the paraxial focal point (like the transverse spherical aberration definition). Likewise, $\alpha_o = \alpha_o\ (\chi_e, B_o, \alpha_i = 0)$ is analyzed from trajectory simulations.

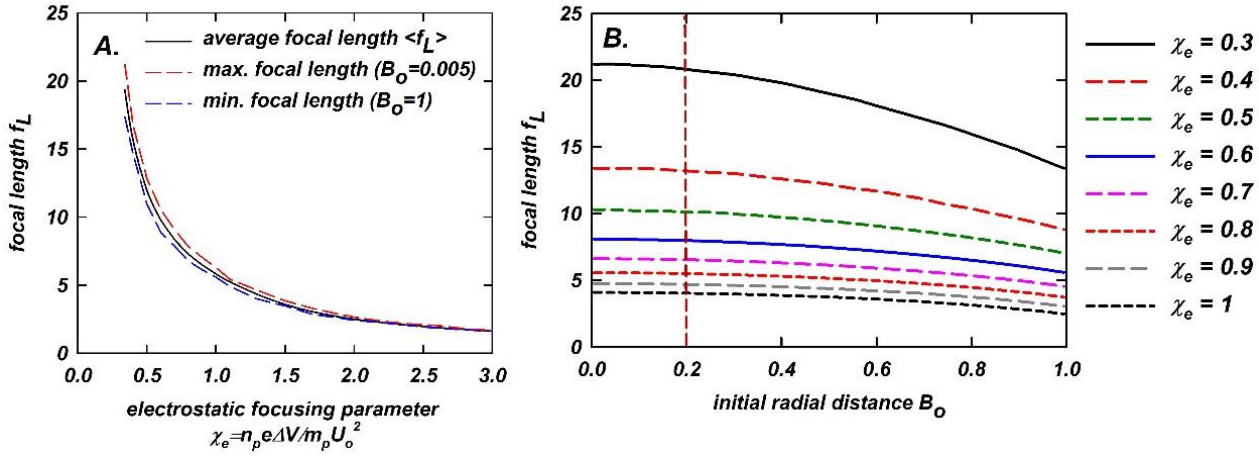

Figure 6: *A) Variation of focal length with χ_e. B) Effect of initial radial distance Bo on focal length for various χ_e*

Figure 7-A shows the variation of the transverse spherical aberration for various initial radial locations of the particle B_o. It is seen that particles that start near the wall (where the electric field is the strongest) are deflected the most and have high Δr. Also, for particles that start within approximately 20% of the radius of the lens (i.e.) $B_o < 0.2$, the transverse spherical aberration is practically negligible. This allows the recognition of an important operating insight which will allow the minimization of beam width and broadening during focusing. Also, as χ_e increases, Δr decreases for identical B_o values, indicating tighter focusing by the electric field. The maximum transverse spherical aberration Δr_{max} (the radial location of the outermost particle trajectory from the optic axis) decreases with increase in χ_e as shown in **Figure 7-B**. As in the case of eq. 8 for the average focal length, the regression relating Δr_{max} (corresponding to $B_o =$

1) and χ_e are also system-specific but indicate a non-linear dependence of the Δr_{max} on the (non-dimensional) focusing voltage χ_e. **Figure 7-C** shows the variation of α_o with B_o and χ_e. It is clearly seen that α_o, and subsequently the beam broadening after cross-over, can be minimized by confining the particles entering a lens to near the optic axis (for example, $B_o < 0.2$). α_o also increases with χ_e, indicating a trend opposite to that of Δr. The maximum divergence angle $\alpha_{o,max}$, plotted in **Figure 7-D**, increases with χ_e. Thus, to obtain a tight focal point the selection of an optimal set of B_o and χ_e is required to minimize *both* Δr and α_o. Depending on the desired location of the focal point (which may be dictated by the position of the substrate or a detector of aerosol particles such as a Faraday cup electrometer), the selection of B_o and χ_e requires optimization considering the trends shown in **Figure 7-A** and **Figure 7-C**. Additional trajectory simulations with the specific dimensions of the focusing device along with the location of the substrate will be necessary to determine the optimal χ_e.

In addition to B_o, χ_e and α_i (whose effect we have deferred to future investigations and set $\alpha_i = 0$ currently), the lens geometry (Daimon, Matsuda et al. 2010) also plays an important role in determining $f_L, \Delta r, \alpha_o$. The length of the electrodes and the width of the dielectric spacing determine the nominal field strength ~ $\frac{\Delta V}{\delta}$ and the gradient in the electric fields (that determine the location of cross-over) in the simulation domain. The effect of lens dimensions on focusing also needs to be investigated in the future. From our trajectory calculations, it is evident that for $\chi_e < 1$, the focal point is sufficiently far from the lensing region (where the electric field is non-zero). For a practical device, it is necessary that any material surface be sufficiently far away from the focusing electrodes to prevent distortion of the field lines and particle trajectories. From the parametric study of B_o, χ_e on focusing, we establish proof of concept for focusing charged aerosol nanoparticles using an einzel lens in vacuum. However, practical devices are operated at

finite low pressure that requires an understanding of the interaction between the particles and the background gas in addition to electrostatic interactions. In the next sub-section, we focus on the effect of gas pressure on particle focusing.

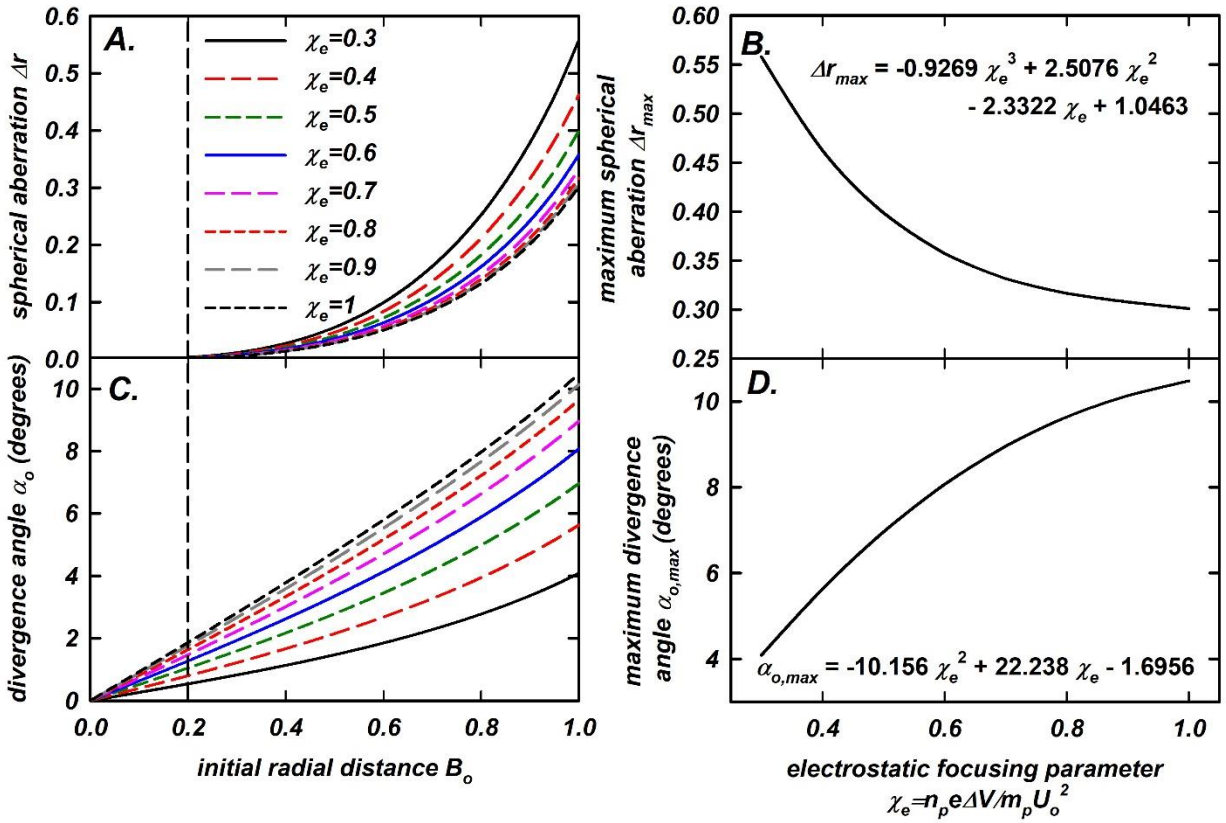

Figure 7: A) Spherical aberration as a function of the initial radial distance B_o for various χ_e. B) The maximum spherical aberration (Δr_{max} corresponding to $B_o = 1$) as a function χ_e. C) Divergence angle as a function of B_o for various χ_e. D) The maximum spherical aberration ($\alpha_{o,max}$ corresponding to $B_o = 1$) as a function χ_e.

Effect of finite pressure on particle focusing:

Maintaining a high level of vacuum is a prerequisite for successfully operating charged particle focusing systems (Matsui, Ichihashi et al. 1995) as particle-gas molecule collisions degrades or destroys focusing performance due to systematic hydrodynamic drag and stochastic Brownian motion. The effect of pressure is parameterized by the particle Knudsen number Kn_p that is

inversely proportional to gas pressure as was previously defined in the *Methods* section. At low pressures, the effect of Brownian motion is expected to be minimal and vanish in the limit of gas pressure $\rightarrow 0$. To assess the importance of Brownian motion at low pressures (~0.001 – 400 Pa), we elected to compare trajectories that were computed using two approximations: 1) that includes drag as described by Henderson's model (equations 5 and 6, with solution given by equations 7a – 7d) but neglects Brownian motion and 2) the Langevin equation of motion (Langevin 1903, Chandrasekhar 1943) that includes drag and Brownian motion. The Langevin equation is strictly valid only in the continuum regime of particle transport (i.e.) at high pressures wherein the particles relax instantly to their thermal velocities due to high number of collisions with gas molecules (Mazur and Oppenheim 1970). The Langevin equation was used to capture the effect of Brownian motion on particle trajectories through the einzel lens. We model the combined electrostatic and hydrodynamic interactions of particles using the Langevin equation of motion (Langevin 1903, Chandrasekhar 1943):

$$\frac{d\vec{v}}{dt} = -St\vec{v} + \chi_e\vec{E} + \frac{\delta}{m_p U_o^2}\vec{X}(t) \qquad (S1)$$

Here, eq. S1 introduces the drag on the particles through a linear damping term $-St\vec{v}$. In addition to the non-dimensional electrostatic parameter χ_e defined in the main text, here the relative importance of particle inertia to hydrodynamic drag on particle motion is quantified through the Stokes number, $St \equiv \frac{m_p U_o}{f_p \delta}$. f_p is the friction factor that relates the hydrodynamic drag force on the particle to velocity ($drag = -f_p \cdot velocity$) in the limit of creeping flow based on the particle Reynolds number $Re_p = \frac{\rho_g U_o d_p}{\mu_g}$ $\left(Re_p \rightarrow 0\right)$. The gas parameters such as viscosity μ_g and temperature T_g describe the momentum and energy exchange between the particles and the gas medium. f_p can be readily obtained using the Stokes law for spherical

particles along with the Cunningham slip correction factor C_c as $f_p = \frac{3\pi\mu_g d_p}{C_c}$. C_c has been reported by empirical correlations to measured drag on particles as a function of particle size and gas pressure in the momentum transfer transition regime (Ku and de la Mora 2009). Also, $\chi_t = \frac{k_b T_g}{m_p U_o^2}$ compares the thermal energy of the particles to their reference kinetic energy (k_b is the Boltzmann constant). The thermal fluctuations in the particle velocity and position due to impacts with gas molecules are captured by adding normally distributed random vectors $\vec{A}_v$ and $\vec{A}_x$ at each timestep. $\vec{A}_v$ and $\vec{A}_x$ have a mean of zero and variances given by equations 3c and 3d, respectively. The timestep Δt is chosen by comparing the diffusion displacement and the electrostatic displacement of the particle as: $\Delta t = \frac{0.001}{St} \cdot \min\left(\frac{1}{\chi_e|\vec{E}(\vec{x}(t))|}, \frac{1}{\chi_t}\right)$. the factor 0.001 was chosen based on numerical experimentation to balance accuracy and computational effort to ensure that the obtained results are independent of the timestep used in the limit of $\Delta t \to 0$. By normalizing the solution to the same derived by Ermak and Buckholz (1980), we obtain the following expressions to track the velocity and position of the particles in time:

$$\vec{v}(t+\Delta t) = \vec{v}(t)\exp\left(-\frac{\Delta t}{St}\right) + \chi_e\, St\, \vec{E}\left(\vec{x}(t)\right)\left(1-\exp\left(-\frac{\Delta t}{St}\right)\right) + \vec{A}_v \qquad (S2a)$$

$$\vec{x}(t+\Delta t) = \vec{x}(t) + St\left(\vec{v}(t+\Delta t) + \vec{v}(t) - 2\chi_e St\, \vec{E}\left(\vec{x}(t)\right)\right)\left(\frac{1-\exp\left(-\frac{\Delta t}{St}\right)}{1+\exp\left(-\frac{\Delta t}{St}\right)}\right)$$

$$+\ \chi_e St\, \vec{E}\left(\vec{x}(t)\right)\Delta t + \vec{A}_x \qquad (S2b)$$

$$\langle A_v^2\rangle = 3\chi_t\left(1-\exp\left(-2\frac{\Delta t}{St}\right)\right) \qquad (S2c)$$

$$\langle A_x^2\rangle = 6\chi_t St^2\left(\frac{\Delta t}{St} - 2\left(\frac{1-\exp\left(-\frac{\Delta t}{St}\right)}{1+\exp\left(-\frac{\Delta t}{St}\right)}\right)\right) \qquad (S2d)$$

Equations S2a – S2d are used in this article to elucidate particle trajectories when both hydrodynamic drag and particle Brownian motion are significant and effect focusing performance in the lens geometry described in Figure 2-A.

Trajectory calculations were obtained for identical gas pressure and focusing parameter χ_e for the two cases – with and without Brownian motion. We note that the Langevin formulation assumes that the drag is linearly proportional to the velocity of the particle relative to the gas medium in the limit of $Re_p, Ma_p \rightarrow 0$, while Henderson's model (derived for high Re_p, Ma_p flows around spherical objects) assumes that drag is proportional to the second power of velocity. Trajectories were calculated for 10 nm, 50 nm, and 100 nm gold particles for pressures 0.001 – 400 Pa all corresponding to $\chi_e = 0.3$ and are presented in **Figure 8**, **Figure 9**, and **Figure 10**, respectively. In each of these figures, two sets of computed trajectories are shown – the top panels correspond to calculations with the Henderson correlation and the bottom panels using the Langevin equation with the value of the gas pressure noted above each panel. In addition to the non-dimensional ratios χ_e and Kn_p, the trajectories are also examined to delineate the dependence of focusing outcomes on size-dependent particle diffusion. Figure 7 (showing trajectories of 10 nm gold particles as a function of pressure and at $\chi_e = 0.3$), demonstrates a marked difference between Henderson and Langevin-derived trajectories. Henderson correlation, that neglects particle diffusion and Brownian motion, shows that at 100 Pa, the einzel focusing of charged aerosol particles ceases to be useful and does not lead to particle cross over on the axis. When diffusion is included, via the Langevin equation, particle focusing is only marginally successful at 0.1 Pa and is significantly poor at greater pressures. We also note that, at 0.001 Pa, Langevin equation also predicts particle trajectories that terminate at the wall. Contrastingly, the Henderson correlation-determined trajectories at the same pressure are very similar to vacuum

(see **Figure 3-C**). This is attributed to the breaking down of the Langevin model – the approximation of a fluctuating force function to mimic particle-gas molecule impacts that are inherently discrete in nature (Mazur and Oppenheim 1970) at very low pressures. Hence, we conclude from this comparison that while the effect of Brownian motion and particle diffusion may be neglected *below* a certain pressure, which would be the operating pressure of an einzel lens based focusing system, such an operating pressure is dependent on particle size and needs to be established through trajectory calculations with an appropriate computational model (Henderson/Langevin or other) and specific lens geometry. This assertion is further supported by the trajectories of 50 nm gold particles at various pressures as shown in **Figure 9** (again, top panels computed using Henderson's correlation and bottom panels using Langevin equation). In this case, we see that up to 200 Pa, particle trajectories are minimally influenced by Brownian motion and diffusion – as evidenced by similar qualitative features between trajectories calculated using both the models. For 100 nm gold particles, the operating pressure of the einzel lens may be as high as 400 Pa (**Figure 10**). These trajectories (**Figure 8– Figure 10**), show the increase of focal length as pressure decreases and the asymptotic behavior of the same as pressure $\rightarrow 0$. They also show us that the maximum operating pressure of the einzel lens system must be selected taking into account particle Brownian motion– that considerably influences 10 nm sized particle focusing than 100 nm or larger sized particles comparatively. The trajectories of particles at pressures of 0 Pa (vacuum), 0.001 Pa and 0.1 Pa are nearly identical as well for 100 nm particles. As pressure is increased, focal length reduces and eventually as pressure exceeds 10 Pa for 10 nm particles, 200 Pa for 50 nm particles and 400 Pa for 100 nm particles, the focusing effect diminishes and gas molecule-particle drag prevents particles from crossing the optic axis at a single focal point. The qualitative features seen in these trajectory calculations

are quantified by the average focal length $\langle f_L \rangle$. The initial radial location of the particles B_o was varied uniformly from 0 to 1 and the average focal length $\langle f_L \rangle$ calculated from both Langevin equation and eq. 5 (with Henderson's drag correlation, eq. 6) is plotted in **Figure 11**. At pressures 10 – 400 Pa, or particle Knudsen number $Kn_p < 1.5 \times 10^4$, the focal length according to both the models differ by no more than 13 % indicating that the contribution of Brownian motion is not significantly high at such low pressures. Above a certain pressure (or below a certain Kn_p), the particles do not cross the optic axis but are lost to the walls due to Brownian motion and electrostatic force. This regime of pressure is clearly unsuitable for operating the electrodes as a focusing device. Hence, a certain maximum pressure is hypothesized to exist for particles of a given size and material. Below this maximum pressure, focusing is reasonably accurately described by the Henderson's equation (that considers only drag force) without undue computational complexity. Also, from **Figure 11**, it is evident that below pressure 1 Pa (or $Kn_p > 1.5 \times 10^4$), the predictions of both Langevin and Henderson's equation are nearly the same, further vindicating the neglect of Brownian motion at low pressures or high vacuum conditions. Based on this sensitivity analysis, subsequent results discussed in this paper are derived using Henderson's equation only for simplicity and may be considered to be accurate for particles 50 nm and larger. For smaller particles, a detailed analysis including Brownian motion is necessary and may be taken up in the future.

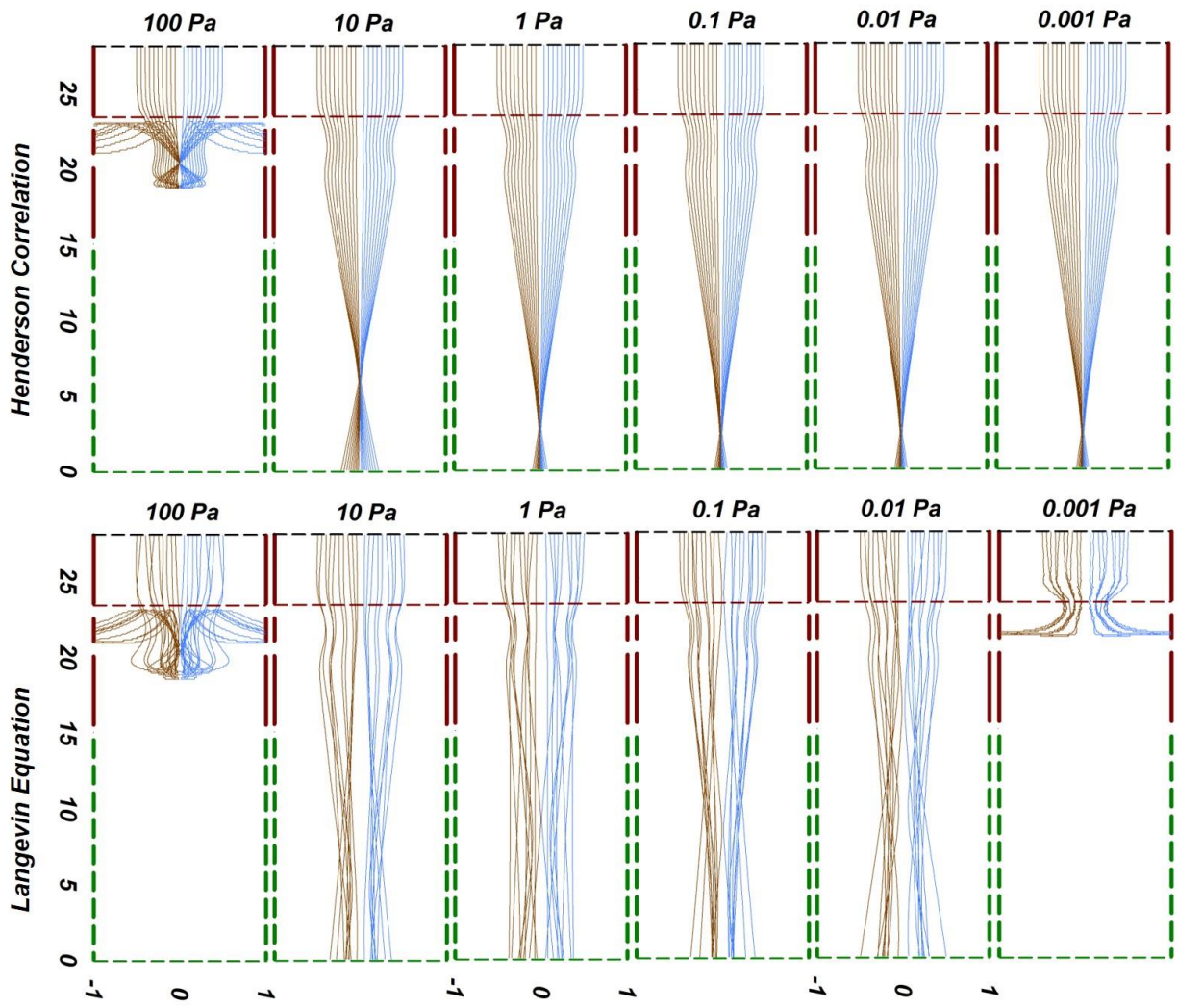

Figure 8: Calculated trajectories of 10 nm gold particles ($\chi_e = 0.3$) at various pressures 0.001 – 100 Pa using Henderson correlation (top panels) and Langevin equation (bottom panels) with pressure noted above each panel.

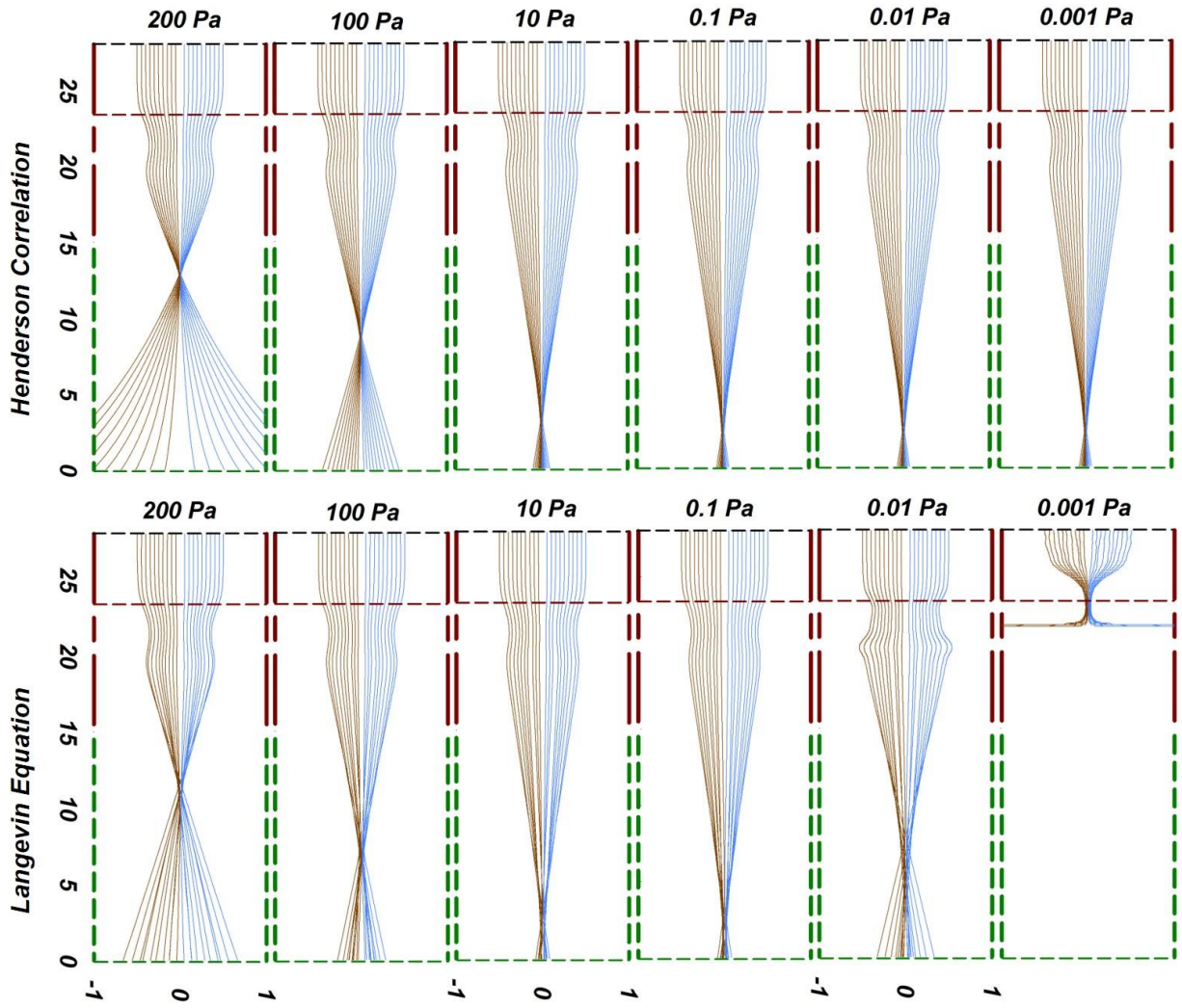

Figure 9: *Calculated trajectories of 50 nm gold particles ($\chi_e = 0.3$) at various pressures 0.001 – 200 Pa using Henderson correlation (top panels) and Langevin equation (bottom panels) with pressure noted above each panel.*

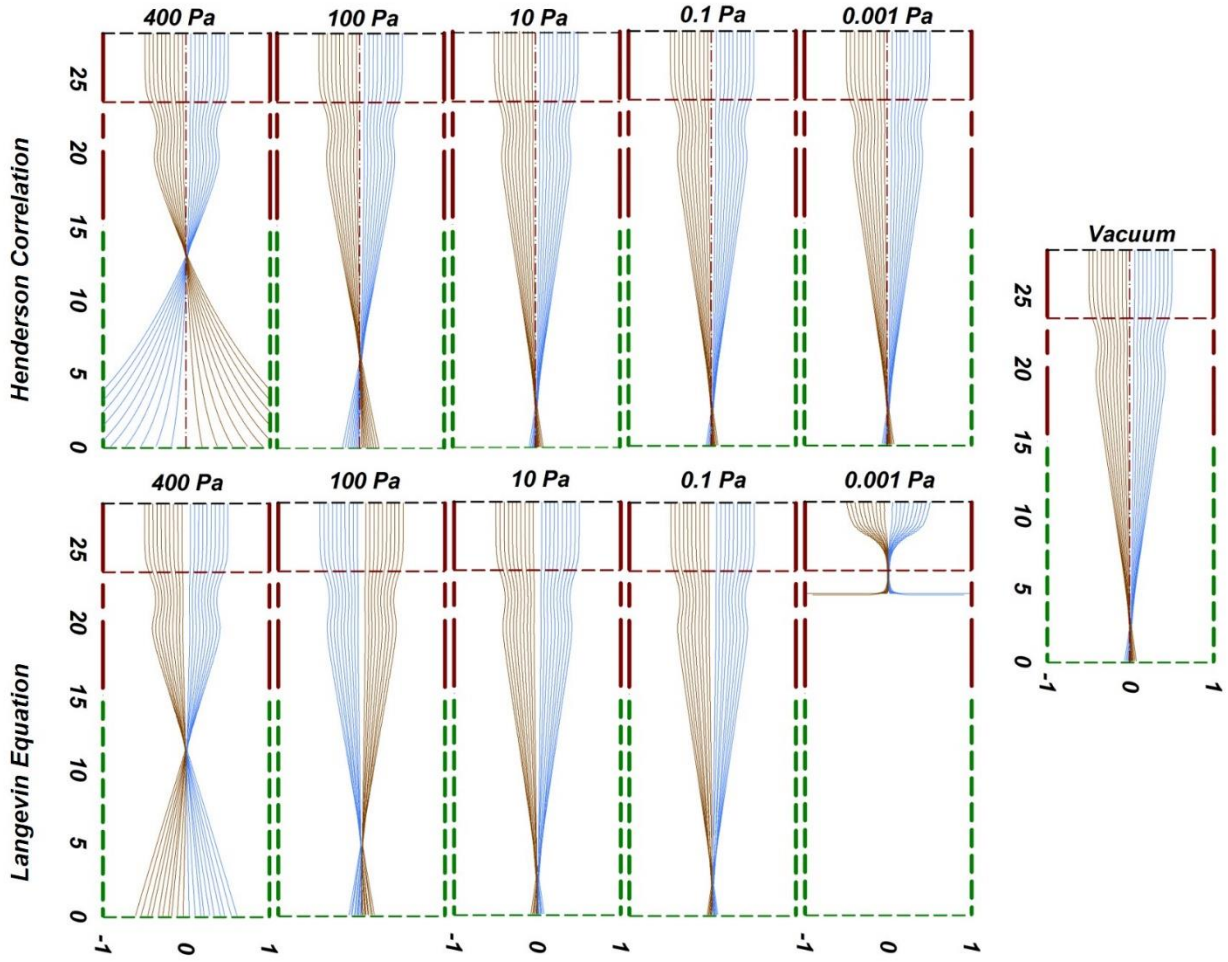

***Figure 10**:* Calculated trajectories of 100 nm gold particles $\chi_e = 0.3$) at various pressures 0.001 – 400 Pa using Henderson correlation (top panels) and Langevin equation (bottom panels) with pressure noted above each panel. An additional case of trajectories in a vacuum is also presented for comparison.

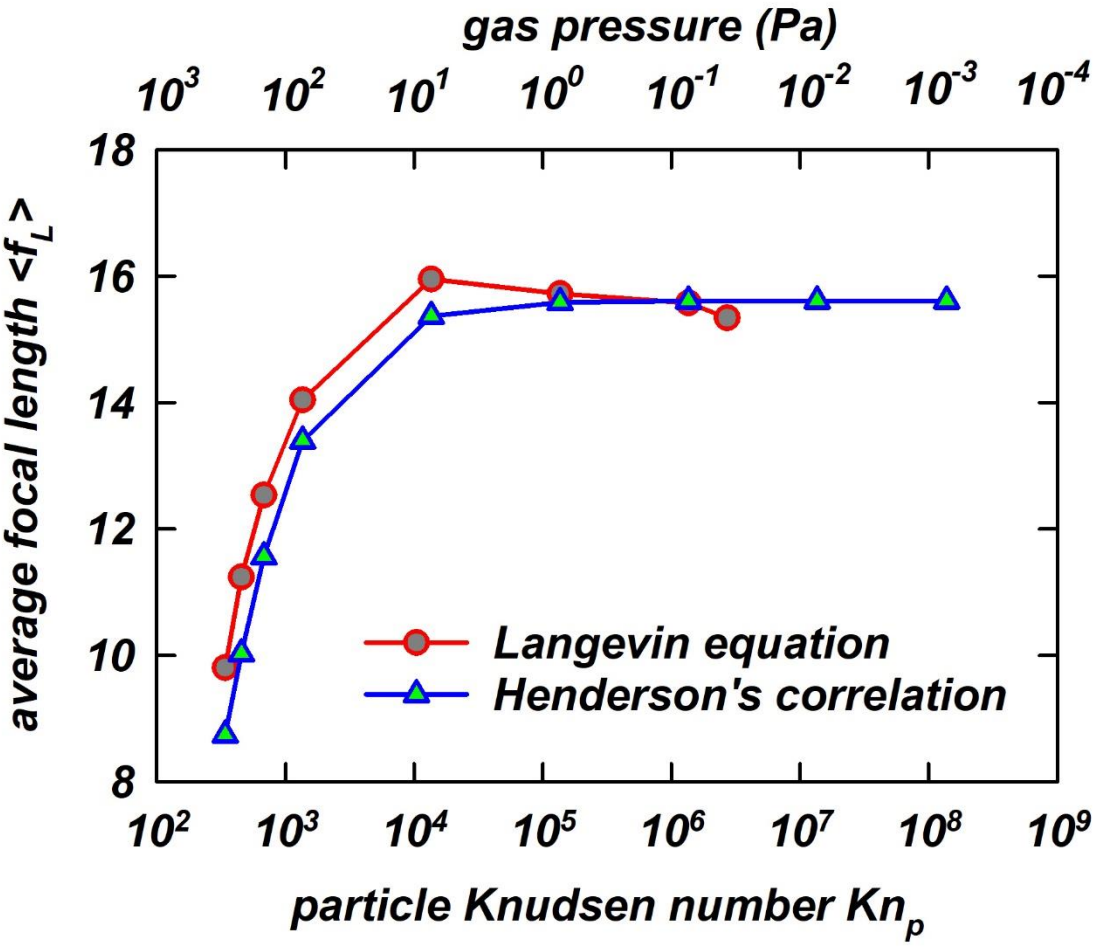

Figure 11: A comparison of the calculated focal length from Henderson's correlation and Langevin equation for different Knudsen numbers.

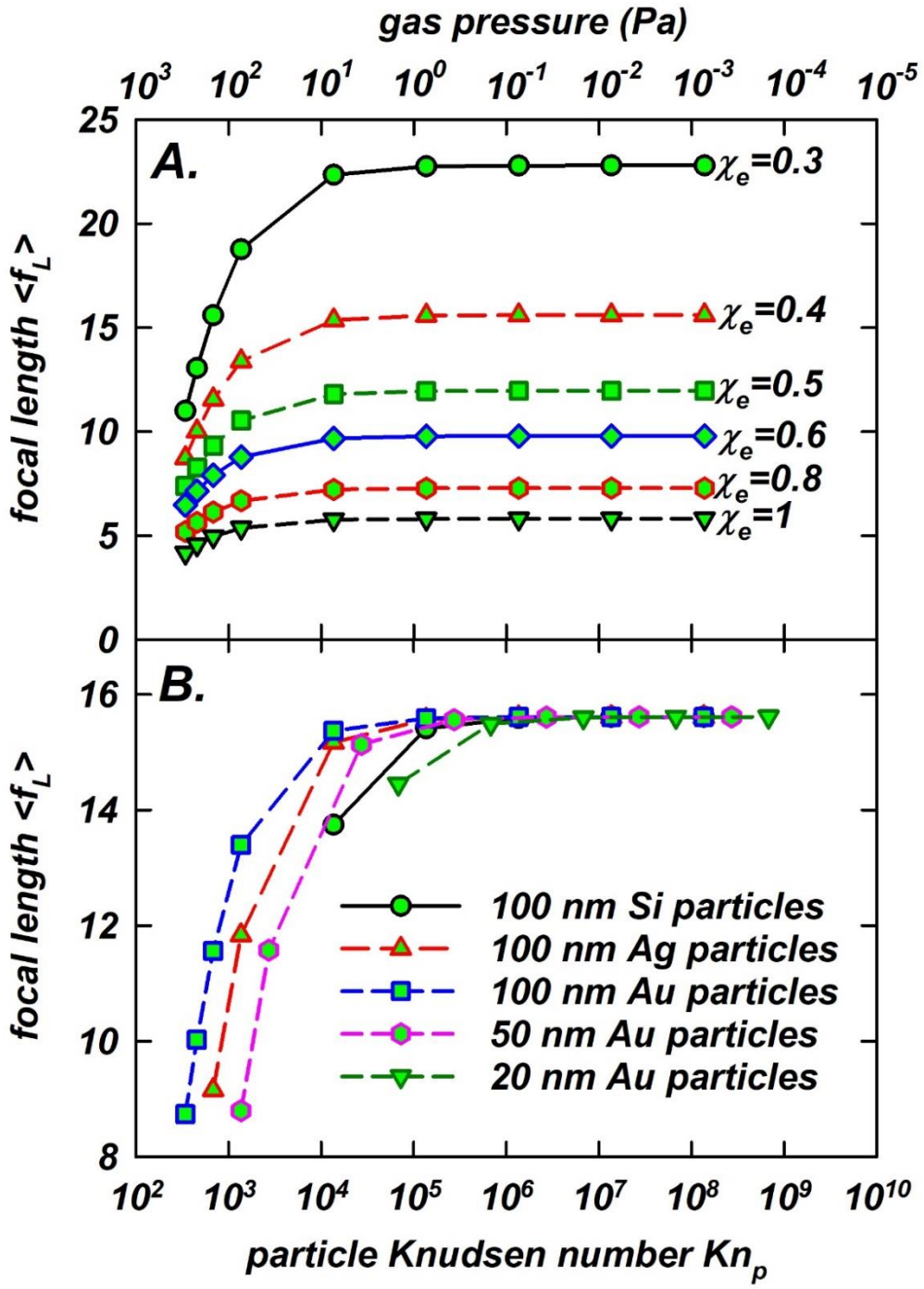

Figure 12: A) Variation of calculated average focal length with particle Knudsen number Kn_p (or gas pressure) for different χ_e. B) A comparison of the variation in average focal length with particle Knudsen number Kn_p (or gas pressure) for particles of different materials and sizes at $\chi_e = 0.4$

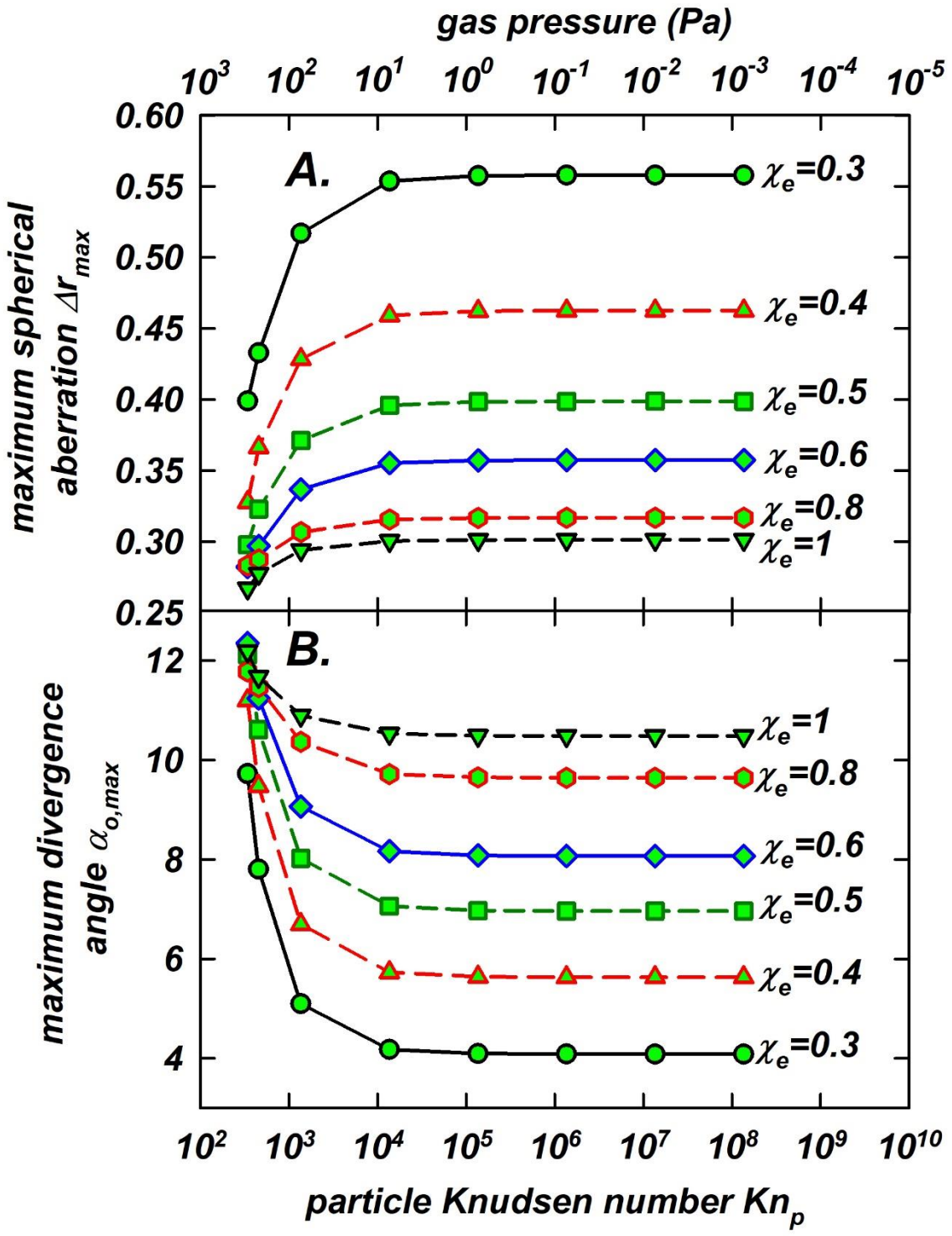

Figure 13: A) Effect of particle Knudsen number Kn_p (or gas pressure) on the maximum spherical aberration for various χ_e.. B) Effect of particle Knudsen number Kn_p (or gas pressure) on the maximum divergence angle for various χ_e.

To probe the effect of both χ_e and gas pressure, trajectory calculations for $\chi_e = 0.3 - 1.0$ were carried out in the pressure range of 0.001 – 400 Pa, that corresponds to $Kn_p = 1.38 \times 10^8 - 3.40 \times 10^2$. To realizes these parameters, 100 nm gold particles were introduced into the einzel lens. The incoming velocity was set to 100 m/s and number of charges on each particle was adjusted to obtain a targeted χ_e. Also, B_o was varied between 0 to 0.2 to minimize spherical aberration. The average focal length $\langle f_L \rangle$ as a function of χ_e and Kn_p plotted in **Figure 12-A** shows three operating regimes based on gas pressure. At pressures > 400 Pa, there is no focusing effect, acting as the upper limit on gas pressure to operate the specific design of einzel lenses considered here. At intermediate pressures, wherein gas drag on the particles is not negligible, the focal length steeply rises with decreasing pressure and converges to an asymptotic value (that is identical to the focal length calculated in vacuum). Below a certain pressure, the focal length is independent of gas pressure, further showing the negligible effect of the gas medium on focusing and establishing an operating pressure for einzel lens focusing of particles. The curves shown in **Figure 13-A**, also depend on more parameters than just χ_e and Kn_p. From **Figure 12-B**, wherein the particle size and density (material) are systematically varied, it is clear that these trends are universal for nanoparticles. The maximum operating pressure (below which focusing is possible) is size and material dependent as shown in **Figure 12-B**. However, the pressure below which the particles behave like in vacuum, is dependent on size as evident from the trends seen from Figure 7 – 9. In practical terms, the selection of a low pressure and a targeted gas flow rate into the einzel lens allows the selection of a suitable pumping system and operation of the lens for focusing a wide range of sizes and materials. Lastly, in addition to average focal length $\langle f_L \rangle$, the maximum spherical aberration Δr_{max} and maximum divergence angle $\alpha_{o,max}$ are also influenced by gas pressure as shown in **Figure 13-A** and **Figure 13-B**,

respectively. Similar to the change in average focal length with pressure, the maximum spherical aberration Δr_{max} (**Figure 13-A**) also decreases with increase in pressure for a certain range, here 10 – 400 Pa. Below, 10 Pa, Δr_{max} can be seen to be independent of gas pressure and material. This allows the realization of tight spot sizes if such an einzel lens were to be used for nanopatterning. However, in **Figure 13-B**, the maximum divergence angle $\alpha_{o,max}$ shows a contrasting trend to Δr_{max} in the 10 – 400 Pa pressure range, $\alpha_{o,max}$ increases with increasing pressure. At low pressure, below 10 Pa, $\alpha_{o,max}$ is also insensitive to the gas pressure. For example, at $\chi_e = 0.3$, the difference between $\alpha_{o,max}$ in vacuum and at ~100 Pa is nearly 25%. For a pressure of 400 Pa, the difference is ~150%. This increase non-linearly decreases with χ_e but remains significant throughout the χ_e range considered. At $\chi_e = 1.0$, the increase in $\alpha_{o,max}$ is ~20%. Therefore, to obtain tight spot sizes for patterning or for increasing the sensitivity of time-of-flight detectors, the placement position of the target surface is crucial. It is most advantageous if the surface is placed at the focal point of the particles (assuming focal point is in the electric field free region and the placed surface does not distort the electric field of the lens). However, if the surface is placed downstream of the focal point (for practical reasons), a large divergence angle will cause significant broadening of the beam after crossover. The diameter of the spot scales with the distance between the focal point and the target surface times the tangent of the maximum divergence angle. Thus, it can be seen that a high operating pressure significantly effects the focusing performance (focal length, beam broadening and divergence angle) and it can even destroy the focusing effect of the lens by reducing the particle inertial velocity by dissipation of kinetic energy. This can lead to significant beam broadening or spot enlargement, reducing the gains of using an einzel lens for focusing particles.

Conclusions

From the described computational parametric study of nanoparticle focusing using a 3-electrode einzel lens, we draw the following conclusions:

1. The electrostatic focusing in vacuum is described by the non-dimensional focusing parameter χ_e, a ratio of the electrostatic energy to the nominal kinetic energy of the particles entering the focusing region. The average focal length $\langle f_L \rangle$ is seen to have an inverse dependence with χ_e. When confined to about ~20% of the radius of the cylindrical lensing region, the spherical aberration and divergence angle of the particles after crossing the optic axis is minimized, thereby allowing the possibility of realizing tight spot sizes with detailed design. For a specific geometry of the einzel lens, a range of χ_e for which a well-focused particle beam converging at a common focal point is computationally demonstrated. By varying the number of charges on the particles, the particle material (density), size and incoming velocity, it is possible to use the non-dimensional framework introduced here to describe the focusing of aerosol nanoparticles of different sizes and materials as well as einzel lens design.
2. From simulations carried out at finite pressure to probe the effect of particle-gas molecule interactions, a maximum operating pressure above which the einzel lenses ceases to be a useful focusing device is seen to exist. Below the maximum operating pressure (that varies weakly with particle size), the focal length, spherical aberration and divergence angle (after cross over) is seen to vary with χ_e, gas pressure (parameterized by a particle Knudsen number) as well as particle diameter and density (that determines the flow-field local to the particle). Below a certain low pressure, the focusing outcomes are nearly independent of gas pressure. This will potentially allow the selection of a suitable operating pressure for a 3-electrode einzel lens for a diverse set of particle sizes, materials and focusing voltage.

Lastly, we have focused exclusively on parameterizing the effect of the focusing parameter χ_e and the particle initial radial distance (when entering the lens) B_o for simplicity and recognize that in addition to these parameters, the angle distribution of the particle's initial velocity (α_i) and the lens geometry are also important. These parameters need to be probed in future investigations. Further, the focusing relies on particles attaining a high, known charge level to practically obtain targeted values of χ_e. This motivates further work into the charging of sub-100 nm particles to charge levels of ~100, beyond what is currently accomplished (± 3) using ambient bipolar diffusion charging (Gopalakrishnan, Meredith et al. 2013, Gopalakrishnan, McMurry et al. 2015). The restriction placed on the spot size due to particle-particle electrostatic repulsion, not considered here, is also a limiting factor to obtain tight spot sizes for nanopatterning, mass-spectrometry or other applications of nanoparticle focusing.

Acknowledgments: This work was partially supported by the DRONES and Data Sciences research grants awarded by the FedEx Institute of Technology, The University of Memphis, and a Faculty Research Grant awarded by the Herff College of Engineering, The University of Memphis.

Scalable High Concentration Aerosol from Commercial Powders

Abstract

Controllable and preferably high concentration submicron dry aerosol is one of the key parameters for successful thin film fabrication using the aerosol deposition method. Aerosol generation using commercially available powder materials are much popular because of its simplicity and ease of dispersion. However, the concentration and consistency of aerosol depends on the control over the dispersion of dry powders. This paper is about an improved version of the previous conceptual design of an aerosol generator (Pokharel, Parajuli et al. 2019) for dispersing dry powders using ultrasonic transducers. The paper investigated the possibility of generating scalable concentration of submicron aerosol by using multiple ultrasonic transducers with vibrating brush technology. Using three ultrasonic transducers with a controlled power supply to the transducers it was possible to generate aerosol concentration in the range of $\sim 10^7 \#/cc$ with commercially available $500\ nm\ TiO_2$ powders and $\sim 10^7 - 10^8\ \#/cc$ for ball-milled TiO_2 powders for a flow rate of $8.7\ lpm$. The mass concentration of particles $> 0.3 \mu m$ was found to be $\sim 500\ mg/m^3$. The concentration could be scaled to even a higher concentration by introducing more transducers and adjusting power supply to the transducers. To maintain a steady supply of aerosol a recommendation is made to place an inline monitor with a controller to adjust power supply to the transducers. The paper also introduces a conjecture based on empirical observations for explaining the reason behind better dispersibility of ball-milled powders. Ultrasonic transducers do deagglomeration to a certain extent however found to be valid for particles greater than ultrafine particles, $> 0.1\ \mu m$. The results are supported by OPS, DMA and CPC data, as well as SEM images.

Introduction

Precise techniques to generate aerosols with the control over mass concentration, number concentration, shape, size and composition (chemical or crystalline phase) are necessary for basic scientific investigations involving particle-laden gases as well as for simulating physical processes (dust explosions, soil erosion, pollutant/debris dispersion, and so on) (Baron 2010, Löndahl, Möller et al. 2014, Perera and Litton 2015, Di, Wang et al. 2019). Alternately, technological applications such as aerosol spray deposition processes (aerosol impact consolidation, aerosol jet printing, thermal/plasma spray) (Biskos, Vons et al. 2008) and other types of aerosol-based additive manufacturing processes such as warfare camouflage using smokescreens, inhalation toxicological or dosimetry studies, filter loading studies also need repeatable aerosol generation methods to produce aerosols at high concentrations ($> 10^5$ #/cm^3) for sustained periods of time (~hours) (Prenni, Siefert et al. 2000). In the case of the aerosol impact consolidation method aerosol mass concentration also plays a significant role in building up thickness of the deposition (Hanft, Glosse et al. 2018).

Common aerosol generators include wet dispersion and dry dispersion such as the use of powder nanoparticles, evaporation-condensation method and plasma synthesized aerosol. Wet dispersion of aerosol is mostly favored for aerosol jet printing, (Secor 2018). For many other cases, dry dispersion is often favored over wet dispersion for its ease of handling, solvent-free room temperature method, and ability to retain the purity and crystalline structure (Schmoll, Elzey et al. 2009). Dry aerosol of particles smaller than 0.1 μm is generated with relative ease using evaporation-condensation or gas-to-particle conversion techniques. In evaporation-condensation methods (Japuntich, Stenhouse et al. 1992), the material to be aerosolized is evaporated by direct heating, electrical current, laser ablation or plasma evaporation and allowed to grow by vapor condensation and particle-particle coagulation by controlling the temperature

history of the particles in the reaction zone. A high energy penalty is involved in generating vapors of material and continuously injecting them into the growth volume to produce particles larger than 0.1 μm. Likewise, spray drying methods, such as aerosol nebulization or electrohydrodynamic atomization, (Swiderska-Kowalczyk, Gomez et al. 1997) are used for generating sub-0.1 μm aerosol. In this method, dispersed droplets containing solute or nanoparticles of the desired material undergoes evaporation and upon evaporation leaves behind aerosol particles. Both evaporation-condensation and spray drying methods are quite successful in producing high concentrations of monodisperse/polydisperse particles that are smaller than 0.1 μm. As the total mass of the particle population scales with the particle size to the third power, injecting high precursor mass flux in vapor/droplet form to produce larger than 0.1 μm particles is practically difficult. On the other hand, we excuse ourselves from the discussion of generating aerosol larger than 10 μm that are conveniently produced by conventional vortex shaking or mechanical dispersion solutions. The generation of high concentration aerosols in intermediate size range of 0.1 – 10 μm, our scope for this article, has been achieved by dispersing dry powders – that are produced in industrial quantities by a variety of methods such as wet chemistry, flame synthesis, plasma synthesis.

Commercially available powders offer a wide range of options in powder particle size, composition and crystalline phase. Dispersion of dry powders, while being cost-effective, simple and portable, presents a few challenges (Calvert, Ghadiri et al. 2009). Firstly, in the size range of 0.1 – 10 μm, particle-particle and particle-bulk surface adhesion forces (that comprise of van der Waals, electrostatic and capillary forces) cause poor flowability and dispersibility (Tang, Fletcher et al. 2008). Secondly, the dispersion of large agglomerates and re-agglomeration of particles. Common techniques of aerosolizing dry powders are mostly use of vibration assisted

fluidized bed (Prenni, Siefert et al. 2000, Au - Yi, Au - Chen et al. 2013). There are few other methods such as, use of fluid nozzle (KOUSAKA, OKUYAMA et al. 1979, Ku, Hare et al. 2015, Tu, Lin et al. 2017, Wu, Tu et al. 2019) and ultrasonic dispersion (Dunst, Bornmann et al. 2018, Pokharel, Parajuli et al. 2019). Fluidized beds offer an effective mechanism to aerosolize powders, but owing to strong adhesion forces, 0.1 – 10 μm require a steady feeding mechanism for mixing with gas. In the absence of such powder feeding, use of fluidized beds does not mitigate intermittency in aerosol generation. Moreover, causes unsteady concentration output, wastage of powders due to collection in low-flow/stagnation zones, and clogging of transport conduits. In some cases, vibration in the fluidized bed forms re-agglomeration of particles. On the other hand, an ultrasonic feeding mechanism, (Dunst, Bornmann et al. 2018, Pokharel, Parajuli et al. 2019), uses standing waves of pressure between a transducer and a flat surface or between two ultrasonic transducers to acoustically levitate aerosol particle grains. The particles dispersed without the use of any moving parts, such as vanes or beads, are then sampled conveniently and mixed with particle-free air to produce well-mixed aerosol for further use in a measurement or a process. Moreover, the use of ultrasonic wave helps in deagglomeration at a certain extant (Knoop, Todorova et al. 2016, Dunst, Bornmann et al. 2018).

Ultrasonic aerosol generator (UAG) designed by Pokharel benefits over Dunst design in the sense of better control over the aerosol generation and deagglomeration. Pokharel used an ultrasonic transducer against a rotating flat powdered bed which served as a reflecting media to make standing pressure waves between them. It would be worth to mention here that to make standing pressure waves, ultrasonic waves have to be reflected and interfere constructively with the incoming waves. The standing pressure waves induce vibration to powder particles on the powder bed, which fueled the particles to levitate over the powder bed and mix with air. It was

observed that the performance of the UAG depends on the thickness and uniformity of the powder thickness on the powder bed. The thickness of powder over the powder bed acts a damping layer for the incoming ultrasonic waves. Therefore, to ensure a good reflectance of the incoming sound waves, powder thickness over the surface has to be minimum. Pokharel's design of UAG doesn't include the feature for controlling thickness and uniformity. In addition, to scale up the aerosol concentration Pokharel recommended to using multiple transducers. These are the two motivations of this study.

In this article, we describe an improved design of the ultrasonic aerosol generator and powder treatment procedure to produce high concentration aerosol by dispersing commercially available dry powders. In addition, a method to measure the high concentration aerosol is presented here. Aerosol number concentration up to 10^7 #/cc using three ultrasonic transducers operating in tandem is demonstrated and the size distribution of the same measured using a TSI® optical particle sizer (OPS 3330) is also reported. Moreover, we describe powder pre-treatment procedures for aerosolization to improve dispersibility and to maintain stable operation for periods that extend up to several hours, an improvement from the 60 minutes in Pokharel's design. A venturi pump-based dilution system as well as deagglomeration setup is described for proper measurement of high concentration aerosol. The rest of the article is organized as follows: in the *Methods* section, we present schematics of the improved design of ultrasonic aerosol generator with three transducers and the aerosol dilution system. Subsequently, in the *Results and Discussion* section, we report the size distribution and number concentration of aerosol particles measured by the OPS along with the estimates for the true concentration produced considering the dilution factors. These findings are discussed to provide supporting evidence for

extending ultrasonic aerosol generator to produce desired high concentration aerosol for specific applications. The conclusions summarize the key findings of this study.

Experimental Methods

Ultrasonic Aerosol Generator (UAG) setup:

Uniformity of the thin ceramic films by aerosol impact consolidation method relies on the steady supply of high concentration aerosol over a longer time. To ensure the supply of tunable and steady high concentration aerosol we developed a modified version of Pokharel's UAG (Pokharel, Parajuli et al. 2019). **Figure 14** is the schematic representation of the modified aerosol generator. The main modifications are the addition of a vibrating soft nylon brush on the rotating powder bed, the powder bed itself, and use of three ultrasonic transducers. The nylon brush holds most of the lump aerosol, while vibrating brush filaments break lumps and disperses continuous thin layer of powder on the powder bed for ultrasonic excitation. The powders are carried out of the brush due to the rotation of the powder bed. While going under the transducers powder particles levitate from the powder bed due to the oscillating standing pressure waves between the powder bed and the ultrasonic transducers. The thin layer of powder provides minimum damping effect to the reflection of ultrasonic wave which is necessary to generate standing waves. In addition, to scale up the aerosol concentration three transducers were used in the modified UAG. Each transducer (SMBLTD63F25H2 of STEINER & MARTINS, INC) operates at a resonant frequency of 25 kHz ± 0.5 kHz with maximum output power of 80W alone, or 60W in parallel connection. The transducers were connected in parallel and an ultrasonic frequency generator (BJUGenerator04, Beijing Ultrasonic, China) capable of producing 20khz to 40khz with maximum power supply of 1200W was used to supply 25 kHz frequency to the three transducers assembly. However, power supply to the ultrasonic transducer could be adjusted from the generator. It was observed that particle excitation increases with the

increase of power to the ultrasonic transducer. We could supply maximum power to the transducers however, we operated the transducers at relatively low power in order to avoid overheating of the transducer and ensured operation for a longer time. In addition, the powder bed has been modified as well. Instead of a grooved metal disk a Ø11 x 3 inch round aluminum pan has been used as a powder bed. The 3 inches raised collar protects the spill out of the powder from the powder bed. The new powder bed can hold enough powder to run the aerosol generator for several hours while the brush ensures the slow discharge of powders in the form of thin sheet for ultrasonic aerosolization. Therefore, the need for continuous feeding has been eliminated which made the device simpler and brought ease in operation. The improved aerosol generator can be operated with both in positive and vacuum pressure. However, we operated the generator slightly below the atmospheric pressure.

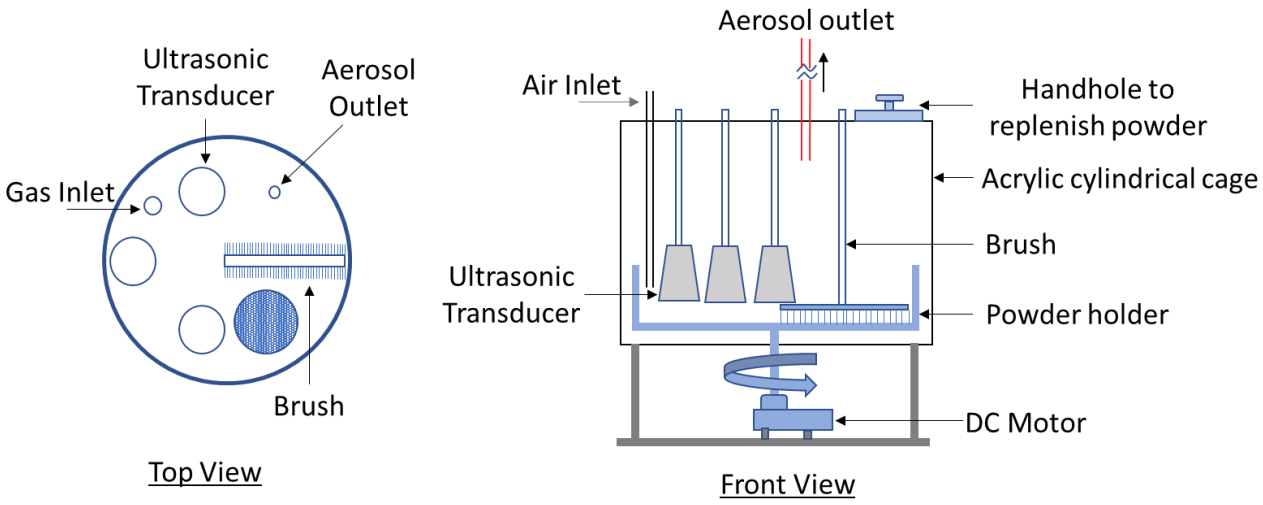

Figure 14: Schematic representation of the modified Ultrasonic Aerosol Generation system

Aerosol dilution, deagglomeration and measurement setup:

The ultrasonic aerosol generator (UAG) was tested against a continuous flow rate of 8.78 lpm over several hours. Particle size and mass concentration was measured to test the durability and steady supply of aerosol over a longer time. Aerosol collected from UAG had a very high concentration and contained agglomerates of powder particles. In order to measure the concentration and size distribution, the concentrated aerosol had been diluted with filtered compressed air in two stages using two venturi pumps. The venturi pumps also helped in certain deagglomeration,(Pokharel, Parajuli et al. 2019, Wu, Tu et al. 2019). **Figure 15** represents a schematic arrangement of the dilution and measurement setup for the aerosol measurement system where $V1$ *and* $V2$ are the first and second venturi pumps respectively. The first venturi pump collected 8.78 lpm of atmospheric aerosol from the UAG chamber and then diluted it to 8.62 times with filtered air. The diluted air was then released to the atmosphere via a filter which had minimal pressure drop corresponding to the flowrate. For the second stage dilution, the

second venturi pump collected 0.73 lpm of atmospheric diluted air from the 1st stage dilution and then diluted again with filtered air to 136.40 times. After 2nd stage dilution, the diluted air had been exposed to a 5-gallon capacity tank at atmospheric pressure for uniform mixing. The mixing tank was vented to the atmosphere via a filter connection which had minimal pressure drop across the filter. Aerosol concentration and size distribution was measured with the sample aerosol collected from the mixing tank. The size distribution and concentration were measured in two steps: Differential mobility analyzer (DMA, Long DMA) with Condensation particle counter (CPC, Kanomax Fast CPC 3650) measured 20 nm to 400 nm particles, while Optical particle sizer (OPS, TSI OPS 3330) measured $0.3\ \mu m - 10\ \mu m$ particles. A neutralizer (TSI Aerosol Neutralizer 3088) was used to charge aerosol particles before passing through DMA for size classification. In addition, particle sizes were measured using SEM before aerosolization, after aerosolization and 2 stage dilution, and after the DMA. A home built electrostatic precipitator was used to deposit powder particles from the gas phase aerosol.

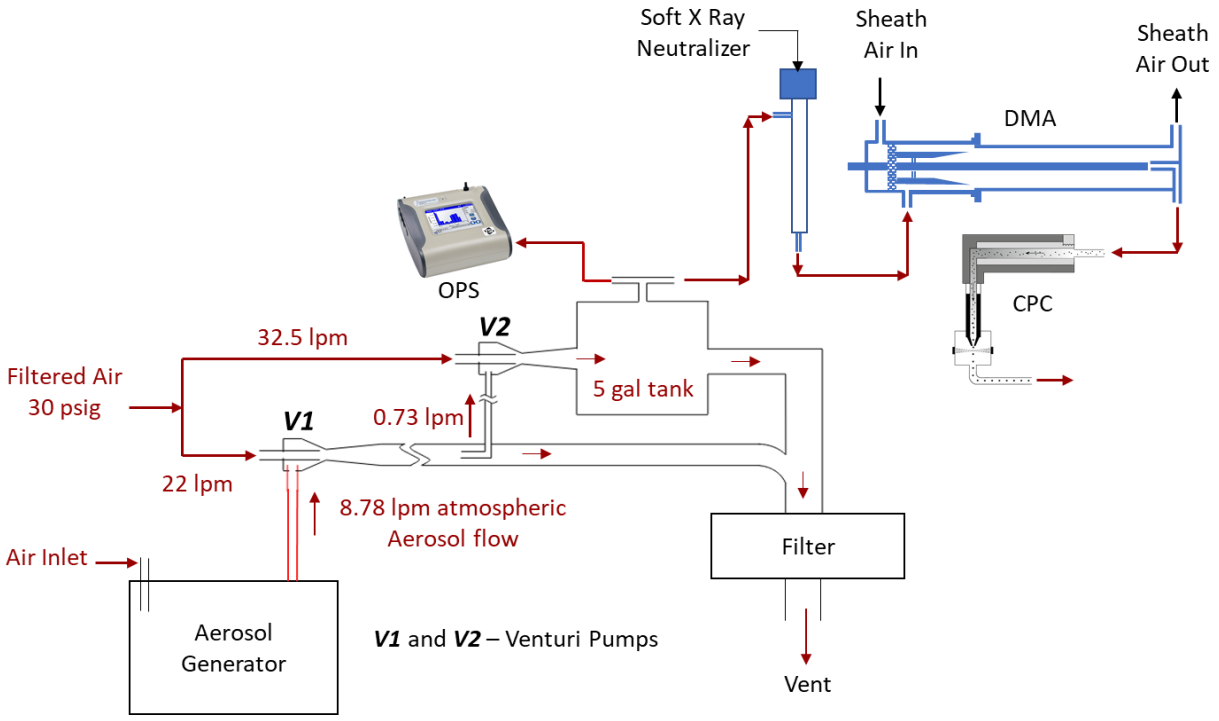

Figure 15: Schematic diagram of dilution, deagglomeration and measurement setup

Materials:

Powder particles used in this study was 99.9% pure 500 nm TiO_2, rutile purchased from US Research Nanomaterials Inc. Although the particle sizes were mentioned as 500 nm however the means size of the particles were found to be around 225 μm. The as received powder is termed as raw powders in the rest of the manuscript. In addition, another version of the same powder, heat treated and ball-milled, was used to test the dispersibility using UAG. **Figure 16**(a) represents the Scanning Electron Microscopy (SEM) image of the raw powder and **Figure 16**(b) represents the size distribution of the raw powder measured by randomly selected 200 particles from the SEM image using Imagej software.

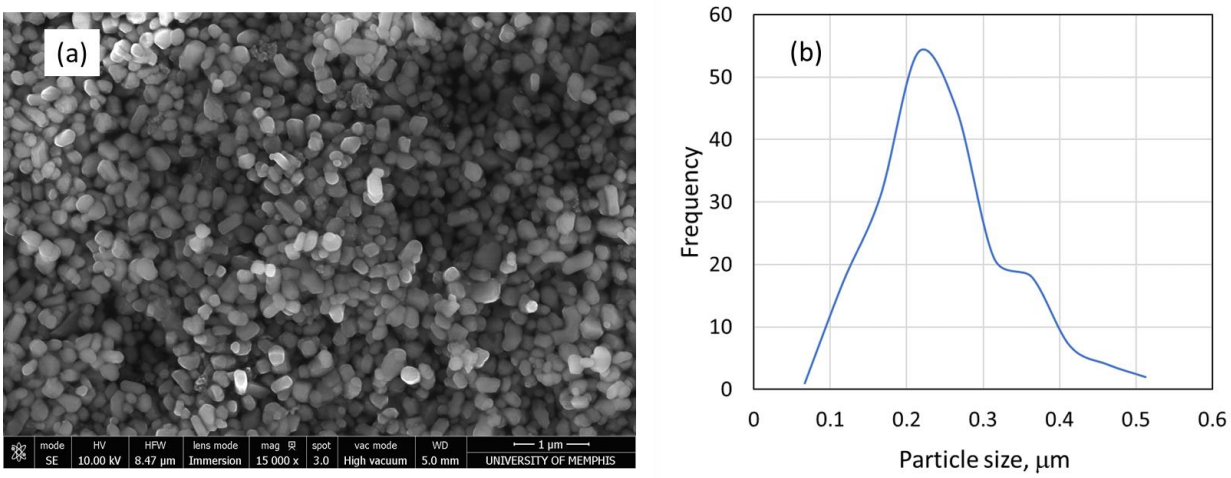

Figure 16: SEM image and size distribution of the raw TiO2 Powder

Results and Discussion

Scalable steady aerosol concentration:

The UAG can supply a very high concentration of aerosol and is scalable. A high concentration of tunable aerosol sources is necessary for fabricating thin ceramic films using the aerosol deposition method (Hanft, Glosse et al. 2018). However, several variables control the concentration of the aerosol coming out of the aerosol generator such as aerosol volume flow rate, number of the aerosol-generating transducers, input power to the transducer, powder materials, deagglomeration and polydispersity, (Zhou, Armstrong et al. 2010),(Chew and Chan 2002). It was observed that it was very difficult to maintain a steady concentration (minimum fluctuation in concentration) aerosol output without having control over the generation side. There is a direct relationship between the aerosol concentration and volume outflow from the UAG. For a fixed volume outflow of aerosol there is an optimum power supply to the transducer to generate a certain concentration range. Below the optimum power level, the aerosol concentration goes to a minimum and above that makes a steady rise in the aerosol concentration until reaches to a saturation point. The steady rise of aerosol could cause re-agglomeration and

would precipitate within the generation chamber or flow as a large agglomerate. In addition, it is also necessary to ensure continuous supply of thin layer of powder delivery under the transducers. As there are multiple factors controlling the aerosol concentration, therefore, it might be necessary to have a controller for the aerosol generation system. An instance could be, to supply steady concentration of aerosol for a fixed volume flowrate an inline concentration monitor equipped with a controller would help to regulate the power supply to ultrasonic traducers and hence control aerosol generation. In this research, an initiative was made to optimize the power delivery to the transducers for an aerosol outflow of 8.73 lpm. The generated aerosol was then diluted to 1175 times (approximately) before measuring with OPS (TSI OPS 3330) and CPC (Kanomax Fast CPC 3650). It would be worth to mention here that TSI OPS 3330 is capable of counting maximum particle concentration of 3000 #/cc in the range of $0.3 - 10\ \mu m$ without any coincidence error while Kanomax CPC 3650 can count maximum 100000 #/cc in the range of $1.9\ nm - 3.0\ \mu m$ without any coincidence error.

Figure 17(a)&(b) represents the OPS reading of number concentration and mass concentration of the diluted aerosol respectively over 300 scans for $500\ nm\ raw\ TiO_2$ powders. Each scan represents an average concentration of over 15 seconds of data. The figures represent 5 trials, each for a duration of 1hr and 15 minutes. The OPS measured number concentration has an average of $3000\ \#/cc$ (approx.) with a standard deviation of 19% (approx.). Therefore, the total number concentration of aerosol particles for $0.3\ \mu m$ and above, product of the OPS measured concentration and the dilution factor, would be in the range of $\sim 10^6\ \#/cc$. In terms of mass concentration, **Figure 17**(b), the average mass concentration for particles of $0.3\ \mu m$ and above is $424\ \mu g/m^3$ with a standard deviation of 20% (approx.). The total mass concentration including the dilution factor for particle above of $0.3\ \mu m$ would be $\sim 500\ mg/m^3$. On the other

hand, particle concentration for the same diluted aerosol measured using CPC, **Figure 17**(c), showed an average of 24,660 #/cc (approx.) with a standard deviation of 11.5% (approx.) for all the size range within 1.9 $nm\ to\ 3\ \mu m$. So, the total concentration of aerosol, considering the dilution factor, for the raw powder would be in the range of $\sim 10^7 \#/cc$. It could be mentioned here that the power supplied to the ultrasonic transducers has been optimized to keep the concentration in this range so that the diluted concentration does not exceed the capacity of measurement devices. The UAG with three transducers can produce much more concentration for higher power input to the ultrasonic transducers and uniform thin powder layer thickness on the powder bed.

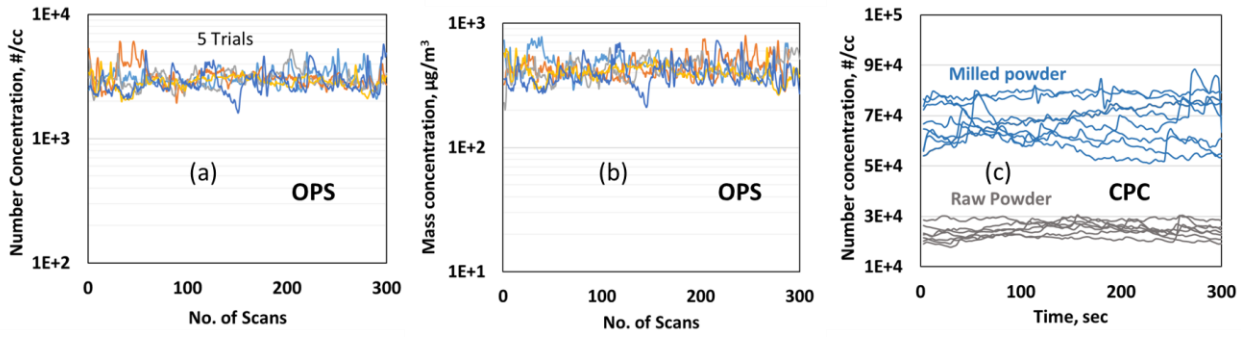

Figure 17: (a)&(b) Aerosol number and mass concentration, respectively, measured at OPS. Each scan was averaged over 15 seconds runtime. Data presented here is for 1hr and 15 minutes runtime; (c) Aerosol concentration measured using CPC for both raw and milled powder where each measurement window is for 5 minutes only.

Figure 17(c) shows aerosol concentration over time for two different sets of powder - raw and milled powders. The figure clearly depicts that the concentration for milled powder is almost 3-4 times higher compared to the aerosol generated from the raw powder. For ball-milled powder the average concentration of the diluted aerosol was found to be $68000\ \#/cc$ (approx.) with a standard deviation of 12% (approx.). Accounting the dilution factor the total concentration of aerosol for the milled powder would be in the range of $\sim 10^7 - 10^8\ \#/cc$. A question might

arise, why the ball-milled powder disperses better, with a high concentration, in compared to the raw powder?

To understand the morphology of ball-milled powders, raw powders were first sintered and then ball-milled for different time duration and observed under SEM. **Figure 18**(a) shows the SEM image of the ball-milled powder that was used to measure the concentration in **Figure 17**(b). **Figure 18**(b) represents the effect of milling time on the size distribution of the powder particles. The unmilled sample powder shows the highest size range and with the increase in milling time the particle size distribution becomes narrower and shifts to the left. It was observed that milling causes the significant breakup of the agglomerates, **Figure 18**(a), as well as the primary sizes of nanoparticles, (Mihara, Hoshina et al. 2010, Exner, Hahn et al. 2015), and hence develops a narrow size distribution of smaller particles as well as makes some ultrafine particles, $< 0.1\ \mu m$. A careful observation on the milled powder, **Figure 18**(a) inset image, reveals that some ultrafine particles are sitting on the fine ($\geq 0.1\ \mu m\ and \leq 2.5\ \mu m$) and coarse ($> 2.5\ \mu m$) particles. Similar images of ball-milled powder could be observed in some other research works (Exner, Schubert et al. 2019). Based on the empirical observation, a conjecture could be made here that due to ball milling effect ultrafine particles attached to the fine and coarse particles and acts a spacer between the larger particles. Since ultrafine particles act as a spacer between larger particles, therefore it reduces the contact area between larger particles and hence reduces particle-particle interaction through van der Waals force. Due to the reduced area of interaction and hence low van der Waals force, the separated particles are less likely to form agglomerates with similar or bigger particles. The authors strongly believe that the spacing effect of ultrafine particles might be one of the intriguing factors of better dispersibility of the ball-milled powder.

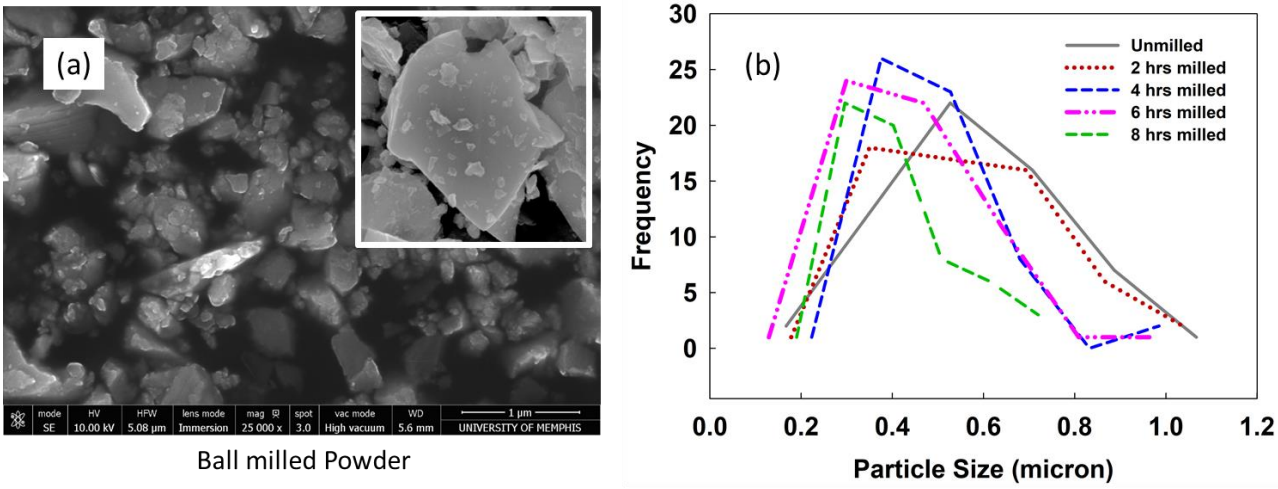

Figure 18: (a) SEM image of the milled powder and (b) size distribution of powders milled for different durations.

Particle size classification and deagglomeration:

Aerosol coming out of the UAG was measured with OPS and DMA. In addition, a homemade electrostatic precipitator was used to collect particles from gas-phase aerosol and then observed under SEM. **Figure 19**(a) represents a SEM image of particles collected from diluted gas-phase sample before going to DMA or OPS measurement. From the SEM image, it can be observed that many of the particles are single i.e. de-agglomerated particles and some ultrafine particles ($< 0.1\mu$) formed agglomerates. A conjecture could be made here that UAG, with its venturi pumps, is capable of deagglomerating particles to some extent for the particles greater than the ultrafine particles($> 0.1\ \mu m$). **Figure 19**(b) represents the size distribution of particles present in the SEM image of **Figure 19**(a), based on a random selection of 200 particles using Imagej software. The size distribution shows a peak at around $0.25\ \mu m$ and ranges from $0.05\ \mu m\ to\ 0.6\ \mu m$. The size distribution of the particles collected from the diluted gas phase aerosol closely complies with the size distribution of the raw powder, in **Figure 16**, from which the aerosol was generated. **Figure 19**(c) represents 5 trials of the averaged lognormal distribution

of the diluted aerosol calculated from OPS data. In each trial, the averaged lognormal value was calculated from the mean of at least 300 scans and each scan represented an average concentration measured over 15 seconds. The OPS size distribution shows a peak at around $0.4\ \mu m$ and ranges from $0.3\ \mu m\ to\ 1.1\ \mu m$. The OPS data shows a higher size range compared to the raw powder and indicates possible agglomeration of particles present in the aerosol that made the peak at a larger size as well as the wider size distribution. It is interesting to see that the maximum size of the agglomerates is limited to $1\ \mu m$. However, at this stage it is difficult to infer the percentage of deagglomeration by the UAG with venturi pumps.

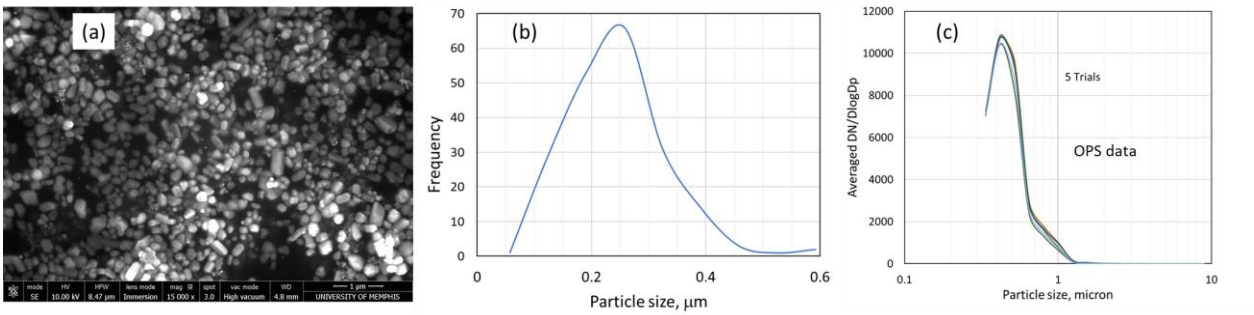

Figure 19: (a) Particles collected from the diluted gas-phase aerosol before going to OPS and DMA. (b) Particle size distribution in figure (a). (c) Lognormal distribution of particle sizes from OPS measurement.

In order to get a better understanding of the aerosol particle sizes below the OPS size range, a Long DMA $(0.02\ \mu m - 0.4\ \mu m)$ was used in connection with a CPC $(1.9\ nm\ to\ 3\ \mu m)$. Aerosol particles were passed through a neutralizer before entering to DMA. **Figure 20**(a) represents the size distribution of the diluted aerosol sampled through DMA. Since DMA operates at some selective specific voltages i.e. selective mobility sizes hence the total concentration observed at specific mobility sizes found to be very low. To clarify the ambiguity of particle concentration and sizes, aerosol particles from the DMA outlet were collected in a

SEM stub using an electrostatic precipitator. **Figure 20**(b), (c) and (d) represents the SEM images of particles collected after DMA corresponding to the mobility size of 100 nm, 200 nm, and 300 nm respectively. From the image analysis, it was observed that all the particles deposited on SEM stubs are agglomerates of ultrafine particles < 0.1 μm. However, the agglomerated sizes found to be closely matched with the corresponding mobility sizes. It was surprising to observe that almost none of the individual particles of those selective mobility sizes deposited on the SEM stubs. There might be several reasons such as improper charging of the large particles, mobility of DMA or the electrostatic particle precipitator. Therefore, it is evident that UAG with the venturi pump settings, it is difficult to break agglomerates of ultrafine particles.

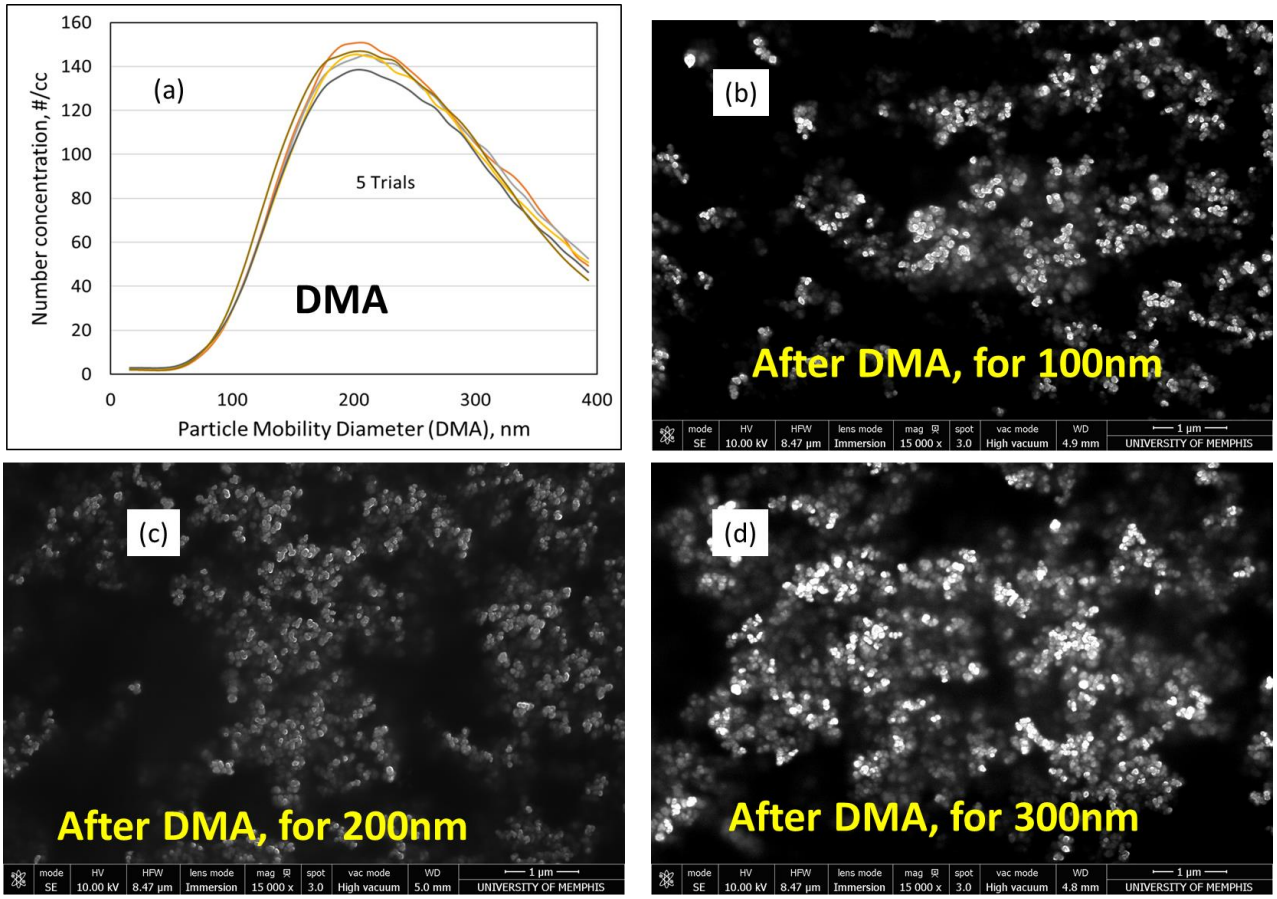

Figure 20: (a) Mobility size distribution from DMA; (b),(c)&(d) SEM image of mobility classified 100 nm, 200 nm & 300 nm particles collected after DMA.

Conclusions

The modified UAG has better powder dispersibility compared to its primitive version. The modification benefits over the primitive version in three different aspects-

First, the vibrating brush holds the lump powder, breaks the lump, and slowly disperse powder as a thin layer. Minimum powder thickness provides minimum disturbances to the standing ultrasonic waves and hence better aerosolization. Because of holding lumps brush eliminated the need of continuous powder feeding on the powder bed, reduced the operational load also provided consistency in an aerosol generation;

Second, Multiple transducers made a positive impact in generating higher concentration aerosol and confirmed the concentration scalability of the device. Now the UAG can easily generate submicron aerosol with a concentration of $\sim 10^7 - 10^8$ #/cc from commercially available powders.

Finally, the replacement powder bed solved the problem of powder spilling out from the powder bed and reduced the powder loss and hazards to a great extent.

Some other improvements, such as thermal management of the transducers, an intermittent feeding system could make the device capable of running even 24 hrs a day. To make the concentration steady, minimum fluctuation, an inline aerosol concentration monitor with a controller is necessary to feed the ultrasonic transducers.

ACKNOWLEDGEMENTS

Partial support for this project was provided by the FedEx Institute of Technology, The University of Memphis DRONES research grant and Development grant. SEM analysis was carried out at the Integrated Microscopy Center at the University of Memphis. The use of ultrasonic transducer to disperse dry powders is covered by patent application U.S. Prov. App. No. 62/724,699.

Fabrication of thin TiO_2 film on glass substrate: an exploratory research

Abstract

Thin films of TiO_2 have a wide range of applications due to its photocatalytic and photochromatic properties, such as decomposing organic materials and dye-sensitized solar cells. Use of the Aerosol Deposition Method (AD) for fabricating TiO_2 films could be advantageous over the conventional methods as a one-step room temperature, high strength low-cost, high-volume additive manufacturing route to process thin ceramic films. However, this method requires optimization and scale up to larger areas (~few sq. inches to a ~sq. ft). This study demonstrates the method of fabricating thin ceramic films of TiO_2 on glass substrates using AD and explores the parametric space of particle velocity and size that leads to successful film formation upon impaction. In addition, this study describes the pre-processing steps of TiO_2 particles for aerosol deposition, the use of virtual impactor for aerodynamic particle sizing and the impact of repeated coating on the quality of the thin-film. It was observed that uniformity in the coating is strongly influenced by the stability of the supplied aerosol particle concentration and the submicron size particle attains the highest quality of the film. However, multiple layering effect have both positive and negative impacts on building up the film thickness. SEM, Optical profilometer, and XRD techniques were used to confirm the film characteristics.

Introduction

Titanium dioxide, commonly known as Titania, has been in use for versatile applications from low end-use as pigment to high end-use as semiconductor materials. Although TiO_2 is an insulator at normal temperature, however, the bandgap is such that it absorbs ultraviolet light at wavelengths just under 400 nm and makes it a wide band gap semiconductor. These photocatalytic semiconductor properties made TiO_2 an excellent candidate for solar energy conversion (Grätzel 2001), gas sensor (Varghese, Gong et al. 2003), biomedical coatings (Lima and Marple 2007) and decomposing organic compounds (Linsebigler, Lu et al. 1995). The potential use of TiO_2 depends strongly on the crystal phase and structure, particle size, and specific surface area. Despite having the potential use of the TiO_2 the application has been limited due to the complexity of fabricating thin films for different applications. Several methods of fabricating thin of TiO_2 have been investigated such as sol–gel methods (Barbé, Arendse et al. 1997), chemical vapor deposition (Zhou and Ma 2009), chemical spray pyrolysis (Natarajan, Fukunaga et al. 1998), plasma spray deposition (Chen, Lee et al. 2006, Du, Coyle et al. 2015), cold spraying (Yang, Li et al. 2008) and Aerosol deposition (AD) (Akedo and Lebedev 1999). All these except AD either needs chemical synthesis, expensive plasma ambient or high heat, which limits the use of different substrates.

On the other hand, the aerosol impact consolidation method, widely known as Aerosol Deposition (AD) method, is a most aspiring ceramic thin film fabrication process (Akedo 2008). The AD method uses high kinetic energy submicron particles generated from powder phase aerosol to impact on a substrate and forms a thin ceramic film on the substrate. Particles upon impaction undergo plastic deformation accompanied by poly-crystallization and bonding to the substrate (Daneshian and Assadi 2014). A wide range of ceramic martials could be deposited on almost any substrates by this method(Chun, Kim et al. 2008). The AD method benefits over the

prevalent methods of ceramic thin film fabrication as a direct write, solvent free, etch free, room temperature deposition method and needs minimal post treatment, and hence reducing the cost of the fabrication process (Hanft, Exner et al. 2015). Ceramic film fabrication using this method attains reportedly higher strength, high density of the film and faster as a direct write method (Chun, Kim et al. 2008).

Several researchers have tried to develop TiO_2 thin film using AD for different applications in mind. Chun et al.(Chun, Kim et al. 2008) reported successful coating development of TiO_2 using AD on different metallic (stainless steel, Cu alloy, Al alloy) and polymer substrates (PET, PMMA) and they have observed higher hardness and modulus of the TiO_2 coated area compared to non-coated area. Ryu et al. (Ryu, Hahn et al. 2010) developed a novel method of fabricating porous network structured thin film of TiO_2 on glass substrate using the AD followed by chemical etching. They observed a strong photocatalytic activity under UV radiation. Park et al. (Park, Lee et al. 2012) used the AD method to fabricate TiO_2 thin film for photokilling or photodegradation applications. They have showed that the aerosol deposited films contributed to the increase in the surface area because of extreme roughness, which enhances the photokilling and photodegradation performance. Cho and Yoon (Chun, Kim et al. 2008) used the AD to fabricate both compact and porous layer of TiO_2 for dye-sensitized solar cell and was able to achieve a 4.2% higher conversion efficiency over as deposited film after annealing at 450^{o}C. Besides, some researches tried to control microstructure of TiO_2 coating by changing the preparation method which showed significant influence on the coating performance (Fan, Yang et al. 2006, Yang, Liao et al. 2012). Although, all of these studies showed that powder preparation and size distribution of the particles in aerosol plays an important role in

fabricating thin ceramic films of TiO_2, however methods of selecting/preparing a narrow size range of particles that would contribute to the thin film formation have yet to established.

This study is focused on an effort to prepare a narrow size distribution of powder particles for fabricating thin ceramic film of TiO_2 and aerosolizing them using an ultrasonic aerosol generator, a novel method that generates aerosol from powder phase materials. The study also reflects the importance of aerodynamic particle sizing and number of overlapping coatings on the quality of the produced film. In addition, the study reveals the effect of particle size ranges on the deposition performances of the TiO_2 coating.

The remainder of the paper is organized as follows: Section 2 describes the powder preparation procedure and effect of different process parameters on the produced powder particle sizes. Section 3 describes the experimental setup for aerosol deposition and different process parameters. Section 4 describes the experimental findings and section 5 summarizes the major conclusions.

Experimental Methodology - Powder preparation

Aerosol deposition (AD) method is based on the particle kinetics which is a function of particle morphology and the attained velocity (Lebedev, Akedo et al. 2000). Several research works showed the necessity of powder pretreatment as a precursor to the well adhered deposition system (Mihara, Hoshina et al. 2010, Exner, Schubert et al. 2019). Commercially available TiO_2 nanoparticle sizes, although has the said size to be 1 -1.5 micron in size; however, almost all the particle sizes are less than 500 nm. It was observed that the commercially available particles either forms a very faint coating or sometimes even don't form any coating. Therefore, the pretreatment of powder became an indispensable part of the aerosol deposition (AD) process. This study describes several aspects of the pretreatment of TiO_2 powders to obtain desired particle kinetics for deposition.

Particle size growth by sintering

Sintering causes particle growth mostly due to surface diffusion (German 2001, Buesser, Gröhn et al. 2011). In this study, 100 nm TiO_2 powders (rutile) purchased from US-nano are used as primary particles. The raw powders are agglomerated and amorphous. On the other hand, 100 nm powders are too small to be deposited using aerosol deposition method (Hanft, Exner et al. 2015). In order to increase the particle sizes, the powders are then sintered to 700, 800, 900, 1000 and 1100 ℃ for 8 hours in air. **Figure 21** shows the scanning electron microscopy (SEM) images of the raw and heated powders at different temperature. From the images it can be qualitatively observed that heated powders formed more distinctive shape compared to the raw powder. **Figure 21**(a) shows the 100 nm as received TiO_2 powders which are amorphous in shape. On the other hand, heated powders are relatively spherical in shape. **Figure 21**(b) shows the sample powders sintered at 700 ℃ for 8 hours. It can be observed that at 700 ℃ although particle size growth is less distinctive compared to the raw powders, but they are relatively more spherical compared to the raw powders. The increase in the particle size is more prominent with the rise of the sintering temperature, **Figure 21**(b) – (f). Here, 1100^{o}C showed the maximum size growth, almost 10 times the initial sizes of the TiO_2 nanoparticles.

Figure 22 shows the normal size distribution of heated powder particles after 8 hours of sintering. It can be clearly observed that sintering at 700 ℃ reduces the particle size range as sintering causes the particles to shrink. Sintering over 700 ℃ shows a significant increase in particle size and increases the standard deviation, hence the size ranges. The similar growth was also observed for CeO_2 particles (Exner, Schubert et al. 2019). From **Figure 22** it can be clearly observed that at 700^{o}C particle size range is the lowest and with the increase in sintering temperature particle size range increased and the maximum size range can be observed for 1100^{o}C while the mean particle size is also the highest.

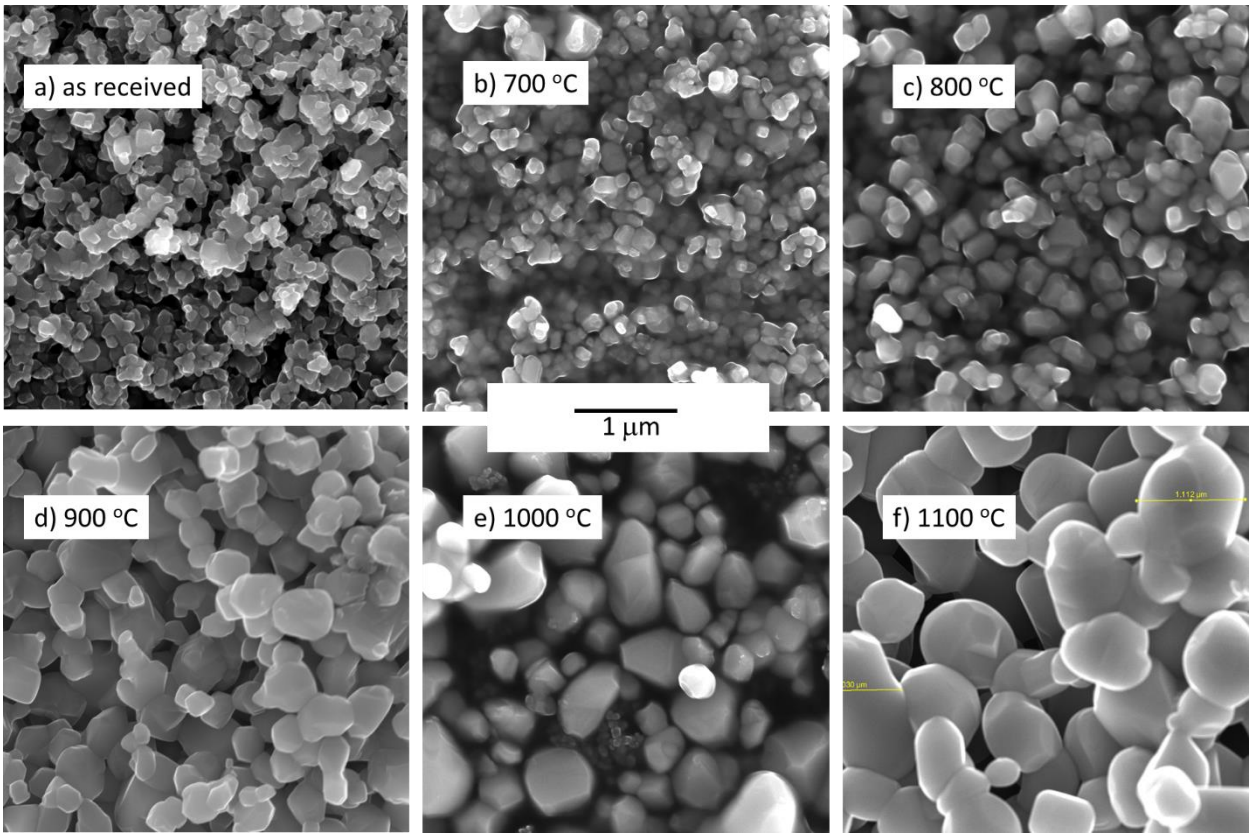

Figure 21: 100 nm TiO_2 heated at different temperatures for 8 hrs at ambient air

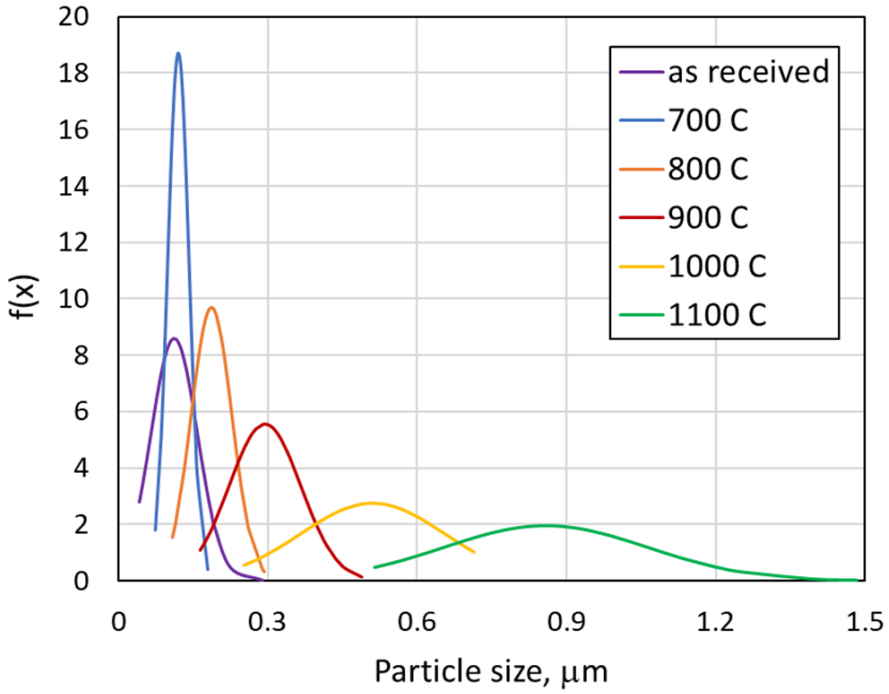

Figure 22: Normal distribution of TiO_2 particles after sintering for 8 hours at different temperatures

Particle agglomeration and deagglomeration

The sintering process not only increases the size and size range of the powder particles but also develops large agglomerate. The sintering process causes the formation of a neck between particles which binds several particles together and forms hard agglomerates. Agglomerated particles are less likely to make coating using aerosol deposition method (Hanft, Exner et al. 2015). **Figure 23**(a) shows SEM image of sintered TiO_2 powders at 1100℃ for 8 hrs where each agglomerate particle size is around $10 - 20\ \mu m$. Each clustered particle is an agglomerate of 0.6 to 1.0-micron particles, **Figure 23**(b). To break these clustered particles, sintered powders are later ball-milled to get individual particles. The effect of ball milling depends on several factors such as rate of rotation, ball size and particle to ball mass ratio. Larger ball size and high rotation rate lead to smaller particle size. Therefore, an optimized ball sizes

and rotation rate must be selected to break the agglomerates without making the individual particle size much smaller. The effect of ball milling to generate deagglomerated particle has also been reported in some other research works (Mihara, Hoshina et al. 2010). **Figure 24**(a) shows the SEM image of TiO_2 powders after 8hrs of ball milling of the powders sintered at 1000℃. The image shows more of the individual particles which is a great improvement in breaking up the agglomerations. The mean size of the powder particles reduces with the number of hours ball milling. Similarly, the particle size also reduces with higher rotation of ball milling, as shown in **Figure 24**(b). Likewise, particle size range also reduces with the increase of ball milling time and speed. **Figure 24**(c) and (d) shows the particle size distribution after ball milling for different hours at 250 rpm and 450 rpm respectively. From **Figure 24**(c) and (d) it is evident that particle size range is smaller for 450 rpm compared to that of the 250-rpm ball milling whereas both the cases particle size range decreases with the increasing of the ball milling time. In this experiment, particles of different size distributions were obtained following the mentioned powder pretreatment procedure.

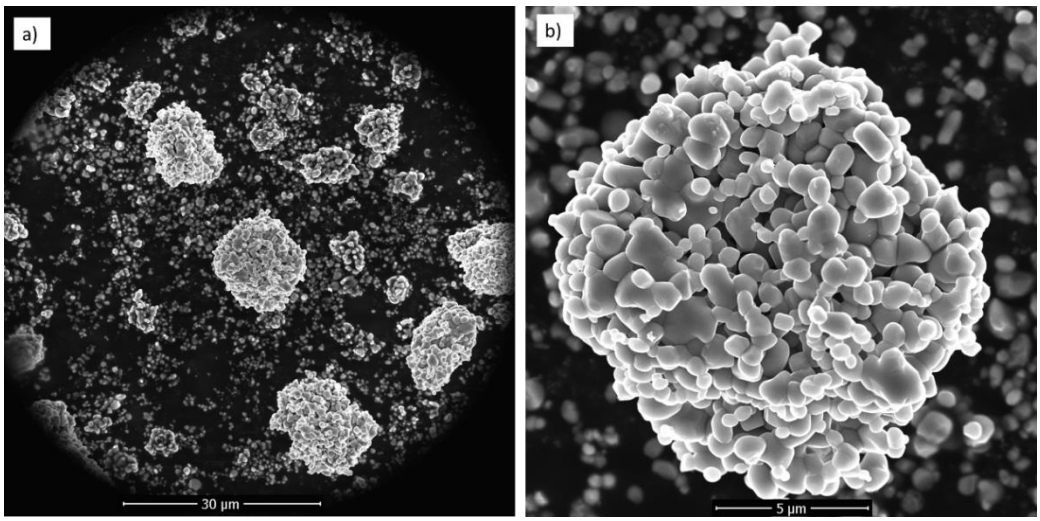

Figure 23: SEM image of sintered TiO_2 particles at 1100 ^oC for 8 hrs

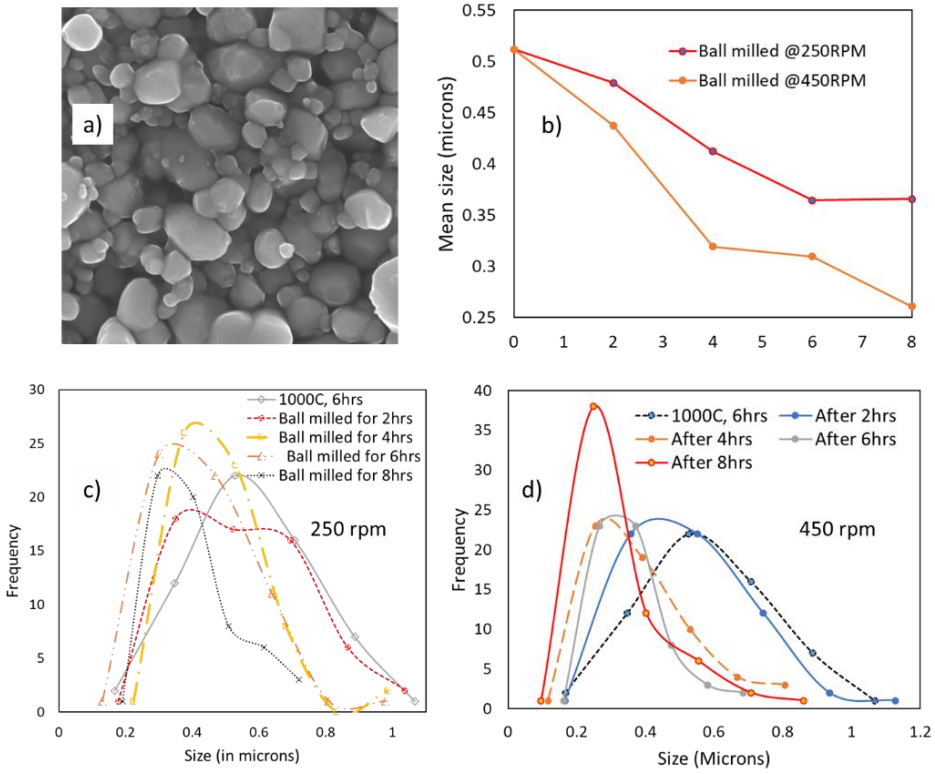

Figure 24: Effect of ball milling on powder preparation. a) SEM image of 8hrs ball-milled powder at 250 rpm, b) Mean size of particles with number of hours at two different rpm, c) particle size ranges with ball milling time for 250 rpm d) particle size ranges with ball milling time for 450 rpm

Experimental setup and procedure

Thin film fabrication process using the AD requires an aerosol source and a vacuum deposition facility equipped with a substrate holder and a translation stage facility, and a pumping station. In this study, we have developed an inhouse aerosol generator system and a

vacuum deposition system. A brief description of the experimental setup and the process flow parameters are described below-

Basic experimental setup:

The experimental setup, **Figure 25**, consists of three major parts – an aerosol generator, a vacuum chamber and a pumping station. The aerosol generator system produces aerosol from powder phase materials. It differs from the conventional aerosol generator in the process of powder lifting mechanism. In this process, powder particles are lifted from the powder bed through the action of ultrasonic standing waves other than mechanical vibration. The standing ultrasonic waves from the ultrasonic transducer lifted the particles from the powder base and mixed with the flowing carrier gas to make aerosol. The number concentration of the particles in aerosol could be varied by changing the power supplied to the ultrasonic transducer which regulates the excitation amplitude of ultrasonic waves. The noncontact based powder lifting mechanism helps to maintain a steady supply of aerosol with an adjustable concentration of the particles. A detailed explanation about the ultrasonic aerosol generator could be found in Pokharel's (Pokharel, Parajuli et al. 2019) and Ahmed's work. (Ahmed, Suresh et al. 2020). The aerosol generator is kept at atmospheric pressure by either making it open to the atmosphere or by supplying gas inside the chamber. The aerosol is then transported from the aerosol generator to the vacuum chamber through the action of differential pressure between the atmospheric aerosol chamber and the vacuum chamber. An aerosol expander fitted with a homemade virtual impactor is placed in between the aerosol generator and the vacuum chamber to remove large agglomerates and to get the steady supply of aerosol. While entering in the vacuum chamber, the aerosol is passed through a supersonic converging diverging nozzle to accelerate particles in the vacuum chamber. The vacuum chamber pressure was maintained 200 to 600 Pa while the supplied air was maintained 10-40 slpm by evacuating through a combination of a booster pump

connected in series with a rotary vane pump. As the particle bonding in the aerosol deposition method relies on the kinetic energy of the particles therefore particle size, mass, acceleration in the nozzle and the deposition chamber pressure are the critical parameters for the aerosol deposition.

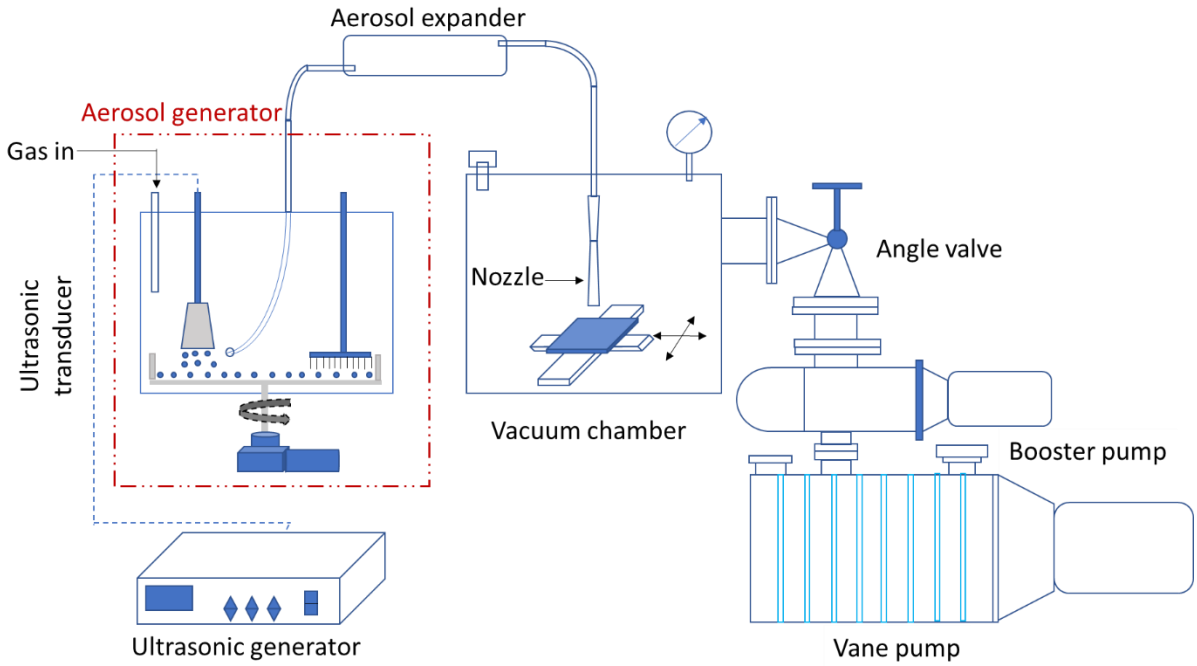

Figure 25: Schematic diagram of the experimental setup for aerosol deposition

Table 2: Deposition condition used for Thin film of TiO_2

Carrier gas	Air
Carrier gas flow rate	10 - 40 SLPM
Pressure in the aerosol chamber	Atmospheric
Deposition chamber pressure	200 – 600 Pa
Nozzle type	Slit nozzle, CD slit nozzle
Nozzle to substrate distance	10 mm
Stage traverse speed	0.1 to 0.3 mm/s
Particle mean size	**0.5 μm – 1 μm**

Numerical investigation of Nozzle and chamber pressure

In an aerosol deposition method the bonding mechanism between particle to the substrate and particle-particle bonding relies on the kinetic energy of the particles (Akedo 2002). In Aerosol deposition and cold spray deposition, the use of slit nozzle is often favored over cone nozzle due to its higher area coverage and the flexibility to use large standoff distance of the substrate from the nozzle exit (Chang, Brock et al. 1993, Lee, Park et al. 2011). Lebedev et al. (Lebedev, Akedo et al. 2000) used a self-selective method to measure the particle velocity experimentally; however, the method suffers from several limitations such as generation of monodispersed aerosol and turbulence effect inside the vacuum chamber. Several computational studies have suggested optimization of nozzle geometry, powder size and type, the pressure

inside the deposition chamber for maximum performance in the AD (Hoffman, Holman et al. , Li, Singh et al. 2019). Park et al. (Park, Lee et al. 2011) studied converging-diverging nozzle and tried to find out the effect of shockwave nozzle geometry, chamber pressure, and substrate location on the impinging gas velocity. They proposed the necessities of nozzle divergence angle adjustment with the change in chamber pressure in order to retain optimal performance and optimal performance was assumed for minimum bow shock thickness. However, they haven't done any particle velocity measurement calculations. Similarly, Yeganeh et al. (Zabihi Yeganeh, Jadidi et al. 2019) modeled sonic nozzles also illustrated the effect of bow shock. In addition, they tried to calculate particle velocities by assuming drag from skin friction without considering the slip effect of the compressible gas. Li et al. (Li, Singh et al. 2019) proposed a new correlation based on neural network to calculate drag coefficient for the Knudsen number range of (10^{-4} - ∞) and Mach number 0<Ma<5. However, they have not considered particle Brownian motion.

In this study we have studied both slit (0.5 x 5 mm^2) and converging diverging (CD) slit nozzle having a throat of 0.45 x 10 mm^2 with an exit area of 1.85 x 10 mm^2 for aerosol deposition. For computational investigation of the particle velocities coming out of the nozzles, we have considered 2D shapes of the nozzles. Fluid flow inside the 2D nozzle geometry was solved using Ansys fluent where $k-\omega\ SST$ model was considered as a turbulence model as this model is well suited to wall bounded flow and flow having adverse pressure gradient (Balabel, Hegab et al. 2011). The inlet boundary condition was pressure inlet and was kept at atmospheric whereas the outlet pressure boundary condition was pressure outlet and was varied from 300 to 12000 Pa to understand the effect of different chamber pressure on the particle velocities impinging on the substrate. Aerosol deposition method holds a diverse flow, as it handles an wide flow area from subsonic to supersonic, creeping flow to highly turbulent flows and continuum to transitional

flows which makes it difficult to model with single conventional methods like Langevin equation (Ermak and Buckholz 1980) or Henderson correlation. For particle velocity calculations in the AD we have used Li's method (Li, Singh et al. 2019) as it correctly addresses the range of Knudsen number, Mach number and Reynolds number. We followed Li's proposed drag calculation and solved Newtons equation of motion with damping terms using leap-frog variant version of the velocity-verlet method coupled with fluid flow field obtained from Ansys Fluent (Ahmed and Gopalakrishnan 2019).

Figure 26 represents the geometry, boundary conditions and velocity contours at two different outlet pressures for the slit nozzle and silt CD nozzle. The inlet pressure was kept at standard atmospheric pressure. Velocity contours of both slit and slit CD nozzles depict that the bow shock thickness is dominant for outlet pressure of 1000 Pa compared to the outlet pressure of 5000 Pa. **Figure 27** represents gas particle velocity and corresponding gas velocity along the nozzle axis of slit CD nozzle for outlet pressure of 1000 Pa and 5000 Pa. Particle velocity was calculated using the Langevin equation for 500 nm TiO_2 particle. Here the dotted line represents the gas velocity and solid line represents the particle velocity and the same color represents the corresponding outlet pressure. It is interesting to observe that although gas velocity is higher at 1000 Pa compared to 5000 Pa, however particle velocity at 5000 Pa is higher compared to 1000 Pa. This is because of the bow shock on top of the substrate. Because of the bow shock, velocity of gas just above the substrate becomes subsonic and the gas density is also higher in the bow shock region which induces more particle drag and hence reduces particle velocity.

In order to investigate more about the effect of chamber pressure on particle impinging velocities we have calculated particle velocities for different sizes of particles at different outlet pressure of

slit CD nozzle. **Figure 28** represents the calculated particle velocities for different pressure and different sizes of particles. It is interesting to observe that the highest particle velocity was obtained for a pressure of 5000 Pa. Above the 5000 Pa particle velocity continuously decreases and this is due to the higher drag on the particle. On the other hand, below 5000 Pa particle velocity continuously decreased until 2000 Pa and then again increased for the pressure below 2000. The reason behind the decrease until 2000 is because of bow shock and higher gas densities. Below 2000 Pa although bow shock is present, however, because of low gas density the drag on particle is also less which help to rise in velocity. A careful observation of the particle velocities at 300 Pa shows that although particle velocity increased from 2000 Pa, however the larges particles (> 300 nm) velocity at 300 Pa is less than that of 5000 Pa. On the other hand, smaller particles (<300 nm) attained a higher velocity at 300 Pa compared to the 500 Pa. This clearly indicates that at lower pressure due to less density of gas, heavier particles don't get enough kinetic energy to be accelerated and smaller particles get less drag and attain higher velocity. This investigation gives a clear insight that to achieve highest kinetic energy from particles less than 300 nm it is better to decrease the chamber pressure below 300 Pa, however, for larger particles it would be better to keep the pressure higher until the flow is over-expanded and bow shock thickness is minimum.

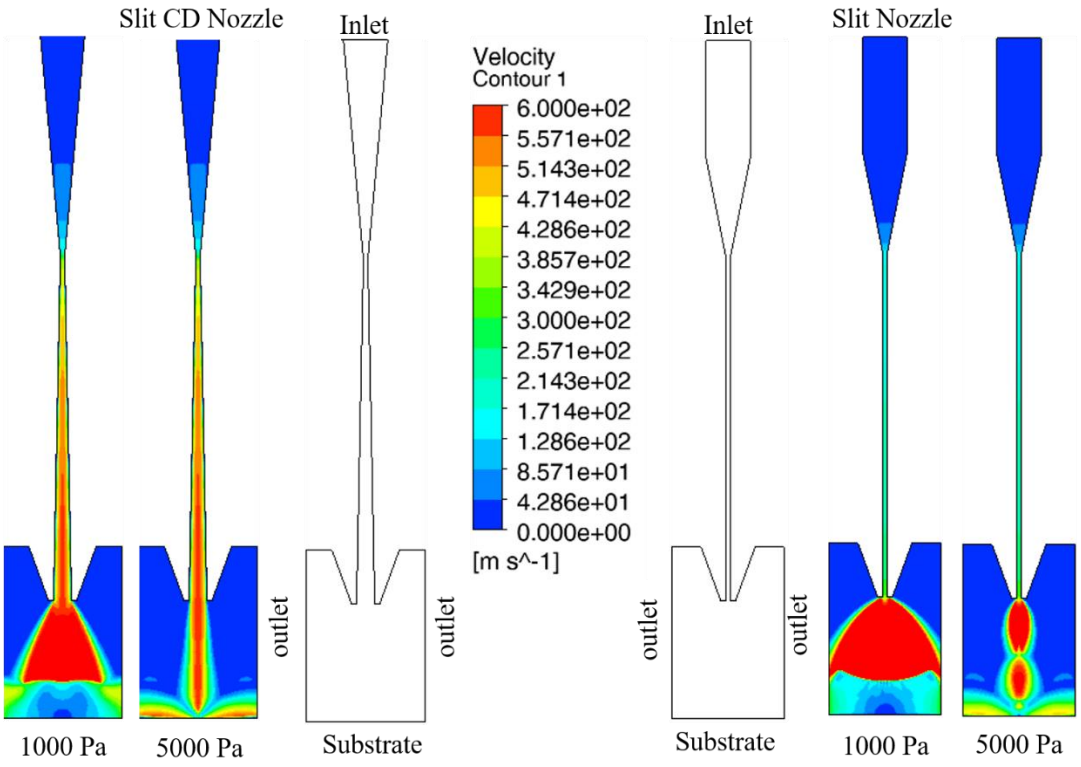

Figure 26: Slit and Slit CD nozzle boundary conditions and velocity contours

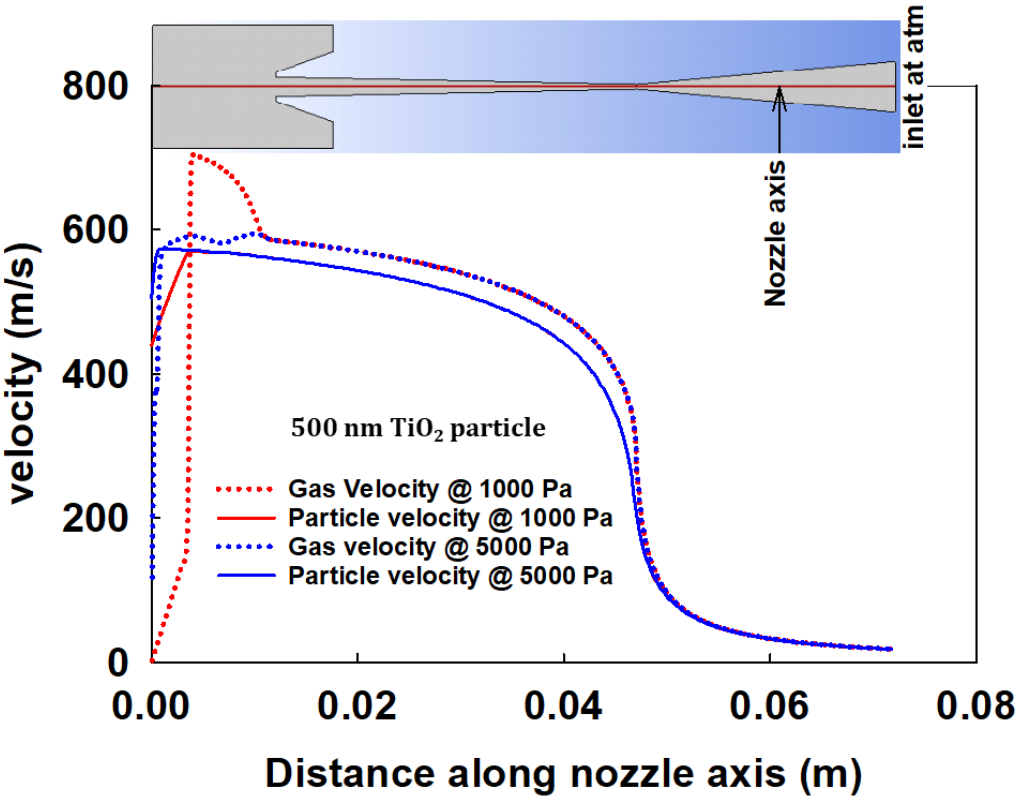

Figure 27: Gas and particle velocity for Slit CD nozzle

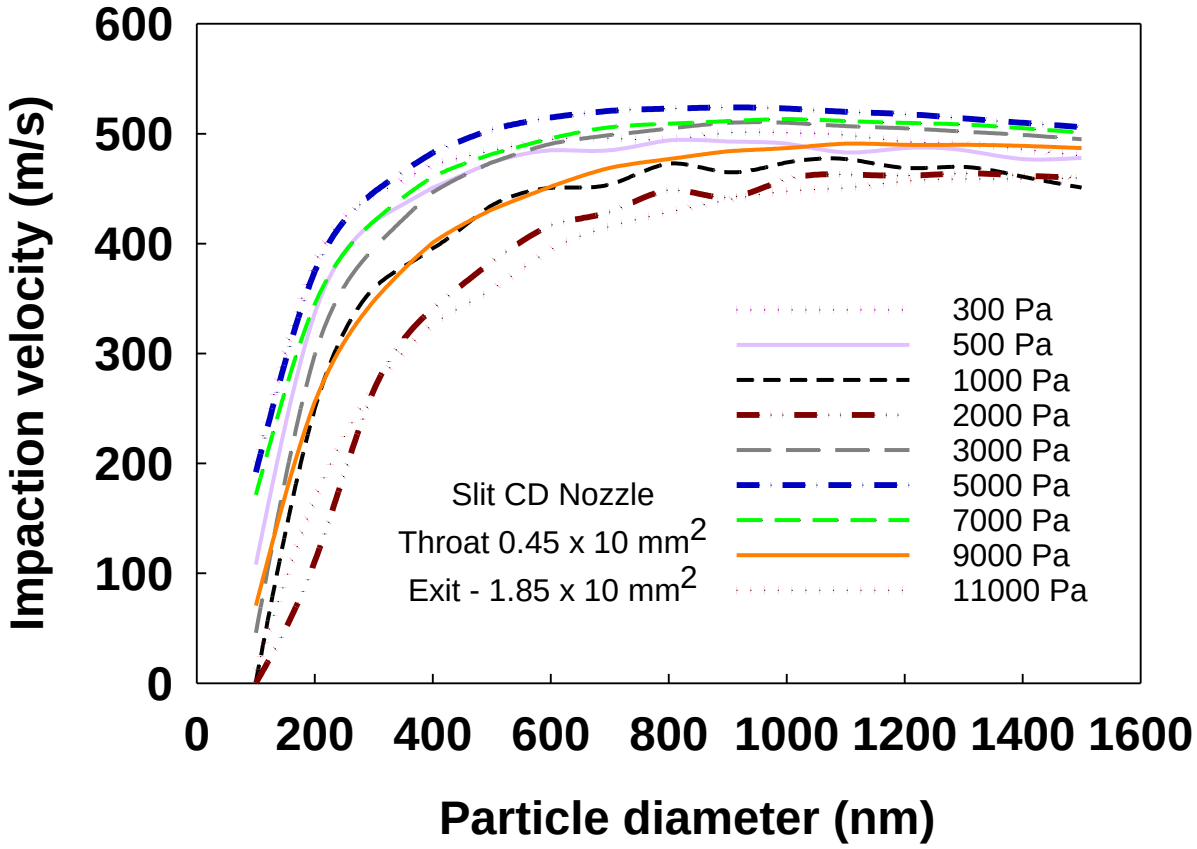

Figure 28: Particle impinging velocities at the substrate for different chamber pressure

Results

Following the particle treatment methodology and aerosolizing with a novel aerosol generator system, we have successfully fabricated a thin film of TiO_2 on glass substrate. In addition to glass we have also developed a coating on different metallic and nonmetallic substrates. The following subsections are organized with coating characterization and observations during experimentation.

Coating of TiO2 on glass:

Figure 29 represents some TiO_2 coated glass samples where it is clearly visible of having different thicknesses. The low thickness makes the color faint, whereas for higher thickness, the

transparency is less and even completely opaque in case of several micron thicknesses. We were able to develop a maximum thickness of 13 μm on glass substrate. **Figure 30** represents two different thickness of TiO_2 coating on glass substrate. In **Figure 31** the left figure shows the surface image of TiO_2 while the right-side figure shows the XRD pattern of the raw powder, milled powder and the deposited film. A careful observation of the XRD pattern reveals that the rightmost four peaks in the raw and milled powder are missing or insignificant in the developed TiO_2 coating. A similar case was observed by Park et al. (Park, Kim et al. 2014). They have reported changes in crystal structure in the as-deposited film and they also observed further changes after annealing the film. The surface roughness of the thin film varies from nano to micron-scale depending on the thickness of the developed film. Surface roughness was measured by Keyence digital microscope (VHX 7000 with VH-Z 500R lens). **Figure 32** represents the surface of the coating over a line measured by the digital microscope. The arithmetic mean roughness shows around 100 nm.

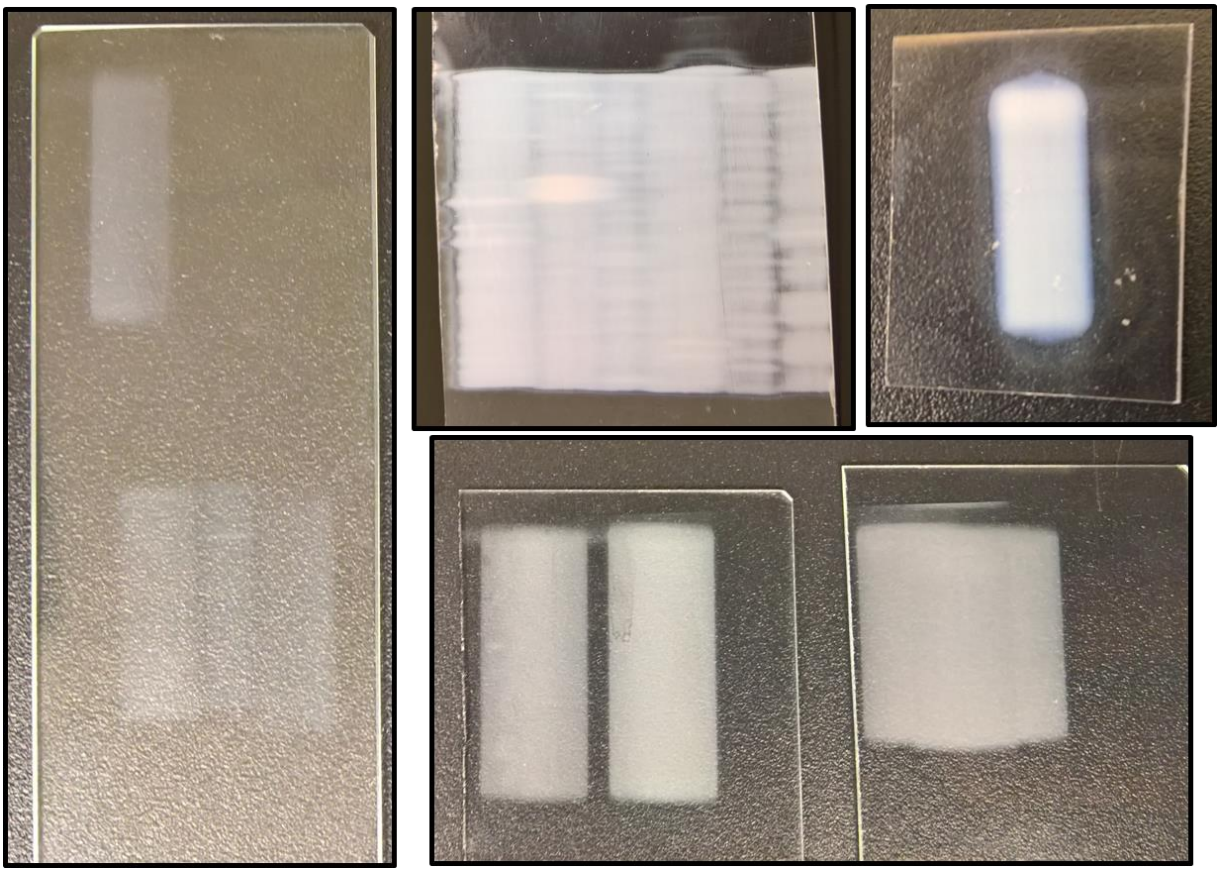

Figure 29: TiO_2 coated glass substrates

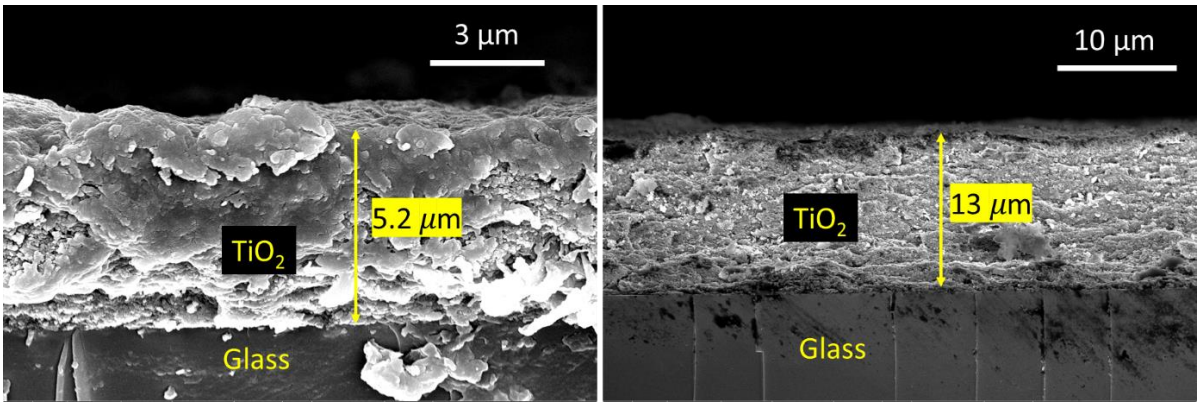

Figure 30: Cross-sectional image of the TiO_2 Coating on a glass substrate

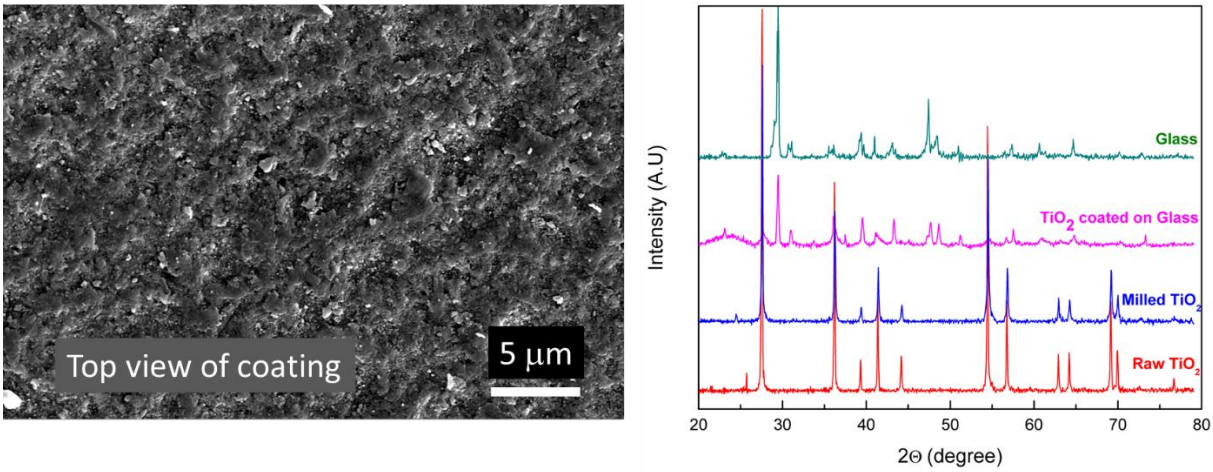

Figure 31: Top view of coating and XRD results

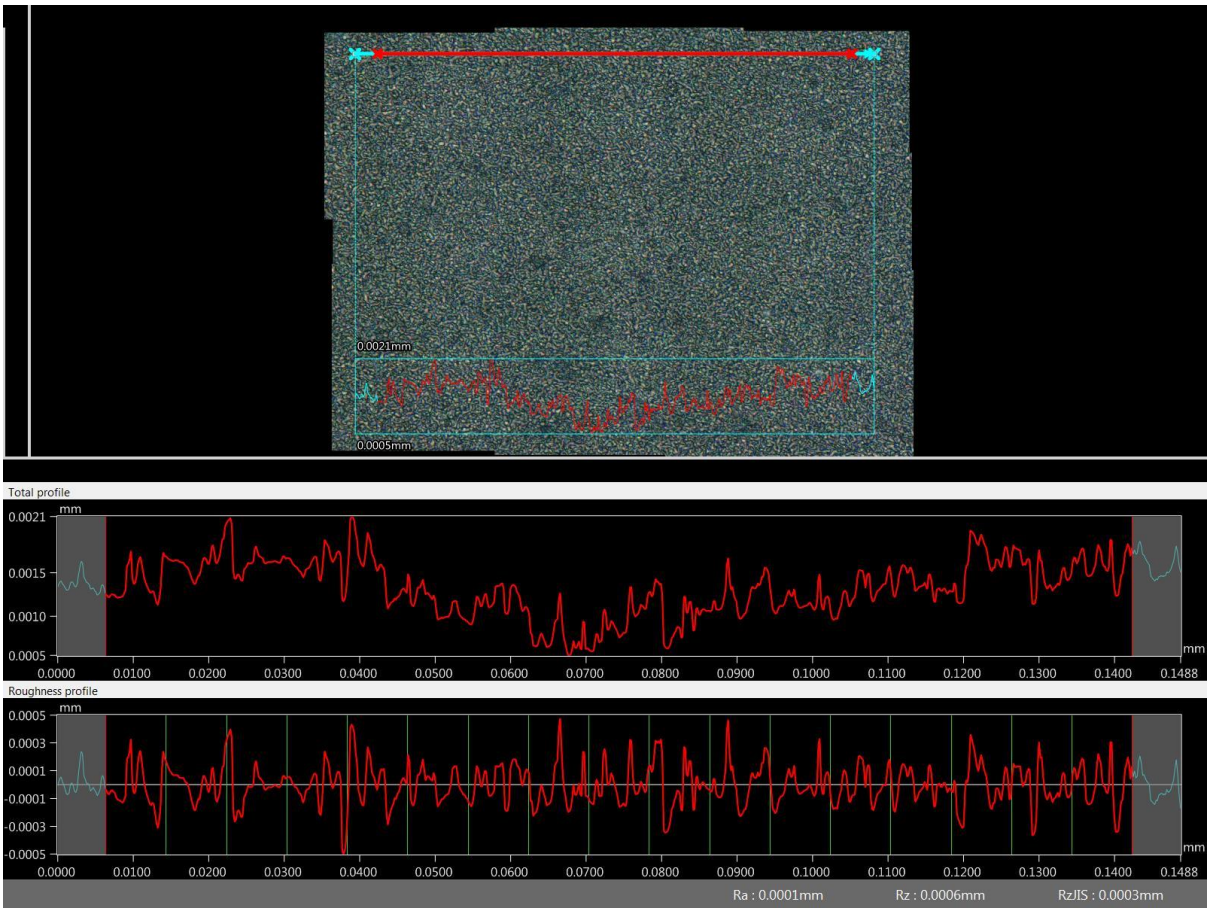

Figure 32: Surface roughness of coating measured by digital microscope

Effect of deposition chamber pressure:

As discussed before, chamber pressure plays an important role on the deposition performance as the pressure determines the drag, kinetic energy of the ambient gas and the presence of bow shock. To check the effect of deposition chamber pressure, we have developed thin film at various pressure for a nozzle with constant atmospheric aerosol flowrate. **Figure 33** represents the images of thin film for different chamber pressure fabricated using 0.5 x 5 mm^2 slit nozzle. The left most film was fabricated at 650 Pa and the right most one was at 7000 Pa. Intermediate pressures are 800 Pa, 900 Pa, 1000 Pa, 1500 Pa, 2000 Pa, 3000 Pa, 4000 Pa, 5000 Pa and 6000 Pa. A careful observation of the film color indicates that film density decreases from 650 Pa to 2000 Pa and then increased in 3000 Pa and then gradually decreased over 3000 Pa which was predicted from simulation results.

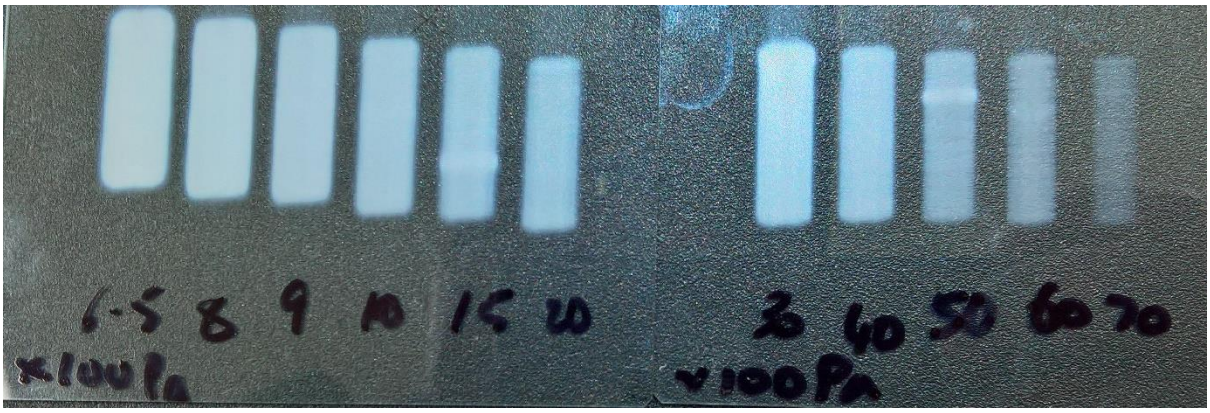

Figure 33: Thin film of TiO_2 developed under various chamber pressure. Here chamber pressure varied from 650 to 7000 Pa

Addition of virtual impactor:

Ball-milled powder contains a wide range particle sizes, which makes polydisperse aerosol after aerosolization. Polydisperse aerosol showed less control over the deposition

thickness as very small particles don't form the coating, large particles erode the coating and substrate, and only medium sized particles contribute to the coating (Hanft, Exner et al. 2015). In order to restrict the large particles going through the nozzle we have passed the polydisperse aerosol through a homemade virtual impactor before going through the nozzle. **Figure 34** shows the schematic of the virtual impactor that was used for aerodynamic particle sizing. The virtual impactor was designed to captured particles above 1 micron and it was successful in capturing most of the large particles. SEM image of the powder samples collected before, after and from inside the virtual impactor confirms the large particle arrestment (**Figure 35**). The top left image represents the ball-milled powder that were passed through the virtual impactor to remove particles larger than 1 micron. The top right image shows the arrested particles image under SEM and confirms the presence of significantly large particles. Similarly, the bottom picture shows the powder particle sample after SEM. **Figure 36** represents the image of thin-film with and without virtual impactor. Thin-film fabricated without virtual impactor shows an eroded patch in the middle of the film due to the impaction of larger particles. On the other hand, the film fabricated with virtual impactor is relatively uniform. The one large eroding mark on the film without virtual impactor is from the sudden uncontrolled burst of powder particles that impacted the coating. However, the use of virtual impactor showed a prominent result in building up the uniform film thickness.

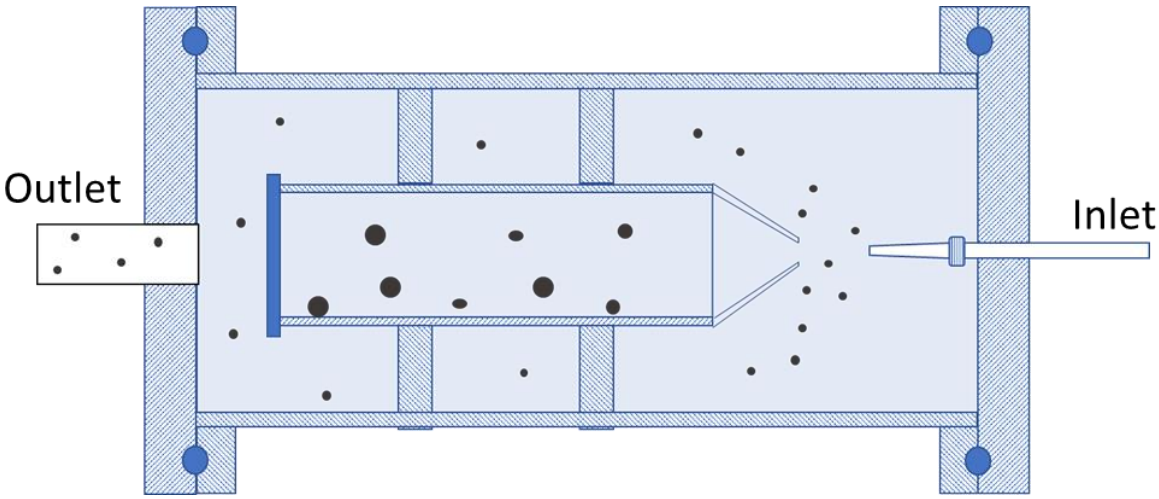

Figure 34: Schematic diagram of the virtual impactor

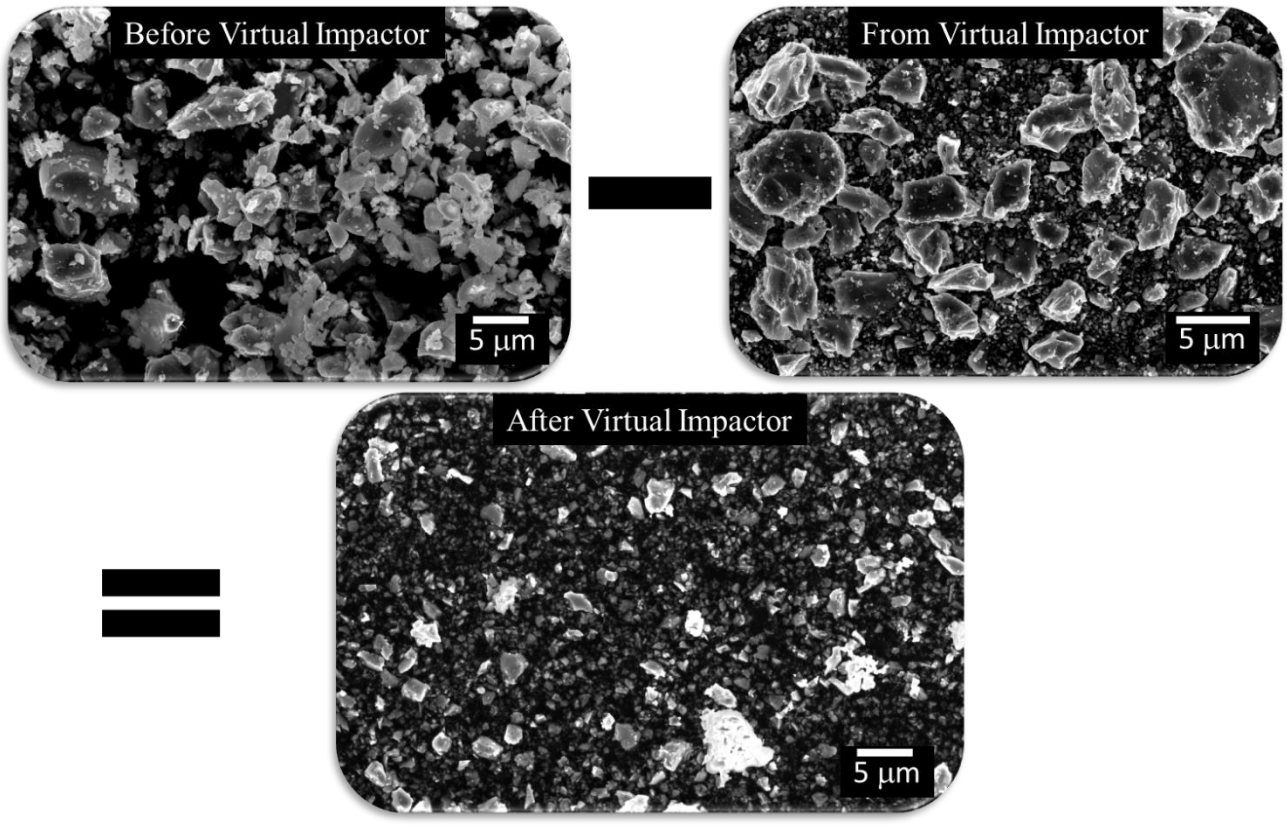

Figure 35: SEM images of particles collected before after and from virtual impactor

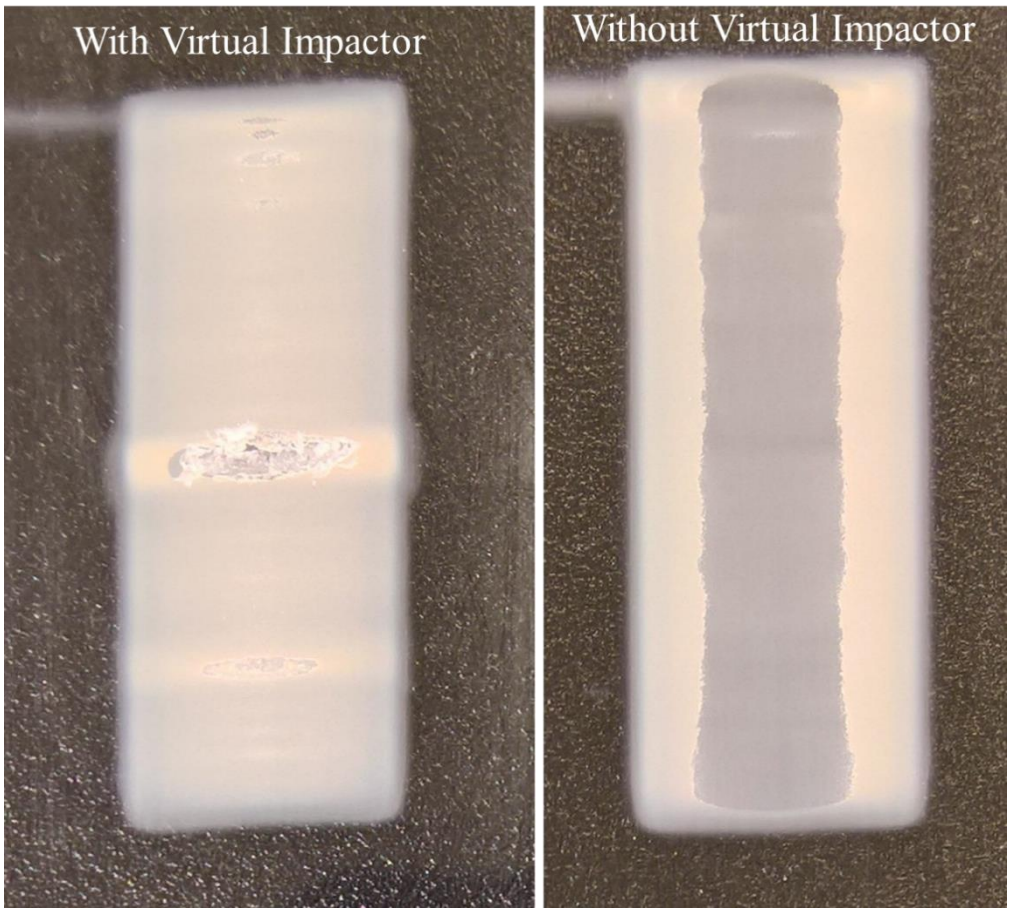

Figure 36: TiO_2 film on glass substrate with and without virtual impactor

Effect of multiple layering:

Several research works reported increasing film thickness over increasing number of passes in aerosol deposition method (Fuchita, Tokizaki et al. 2010, Hanft, Glosse et al. 2018). In this study it was observed that although film thickness increases with number of passes until several number of passes, however after that film thickness started to decrease with the increasing number of passes and at some point, removes the film. **Figure 37** represents the images of coating after different number of passes. From visual observation of the images it is clear that, although initially the film thickness developed with increasing number of passes however, thickness decreased with higher number of passes. **Figure 38** shows the measured film

thickness based on SEM images of cross-section of the films. From **Figure 38** it can be observed that film thickness increased until 8 passes and started to decrease after that. This might be due to the hammering effect on the glass substrate. confirms the observation based on the **Figure 37**.

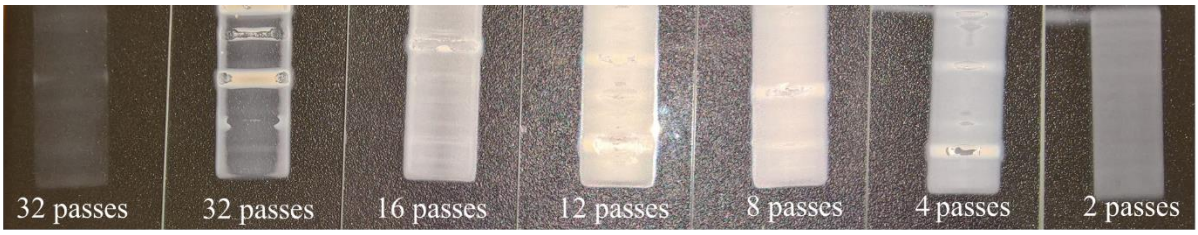

Figure 37: Images of TiO_2 thin films for a different number of passes.

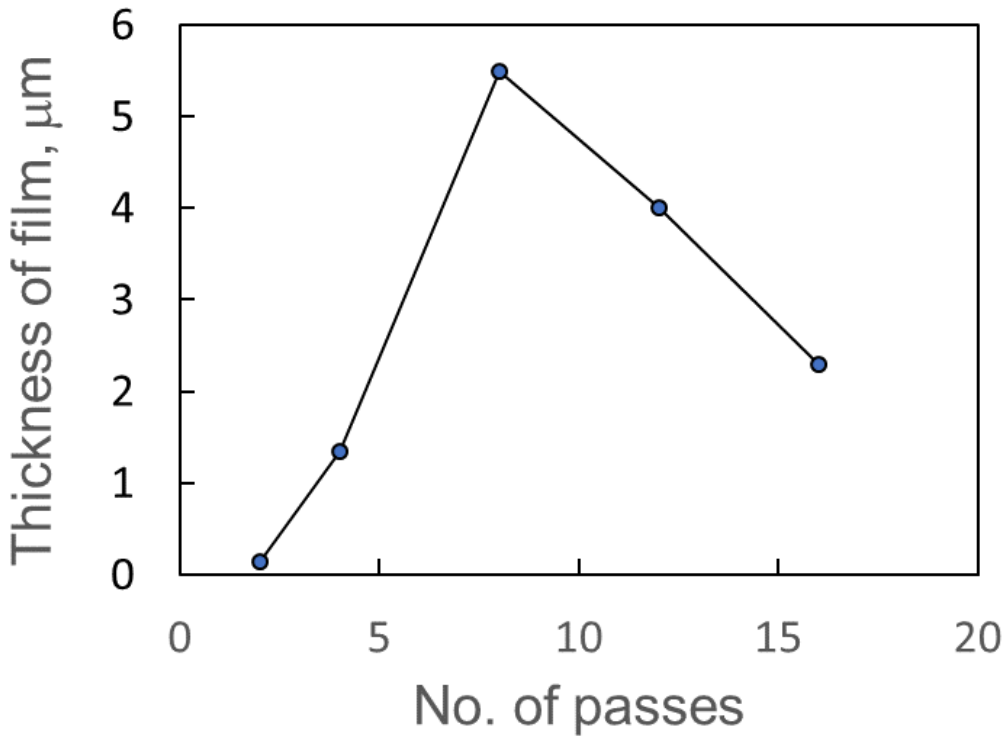

Figure 38: Film thickness vs. number of passes

Micro scratch resistance testing:

To understand the adhesion strength of the film, five TiO_2 coated samples of a various number of scans were tested using a micro scratch resistance testing method. The tests were performed by MachAction, Inc a coating test company. The testing procedures followed a modified ASTM C1624 standard to scratch the film material with a diamond scratch tip. A 20 µm radius diamond spherical tip was employed for the scratch measurements. The system and the scratch tip were validated on a TiN reference sample before the experiments were conducted on Honeywell samples.

Table 3: Micro scratch testing parameters

Scratch mode:	**Progressive**
Max Load (N)	2.5, 3.5
Scratch Length (mm)	1, 1.4
Scratch Speed (mm/min)	2
Loading Rate (N/min)	5
Pre/Post Scan Load (mN)	10
Scratch Tracks per sample	3
Scratch Tip Type	Sphero-conical
Tip Material	Diamond
Scratch Tip Radius (µm)	20

A progressive scratch mode was employed where the normal load keeps increasing while scratching through the sample surface. In addition, a pre-scan and a post-scan were employed before the scratch to define the profile of the sample surface and to determine the residual depth after elastic recovery of sample surface respectively. The real scratch depth was calculated by subtracting the surface profile (pre-scan) from the raw data. A spherical diamond tip was employed for such work to achieve symmetrical scratch distribution. Two sets of test parameters are employed as coatings have different thicknesses and strengths. But the loading rate and scratch speed are the same, thus the data is directly comparable. **Table 3** represents the Micro scratch testing parameters.

For each sample 3 sets of data were collected. **Table 4** tabulates some results based on the scratch testing. Critical Normal Scratch Load (LC1) is used to describe the onset of coating crack failure (Chevron Type). Such a failure mechanism is most likely cohesive and is confined within the coating structure. LC1 is more related to the coating mechanical properties rather than the adhesion strength. Critical Normal Scratch Load (LC2) is used to describe the onset of coating delamination failure. LC2 is related to coating adhesion strength. Critical Normal Scratch Load (LC3) is used to describe the onset of substrate fracture failure. As the glass substrate is brittle, the substrate cracks before the coating are delaminated from the substrate, which again indicates the strong adhesion of the coating. As LC3 is solely related to glass substrate rather than the coating, therefore, it is suggested to employ a much harder and ductile substrate such as stainless steel for this study.

2s and 16s coatings are very thin (~1µm). They are difficult to be delaminated from the substrate by scratch as the glass substrate fractures before coating failure. Both coatings show decent integrality with no cracking or delamination through scratch. But 16s surface is noticeably

rougher than the 2s surface. 4s coating is thicker (~2µm) than 2s and 16s but doesn't show coating delamination moment either before substrate fracture. However, 4s shows a cohesive coating cracking moment (LC1), which is related to coating mechanical properties. 8s and 12s coatings are thicker (~5µm) than others. Like 4s, 8s and 12s show LC1 moment of coating cohesive cracking, but they also show LC2, which is the adhesive failure of the coating.
12s has a greater LC2 value than 8s, which indicates a better adhesion strength. To assess adhesion strength of 2s, 4s, and 16s coatings, it is suggested that the coatings should be put on a harder and more ductile substrate, such as stainless-steel coupon.

Table 4: Comparison of critical loads of failure

		2 scans	4 scans	8 scans	12 scans	16 scans
Max scratch load		2.5 N	3.5 N	2.5 N	3.5 N	3.5 N
Scratch length		1 mm	1.4 mm	1 mm	1.4 mm	1.4mm
LC1 Optic	Data : 1	--.--	0.599	0.622	0.645	--.--
[N]	Data : 2	--.--	0.686	0.639	0.633	--.--
	Data : 3	--.--	0.634	0.748	0.712	--.--
	Mean	--.--	0.64	0.67	0.663	--.--
	Std Dev	--.--	0.043	0.069	0.043	--.--
LC2 Optic	Data : 1	--.--	--.--	1.672	2.55	--.--
[N]	Data : 2	--.--	--.--	1.751	2.517	--.--
	Data : 3	--.--	--.--	1.767	2.495	--.--
	Mean	--.--	--.--	1.73	2.52	--.--
	Std Dev	--.--	--.--	0.051	0.028	--.--
LC3 Optic	Data : 1	1.846	3.149	--.--	--.--	1.735
[N]	Data : 2	1.797	3.164	--.--	--.--	2.061
	Data : 3	1.907	3.033	--.--	--.--	2.316
	Mean	1.85	3.115	--.--	--.--	2.037
	Std Dev	0.055	0.071	--.--	--.--	0.291

Conclusions

Titanium dioxide film on glass has a wide application area because of its photolytic and photochromatic applications. Fabrication of TiO_2 thin film using aerosol deposition method would greatly be accepted as it is a one-step chemical free, solve free room temperature method and obtains reportedly higher strength compare to other methods of fabrication. However, this method is facing some limitations and needs proper solution strategies to address those for commercial applications. This study finds few of the limitations and tried to explore some possible solutions.

The main limitation is availability of the proper size of deagglomerated powder particles. The commercially available powders although mentioned to have different sizes of particles, however the true size measure under SEM found to have less than 500 nm particles. For aerosol deposition of TiO_2 particles it was found that particles over 500 nm and below 1 micron showed the best deposition performance. The basis of this justification is that commercially available powders were aerosolized and found to have either very low or no contribution to deposition. This study and some other study successfully fabricated thin film of TiO_2 by prepossessing the commercially available powder materials. Although the prepossessing steps help to get successful deposition of particles, however, prepossessing is very cumbersome, may change particle crystalline structure and transforms to wide size distribution of particles which finally contributes to a less control over deposited film quality and huge loss of powders particles. In order to address this limitation of AD, the first step would be producing the right size of particles with a very narrow size range.

The second important aspect is particle kinetics, which is a function of particle size, nozzle aerodynamics and chamber pressure. With the aid of computation analysis this study showed that to achieve the right kinetic energy converging-diverging silt nozzles could be

benefited over only slit nozzles and the selection of proper chamber pressure is very important to achieve the proper particle impaction velocity.

This study found that virtual impactor could be a good tool to use in order to improve the quality of the deposited film. Particles tries to form agglomerates by nature and during aerosolization, agglomerates also aerosolizes like single particles. Agglomerates or single large particles in aerosol has detrimental effect on the aerosol thin film and to prevent these agglomerates or large particles virtual impactor could be a good tool to use. It was observed that virtual impactor successfully captured large particles and improved the deposited film quality to a great extent.

To build up the thickness of the deposited film, it is necessary to do repeated coating/layering. It was observed that although multiple layering helps to build up the deposited thickness, however, after certain number of layering the film started to erode and at some point, the film might be even completely erased. This might be due to repeating impaction of high energetic particles on the deposited film, which ultimately breaks the film bonding. So, it is recommended to select an optimum number of layering, which would contribute to the thickness buildup of the deposited film and needs further investigation.

Conclusions

The dissertation comprises of three different studies on aerosol science and engineering which are aerosol generation, aerosol focusing and application of aerosol for thin film fabrication using aerosol impact consolidation method. The study on aerosol focusing proposed a new method of focusing nanoparticles similar to electrons and ions based on electrostatics. This study revealed that nanoparticles could also be focused as electrons and ions provided, they are charged to a higher state. The study identified some critical parameters in focusing and described their effect on the deposition performance. The study also revealed that below a certain pressure the focusing performance is close to the vacuum state which omits the necessity of stringent vacuum. The concept of focusing particles with electrostatics demand some more parametric analysis to understand the final beam width of the particle, such as effect of initial angle of the particles entering the lens, effect of lens geometry and particle concentration on the focusing performance which are considered as future studies.

The scalable high concentration ultrasonic aerosol generator is a great tool for generating aerosol from powder phase materials. This method uses ultrasonic energy to levitate powder particles from powder bed and mix with air. The method offers a great benefit over the conventional aerosol generator method such that it doesn't need any gas mass flow controller, or fluid power to levitate powder and generate aerosol. Aerosol concentration can be varied with the ultrasonic power supplied to the ultrasonic transducers. Another benefit of method is that ultrasonic vibration helps to separate the loosely agglomerated particles which in result produces better de-agglomerated aerosol.

Lastly, TiO_2 thin film fabrication using aerosol impact consolidation method is a one-step room temperature method offers a great benefit over the conventional methods such as chemical vapor

deposition or plasma enhanced deposition. This study successfully developed TiO_2 film on glass substrate and described the powder preparation procedures in detail. In aerosol deposition method some research suggested that thickness build up is proportional to the number of scans/repetitions. However, in this study it was observed that although repeated coating initially builds up thickness of the film however started to erode the film after certain number of repetitions and may even completely remove the film with a greater number of repetitions. In addition, the use of virtual impactor found to have positive impact on increasing the rate of deposition. Another important parameter is the deposition chamber pressure which determines the drag on the particle and particle impaction speed. This study showed that very low pressure doesn't confirm the highest velocity rather there is an optimum pressure where particle velocity could be maximum. Above and below the optimum chamber pressure particle velocity is less. This study suggests that as ball milling is a cumbersome process and has no control over particle sizes, therefore, it is necessary to investigate some other methods of preparing submicron size (500 nm to 1 μm) aerosol particles with a narrow size distribution for aerosol impact consolidation method.

References

Abdelsalam, D. G. and M. Stanislas (2017). "Spherical aberration measurement of a microscope objective by use of calibrated spherical particles." Applied Optics **56**(16): 4766-4771.

Adams, A. and F. H. Read (1972). "Electrostatic cylinder lenses II: Three element einzel lenses." Journal of Physics E: Scientific Instruments **5**(2): 150-155.

Ahmed, R. and R. Gopalakrishnan (2019). "Computational study of electrostatic focusing of aerosol nanoparticles using an einzel lens." Journal of Aerosol Science **137**: 105443.

Aitken, J. (1881). "Dust, Fogs, and Clouds." Nature **23**(591): 384-385.

Akedo, J. (2002). "Aerosol Deposition Method (ADM) : A novel method of PZT thick films producing for microactuators." J. Crystal Growth **235**: 415.

Akedo, J. (2008). "Room Temperature Impact Consolidation (RTIC) of Fine Ceramic Powder by Aerosol Deposition Method and Applications to Microdevices." Journal of Thermal Spray Technology **17**(2): 181-198.

Akedo, J., M. Ichiki, K. Kikuchi and R. Maeda (1998). "Jet molding system for realization of three-dimensional micro-structures." Sensors and Actuators A: Physical **69**(1): 106-112.

Akedo, J. and M. Lebedev (1999). "Microstructure and Electrical Properties of Lead Zirconate Titanate (Pb(Zr52/Ti48)O3) Thick Films Deposited by Aerosol Deposition Method." Japanese Journal of Applied Physics **38**(Part 1, No. 9B): 5397-5401.

Allen, J. and R. K. Gould (1981). "Mass spectrometric analyzer for individual aerosol particles." Review of Scientific Instruments **52**(6): 804-809.

Au - Yi, J., B. T. Au - Chen, D. Au - Schwegler-Berry, D. Au - Frazer, V. Au - Castranova, C. Au - McBride, T. L. Au - Knuckles, P. A. Au - Stapleton, V. C. Au - Minarchick and T. R. Au -

Nurkiewicz (2013). "Whole-Body Nanoparticle Aerosol Inhalation Exposures." JoVE(75): e50263.

Awad, H., M. M. Khamis and A. El-Aneed (2015). "Mass Spectrometry, Review of the Basics: Ionization." Applied Spectroscopy Reviews **50**(2): 158-175.

Balabel, A., A. M. Hegab, M. Nasr and S. M. El-Behery (2011). "Assessment of turbulence modeling for gas flow in two-dimensional convergent–divergent rocket nozzle." Applied Mathematical Modelling **35**(7): 3408-3422.

Barbé, C. J., F. Arendse, P. Comte, M. Jirousek, F. Lenzmann, V. Shklover and M. Grätzel (1997). "Nanocrystalline Titanium Oxide Electrodes for Photovoltaic Applications." Journal of the American Ceramic Society **80**(12): 3157-3171.

Baron, P. (2010). Generation and Behavior of Airborne Particles (Aerosols), PowerPoint Presentation. US Department of Health and Human Services, Centers ….

Biskos, G., V. Vons, C. U. Yurteri and A. Schmidt-Ott (2008). "Generation and Sizing of Particles for Aerosol-Based Nanotechnology." KONA Powder and Particle Journal **26**: 13-35.

Buesser, B., A. J. Gröhn and S. E. Pratsinis (2011). "Sintering Rate and Mechanism of TiO2 Nanoparticles by Molecular Dynamics." The Journal of Physical Chemistry C **115**(22): 11030-11035.

Calvert, G., M. Ghadiri and R. Tweedie (2009). "Aerodynamic dispersion of cohesive powders: A review of understanding and technology." Advanced Powder Technology **20**(1): 4-16.

Cao, J. (2017). "The Importance of Aerosols in the Earth System: Science and Engineering Perspectives." Aerosol Science and Engineering **1**(1): 1-6.

Chandrasekhar, S. (1943). "Stochastic Problems in Physics and Astronomy." Reviews of Modern Physics **15**: 1-89.

Chang, P. S., J. R. Brock and I. Trachtenberg (1993). "A theoretical investigation of low pressure particle impaction in a highly underexpanded sonic impinging slit jet." Journal of Aerosol Science **24**(1): 31-44.

Chang, T., M. Thomson, E. Kratschmer, H. Kim, M. Yu, K. Lee, S. Rishton, B. Hussey and S. Zolgharnain (1996). "Electron-beam microcolumns for lithography and related applications." Journal of Vacuum Science & Technology B: Microelectronics and Nanometer Structures Processing, Measurement, and Phenomena **14**(6): 3774-3781.

Chen, H., S. W. Lee, T. H. Kim and B. Y. Hur (2006). "Photocatalytic decomposition of benzene with plasma sprayed TiO2-based coatings on foamed aluminum." Journal of the European Ceramic Society **26**(12): 2231-2239.

Chew, N. Y. and H.-K. Chan (2002). "Effect of powder polydispersity on aerosol generation." J Pharm Pharm Sci **5**(2): 162-168.

Choi, H., S. Kang, W. Jung, Y.-h. Jung, S. J. Park, D. S. Kim and M. Choi (2015). "Controlled electrostatic focusing of charged aerosol nanoparticles via an electrified mask." Journal of Aerosol Science **88**: 90-97.

Chun, D. M., M. H. Kim, J. C. Lee and S. H. Ahn (2008). "TiO2 coating on metal and polymer substrates by nano-particle deposition system (NPDS)." CIRP Annals - Manufacturing Technology **57**(1): 551-554.

Ciric, D., I. Terzic and J. Vukanic (1976). "Symmetrical three-tube unipotential lens. II. First-order focal properties." Journal of Physics E: Scientific Instruments **9**(10): 839-847.

Core, J. E. (1991). Chapter 9 - Application of Receptor Modeling to Solving Local Air Quality Problems. Data Handling in Science and Technology. P. K. Hopke, Elsevier. **7:** 299-319.

Cumeras, R., E. Figueras, C. E. Davis, J. I. Baumbach and I. Gràcia (2015). "Review on ion mobility spectrometry. Part 1: current instrumentation." The Analyst **140**(5): 1376-1390.

Dahneke, B. and Y. Cheng (1979). "Properties of continuum source particle beams. I. Calculation methods and results." Journal of Aerosol Science **10**(3): 257-274.

Dahneke, B. and H. Flachsbart (1972). "An aerosol beam spectrometer." Journal of Aerosol Science **3**(5): 345-349.

Daimon, H., H. Matsuda, M. Kato and M. Kudo (2010). Spherical aberration corrected electrostatic lens, input lens, electron spectrometer, photoemission electron microscope and measuring system, Google Patents.

Daneshian, B. and H. Assadi (2014). "Impact Behavior of Intrinsically Brittle Nanoparticles: A Molecular Dynamics Perspective." Journal of Thermal Spray Technology **23**(3): 541-550.

De La Mora, J. F. and P. Riesco-Chueca (1988). "Aerodynamic focusing of particles in a carrier gas." Journal of Fluid Mechanics **195**: 1-21.

Deng, R., X. Zhang, K. A. Smith, J. Wormhoudt, D. K. Lewis and A. Freedman (2008). "Focusing particles with diameters of 1 to 10 microns into beams at atmospheric pressure " Aerosol Science and Technology **42**(11): 899-915.

Di Fonzo, F., A. Gidwani, M. Fan, D. Neumann, D. Iordanoglou, J. Heberlein, P. McMurry, S. Girshick, N. Tymiak and W. Gerberich (2000). "Focused nanoparticle-beam deposition of patterned microstructures." Applied Physics Letters **77**(6): 910-912.

Di, H., Z. Wang and D. Hua (2019). "Precise size distribution measurement of aerosol particles and fog droplets in the open atmosphere." Optics Express **27**(12): A890-A908.

Ding, Y. and M. Riediker (2016). "A System to Create Stable Nanoparticle Aerosols from Nanopowders." Journal of visualized experiments : JoVE(113): 54414.

Dong, Y., A. Bapat, S. Hilchie, U. Kortshagen and S. Campbell (2004). "Generation of nano-sized free standing single crystal silicon particles." Journal of Vacuum Science & Technology B: Microelectronics and Nanometer Structures Processing, Measurement, and Phenomena **22**(4): 1923-1930.

Du, L., T. Coyle, K. Chien, L. Pershin, T. Li and M. Golozar (2015). "Titanium Dioxide Coating Prepared by Use of a Suspension-Solution Plasma-Spray Process." Journal of Thermal Spray Technology **24**(6): 915-924.

Dunst, P., P. Bornmann, T. Hemsel and W. Sextro (2018). "Vibration-Assisted Handling of Dry Fine Powders." Actuators **7**(2): 18.

Ermak, D. L. and H. Buckholz (1980). "Numerical integration of the Langevin equation: Monte Carlo simulation." Journal of Computational Physics **35**(2): 169-182.

Evtushenko, Y. M., S. V. Romashkin, N. S. Trofimov and T. K. Chekhlova (2015). "Optical Properties of TiO2 Thin Films." Physics Procedia **73**: 100-107.

Exner, J., M. Hahn, M. Schubert, D. Hanft, P. Fuierer and R. Moos (2015). "Powder requirements for aerosol deposition of alumina films." Advanced Powder Technology **26**(4): 1143-1151.

Exner, J., M. Schubert, D. Hanft, J. Kita and R. Moos (2019). "How to treat powders for the room temperature aerosol deposition method to avoid porous, low strength ceramic films." Journal of the European Ceramic Society **39**(2): 592-600.

Fan, S. Q., G. J. Yang, C. J. Li, G. J. Liu, C. X. Li and L. Z. Zhang (2006). "Characterization of microstructure of Nano-TiO2 coating deposited by vacuum cold spraying." Journal of Thermal Spray Technology **15**(4): 513-517.

Fernández-Maestre, R. (2012). "Ion mobility spectrometry: History, characteristics and applications." Revista U.D.C.A Actualidad & Divulgación Científica **15**: 467-479.

Fernandez de la Mora, J. (2006). "Aerodynamic focusing in spatially periodic flows: Two-dimensional symmetric and antisymmetric channels." Journal of Aerosol Science **37**(3): 323-339.

Fernandez De La Mora, J. and P. Riesco-Chueca (2006). "Aerodynamic focusing of particles in a carrier gas." Journal of Fluid Mechanics **195**: 1-21.

Fuchita, E., E. Tokizaki and Y. Sakka (2010). "Formation of zirconia films by the aerosol gas deposition method." Journal of the Ceramic Society of Japan **118**(1380): 767-770.

Gamero-Castaño, M. and J. F. d. l. Mora (2000). "Kinetics of small ion evaporation from the charge and mass distribution of multiply charged clusters in electrosprays." Journal of Mass Spectrometry **35**(7): 790-803.

German, R. M. (2001). Sintering. Encyclopedia of Materials: Science and Technology. K. H. J. Buschow, R. W. Cahn, M. C. Flemings et al. Oxford, Elsevier**:** 8641-8643.

Gopalakrishnan, R., P. H. McMurry and C. J. Hogan (2015). "The Bipolar Diffusion Charging of Nanoparticles: A Review and Development of Approaches for Non-Spherical Particles." Aerosol Science and Technology **49**(12): 1181-1194.

Gopalakrishnan, R., M. J. Meredith, C. Larriba-Andaluz and C. J. Hogan Jr (2013). "Brownian dynamics determination of the bipolar steady state charge distribution on spheres and non-spheres in the transition regime." Journal of Aerosol Science **63**: 126-145.

Grätzel, M. (2001). "Photoelectrochemical cells." nature **414**(6861): 338-344.

Hall, T. and W. Beeman (1976). "Secondary electron emission from beams of polystyrene latex spheres." Journal of Applied Physics **47**(12): 5222-5225.

Hanft, D., J. Exner, M. Schubert, T. Stöcker, P. Fuierer and R. Moos (2015). "An Overview of the Aerosol Deposition Method: Process Fundamentals and New Trends in Materials Applications." Journal of Ceramic Science and Technology **6**: 147-182.

Hanft, D., P. Glosse, S. Denneler, T. Berthold, M. Oomen, S. Kauffmann-Weiss, F. Weis, W. Häßler, B. Holzapfel and R. Moos (2018). "The aerosol deposition method: a modified aerosol generation unit to improve coating quality." Materials **11**(9): 1572.

Hanft, D., P. Glosse, S. Denneler, T. Berthold, M. Oomen, S. Kauffmann-Weiss, F. Weis, W. Häßler, B. Holzapfel and R. Moos (2018). "The Aerosol Deposition Method: A Modified Aerosol Generation Unit to Improve Coating Quality." Materials (Basel, Switzerland) **11**(9): 1572.

Heise, F. and O. Rang (1949). "Experimental investigations of the electrostatic einzel lens." Optik **5**: 201-217.

Henderson, C. B. (1976). "Drag Coefficients of Spheres in Continuum and Rarefied Flows." AIAA Journal **14**(6): 707-708.

Hinds, W. C. (2012). Aerosol Technology: Properties, Behavior, and Measurement of Airborne Particles, Wiley.

Hoey, J. M., A. Lutfurakhmanov, D. L. Schulz and I. S. Akhatov (2012). "A review on aerosol-based direct-write and its applications for microelectronics." Journal of Nanotechnology.

Hoffman, T., Z. C. Holman, M. Herrmann and M. Kozicki Nozzle Design for Vacuum Aerosol Deposition of Nanostructured Coatings. Nozzle Design for Vacuum Aerosol Deposition of Nanostructured Coatings, Arizona State University.

Huffman, J. A., J. T. Jayne, F. Drewnick, A. C. Aiken, T. Onasch, D. R. Worsnop and J. L. Jimenez (2005). "Design, modeling, optimization, and experimental tests of a particle beam

width probe for the Aerodyne aerosol mass spectrometer." Aerosol Science and Technology **39**(12): 1143-1163.

Hutchins, D. K., J. Holm and S. R. Addison (1991). "Electrodynamic focusing of charged aerosol particles." Aerosol Science and Technology **14**(4): 389-405.

Japuntich, D. A., J. I. T. Stenhouse and B. Y. H. Liu (1992). "An Aerosol Generator for High Concentrations of 0.5–5-μm Solid Particles of Practical Monodispersity." Aerosol Science and Technology **16**(4): 246-254.

Johnston, M. V. and D. E. Kerecman (2019). "Molecular Characterization of Atmospheric Organic Aerosol by Mass Spectrometry." Annual Review of Analytical Chemistry **12**(1): 247-274.

Kane, D. B., B. Oktem and M. V. Johnston (2001). "An electrostatic lens for focusing charged particles in a mass spectrometer." Aerosol Science & Technology **35**(6): 990-997.

Kievit, O., J. C. M. Marijnissen, P. J. T. Verheiljen and B. Scarlett (1992). "On-line measurement of particle size and composition." Journal of Aerosol Science **23**: 301-304.

Kim, H., J. Kim, H. J. Yang, J. Suh, T. Kim, B. W. Han, S. Kim, D. S. Kim, P. V. Pikhitsa and M. Choi (2006). "Parallel patterning of nanoparticles via electrodynamic focusing of charged aerosols." Nature Nanotechnology **1**(2): 117-121.

Kim, S.-G., B.-D. Hahn, D.-S. Park, Y.-C. Lee, E.-J. Choi, W.-S. Chae, D.-H. Baek and J.-Y. Choi (2011). "Aerosol Deposition of Hydroxyapatite and 4-Hexylresorcinol Coatings on Titanium Alloys for Dental Implants." Journal of Oral and Maxillofacial Surgery **69**(11): e354-e363.

Knoop, C., Z. Todorova, J. Tomas and U. Fritsching (2016). "Agglomerate fragmentation in high-intensity acoustic standing wave fields." Powder Technology **291**: 214-222.

Knutson, E. O. and K. T. Whitby (1975). "Aerosol classification by electric mobility: apparatus, theory, and applications." Journal of Aerosol Science **6**(6): 443-451.

KOUSAKA, Y., K. OKUYAMA, A. SHIMIZU and T. YOSHIDA (1979). "Dispersion mechanism of aggregate particles in air." Journal of Chemical Engineering of Japan **12**(2): 152-159.

Krinke, T. J., K. Deppert, M. H. Magnusson, F. Schmidt and H. Fissan (2002). "Microscopic aspects of the deposition of nanoparticles from the gas phase." Journal of Aerosol Science **33**(10): 1341-1359.

Ku, B. K. and J. F. de la Mora (2009). "Relation between Electrical Mobility, Mass, and Size for Nanodrops 1-6.5 nm in Diameter in Air." Aerosol Science and Technology **43**(3): 241-249.

Ku, N., C. Hare, M. Ghadiri, M. Murtagh, P. Oram and R. A. Haber (2015). "Auto-granulation of Fine Cohesive Powder by Mechanical Vibration." Procedia Engineering **102**: 72-80.

Langevin, P. (1903). Ann. Chim. Phys. **28**: 289.

Lebedev, M., J. Akedo, K. Mori and T. Eiju (2000). "Simple self-selective method of velocity measurement for particles in impact-based deposition." Journal of Vacuum Science & Technology A **18**(2): 563-566.

Lee, C., M.-Y. Cho, M. Kim, J. Jang, Y. Oh, K. Oh, S. Kim, B. Park, B. Kim, S.-M. Koo, J.-M. Oh and D. Lee (2019). "Applicability of Aerosol Deposition Process for flexible electronic device and determining the Film Formation Mechanism with Cushioning Effects." Scientific Reports **9**(1): 2166.

Lee, K.-S., S.-W. Cho and D. Lee (2008). "Development and experimental evaluation of aerodynamic lens as an aerosol inlet of single particle mass spectrometry." Journal of Aerosol Science **39**(4): 287-304.

Lee, K.-S., T.-H. Hwang, S.-H. Kim, S. H. Kim and D. Lee (2013). "Numerical simulations on aerodynamic focusing of particles in a wide size range of 30 nm–10 μm." Aerosol Science and Technology **47**(9): 1001-1008.

Lee, K.-S., S. Kim and D. Lee (2009). "Aerodynamic focusing of 5–50nm nanoparticles in air." Journal of Aerosol Science **40**(12): 1010-1018.

Lee, M. W., J. J. Park, D. Y. Kim, S. S. Yoon, H. Y. Kim, D. H. Kim, S. C. James, S. Chandra, T. Coyle, J. H. Ryu, W. H. Yoon and D. S. Park (2011). "Optimization of supersonic nozzle flow for titanium dioxide thin-film coating by aerosol deposition." Journal of Aerosol Science **42**(11): 771-780.

Li, C., N. Singh, A. Andrews, B. A. Olson, T. E. Schwartzentruber and C. J. Hogan (2019). "Mass, momentum, and energy transfer in supersonic aerosol deposition processes." International Journal of Heat and Mass Transfer **129**: 1161-1171.

Lima, R. S. and B. R. Marple (2007). "Thermal spray coatings engineered from nanostructured ceramic agglomerated powders for structural, thermal barrier and biomedical applications: a review." Journal of Thermal Spray Technology **16**(1): 40-63.

Lin, E.-C., J. J. Cole and H. O. Jacobs (2010). "Gas Phase Electrodeposition: A Programmable Multimaterial Deposition Method for Combinatorial Nanostructured Device Discovery." Nano Letters **10**(11): 4494-4500.

Linsebigler, A. L., G. Lu and J. T. Yates Jr (1995). "Photocatalysis on TiO2 surfaces: principles, mechanisms, and selected results." Chemical reviews **95**(3): 735-758.

Liu, P., P. J. Ziemann, D. B. Kittelson and P. H. McMurry (1995). "Generating Particle Beams of Controlled Dimensions and Divergence .1. Experimental Evaluation of Particle Motion in Aerodynamic Lenses and Nozzle Expansions." Aerosol Science and Technology **22**(3): 293-313.

Liu, P., P. J. Ziemann, D. B. Kittelson and P. H. McMurry (1995). "Generating Particle Beams of Controlled Dimensions and Divergence .2. Experimental Evaluation of Particle Motion in Aerodynamic Lenses and Nozzle Expansions." Aerosol Science and Technology **22**(3): 314-324.

Löndahl, J., W. Möller, J. H. Pagels, W. G. Kreyling, E. Swietlicki and O. Schmid (2014). "Measurement techniques for respiratory tract deposition of airborne nanoparticles: a critical review." Journal of aerosol medicine and pulmonary drug delivery **27**(4): 229-254.

Masuda, S., K. Fujibayashi, K. Ishida and H. Inaba (1972). "Confinement and transportation of charged aerosol clouds via electric curtain." Electrical Engineering in Japan **92**(1): 43-52.

Matsui, H., M. Ichihashi, S. Ueda, T. Otaka, K. Takahashi, T. Kobari and K. Odaka (1995). Charged particle beam apparatus including means for maintaining a vacuum seal, Google Patents.

Mazur, P. and I. Oppenheim (1970). "Molecular theory of brownian motion." Physica **50**(2): 241-258.

McMurry, P. H. (2000). "A review of atmospheric aerosol measurements." Atmospheric Environment **34**(12): 1959-1999.

Mihara, K., T. Hoshina, H. Kakemoto, H. Takeda and T. Tsurumi (2010). "Effects of Pretreatments on Deposition Rate of Films in Aerosol Deposition Method." Key Engineering Materials **421-422**: 165-168.

Murphy, W. K. and G. W. Sears (1964). "Production of Particulate Beams." Journal of Applied Physics **35**(6): 1986-1987.

Natarajan, C., N. Fukunaga and G. Nogami (1998). "Titanium dioxide thin film deposited by spray pyrolysis of aqueous solution." Thin Solid Films **322**(1): 6-8.

Oberreit, D. R. and C. J. Hogan Jr (2015). Drift tube ion mobility spectrometer for aerosol measurement, Google Patents.

Odenthal, C. J. (1991). Pinched electron beam cathode-ray tube with high-voltage einzel focus lens, Google Patents.

Pan, Y.-L., A. Kalume, C. Wang and J. L. Santarpia (2018). "Opto-aerodynamic focusing of aerosol particles." Aerosol Science and Technology **52**(1): 13-18.

Park, J.-J., D.-Y. Kim, J.-G. Lee, Y.-H. Cha, M. T. Swihart and S. S. Yoon (2014). "Supersonic aerosol-deposited TiO2 photoelectrodes for photoelectrochemical solar water splitting." RSC Advances **4**(17): 8661-8670.

Park, J.-J., J.-G. Lee, D.-Y. Kim, J.-H. Hong, J.-J. Kim, S. Hong and S. S. Yoon (2012). "Antibacterial and Water Purification Activities of Self-Assembled Honeycomb Structure of Aerosol Deposited Titania Film." Environmental Science & Technology **46**(22): 12510-12518.

Park, J.-J., M.-W. Lee, S. S. Yoon, H.-Y. Kim, S. C. James, S. D. Heister, S. Chandra, W.-H. Yoon, D.-S. Park and J. Ryu (2011). "Supersonic Nozzle Flow Simulations for Particle Coating Applications: Effects of Shockwaves, Nozzle Geometry, Ambient Pressure, and Substrate Location upon Flow Characteristics." Journal of Thermal Spray Technology **20**(3): 514-522.

Park, J., J. Jeong, C. Kim and J. Hwang (2013). "Deposition of Charged Aerosol Particles on a Substrate by Collimating Through an Electric Field Assisted Coaxial Flow Nozzle." Aerosol Science and Technology **47**(5): 512-519.

Perera, I. E. and C. D. Litton (2015). "Quantification of Optical and Physical Properties of Combustion-Generated Carbonaceous Aerosols (<PM(2.5))Using Analytical and Microscopic Techniques." Fire technology **51**(2): 247-269.

Pokharel, L., P. Parajuli, L. Li, E. J. Chng and R. Gopalakrishnan (2019). "An ultrasonic feeding mechanism for continuous aerosol generation from cohesive powders." Aerosol Science and Technology **53**(3): 321-331.

Prenni, A. J., R. L. Siefert, T. B. Onasch, M. A. Tolbert and P. J. Demott (2000). "Design and Characterization of a Fluidized Bed Aerosol Generator: A Source for Dry, Submicrometer Aerosol." Aerosol Science and Technology **32**(5): 465-481.

Qi, L., P. H. McMurry, D. J. Norris and S. L. Girshick (2010). "Micropattern deposition of colloidal semiconductor nanocrystals by aerodynamic focusing." Aerosol Science and Technology **44**(1): 55-60.

Ren-Jian, Z., H. Kin-Fai and S. Zhen-Xing (2012). "The Role of Aerosol in Climate Change, the Environment, and Human Health." Atmospheric and Oceanic Science Letters **5**(2): 156-161.

Robinson, A. (1956). "On the motion of small particles in a potential field of flow." Communications on Pure and Applied Mathematics **9**(1): 69-84.

Rusinque, H., E. Fedianina, A. Weber and G. Brenner (2019). "Numerical study of the controlled electrodeposition of charged nanoparticles in an electric field." Journal of Aerosol Science **129**: 28-39.

Ryu, J., B.-D. Hahn, J.-J. Choi, W.-H. Yoon, B.-K. Lee, J. H. Choi and D.-S. Park (2010). "Porous Photocatalytic TiO2 Thin Films by Aerosol Deposition." Journal of the American Ceramic Society **93**(1): 55-58.

Schmoll, L. H., S. Elzey, V. H. Grassian and P. T. O'Shaughnessy (2009). "Nanoparticle aerosol generation methods from bulk powders for inhalation exposure studies." Nanotoxicology **3**(4): 265-275.

Schreiner, J., U. Schild, C. Voigt and K. Mauersberger (1999). "Focusing of aerosols into a particle beam at pressures from 10 to 150 Torr " Aerosol Science and Technology **31**(5): 373-382.

Schreiner, J., C. Voigt, K. Mauersberger, P. McMurry and P. Ziemann (1998). "Aerodynamic lens system for producing particle beams at stratospheric pressures." Aerosol Science and Technology **29**(1): 50-56.

Schubert, M., D. Hanft, T. Nazarenus, J. Exner, M. Schubert, P. Nieke, P. Glosse, N. Leupold, J. Kita and R. Moos (2019). "Powder aerosol deposition method—novel applications in the field of sensing and energy technology." Functional Materials Letters **12**(5).

Seapan, M., D. Selman, F. Seale, G. Siebers and E. H. Wissler (1982). "Aerosol characterization using molecular beam techniques." Journal of Colloid and Interface Science **87**(1): 154-166.

Secor, E. B. (2018). "Principles of aerosol jet printing." Flexible and Printed Electronics **3**(3): 035002.

Sinha, M. P. and S. K. Friedlander (1986). "Mass distribution of chemical species in a polydisperse aerosol: Measurement of sodium chloride in particles by mass spectrometry." Journal of Colloid and Interface Science **112**(2): 573-582.

Swiderska-Kowalczyk, M., F. J. Gomez and M. Martin (1997). Particle generation methods applied in large-scale experiments on aerosol behaviour and source term studies. Spain**:** 112.

Tang, P., D. F. Fletcher, H. K. Chan and J. A. Raper (2008). "Simple and cost-effective powder disperser for aerosol particle size measurement." Powder Technology **187**(1): 27-36.

Thomson, B. A. and J. V. Iribarne (1979). "Field induced ion evaporation from liquid surfaces at atmospheric pressure." The Journal of Chemical Physics **71**(11): 4451-4463.

Tiwari, A. J., C. G. Fields and L. C. Marr (2013). "A Cost-Effective Method of Aerosolizing Dry Powdered Nanoparticles." Aerosol Science and Technology **47**(11): 1267-1275.

Tse, L. and K. Barton (2015). "Airflow assisted printhead for high-resolution electrohydrodynamic jet printing onto non-conductive and tilted surfaces." Applied Physics Letters **107**(5): 054103.

Tu, C., J. Lin, Z. Yin, F. Bao and P. Du (2017). "Powder disperser for the continuous aerosolizing of dry powdered nanoparticles." Advanced Powder Technology **28**(11): 2848-2858.

Varghese, O. K., D. Gong, M. Paulose, K. G. Ong and C. A. Grimes (2003). "Hydrogen sensing using titania nanotubes." Sensors and Actuators B: Chemical **93**(1-3): 338-344.

Verlet, L. (1967). "Computer "experiments" on classical fluids. I. Thermodynamical properties of Lennard-Jones molecules." Physical Review **159**(1): 98-103.

Wang, H.-L., C.-Y. Hsu, K. C. W. Wu, Y.-F. Lin and D.-H. Tsai (2020). "Functional nanostructured materials: Aerosol, aerogel, and de novo synthesis to emerging energy and environmental applications." Advanced Powder Technology **31**(1): 104-120.

Wang, X., F. E. Kruis and P. H. McMurry (2005). "Aerodynamic Focusing of Nanoparticles: I. Guidelines for Designing Aerodynamic Lenses for Nanoparticles." Aerosol Science and Technology **39**(7): 611-623.

Wang, X., C. Lee, P. Chen, C. Peng and P. Chang (2006). Microfabrication Process of PZT Thick Film by Aerosol Deposition Method. 2006 1st IEEE International Conference on Nano/Micro Engineered and Molecular Systems.

Weißbäcker, C. and H. Rose (2001). "Electrostatic correction of the chromatic and of the spherical aberration of charged-particle lenses." Journal of Electron Microscopy **50**(5): 383-390.

Wilkinson, N. J., M. A. A. Smith, R. W. Kay and R. A. Harris (2019). "A review of aerosol jet printing—a non-traditional hybrid process for micro-manufacturing." The International Journal of Advanced Manufacturing Technology **105**(11): 4599-4619.

Wu, Y., C. Tu, Z. Zhang, M. Yang, F. Bao and Z. Yin (2019). "Effect of divergence angle of ejector nozzle on aerosolisation of powdered nanoparticles." Molecular Simulation **45**(7): 556-563.

Yang, G.-J., C.-J. Li, F. Han, W.-Y. Li and A. Ohmori (2008). "Low temperature deposition and characterization of TiO2 photocatalytic film through cold spray." Applied Surface Science **254**(13): 3979-3982.

Yang, G.-J., K.-X. Liao, C.-J. Li, S.-Q. Fan, C.-X. Li and S. Li (2012). "Formation of Pore Structure and Its Influence on the Mass Transport Property of Vacuum Cold Sprayed TiO2 Coatings Using Strengthened Nanostructured Powder." Journal of Thermal Spray Technology **21**(3): 505-513.

You, S. and M. Choi (2007). "Numerical simulation of microscopic motion and deposition of nanoparticles via electrodynamic focusing." Journal of Aerosol Science **38**(11): 1140-1149.

You, S., K. Han, H. Kim, H. Lee, C. G. Woo, C. Jeong, W. Nam and M. Choi (2010). "Nanoparticle patterning: High-resolution, parallel patterning of nanoparticles via an ion-induced focusing mask." Small **6**(19).

Yuuki, K., Y. Uemichi, Y. Sato and S. Yoshikado (2013). "Evaluation of TiO2 Films Fabricated by Aerosol Deposition." Key Engineering Materials **566**: 195-198.

Zabihi Yeganeh, A., M. Jadidi, C. Moreau and A. Dolatabadi (2019). "Numerical modeling of aerosol deposition process." Surface and Coatings Technology **370**: 269-287.

Zhang, X., K. A. Smith, D. R. Worsnop, J. L. Jimenez, J. T. Jayne, C. E. Kolb, J. Morris and P. Davidovits (2004). "Numerical characterization of particle beam collimation: Part II Integrated aerodynamic-lens–nozzle system." Aerosol Science and Technology **38**(6): 619-638.

Zhou, M. and X. Ma (2009). "Efficient photoelectrocatalytic activity of TiO2/Ti anode fabricated by metalorganic chemical vapor deposition (MOCVD)." Electrochemistry Communications **11**(4): 921-924.

Zhou, Q. T., B. Armstrong, I. Larson, P. J. Stewart and D. A. V. Morton (2010). "Understanding the influence of powder flowability, fluidization and de-agglomeration characteristics on the aerosolization of pharmaceutical model powders." European Journal of Pharmaceutical Sciences **40**(5): 412-421.

Ziemann, P. J., D. B. Kittelson and P. H. McMurry (1995). "Generating Particle Beams of Controlled Dimensions and Divergence: I. Theory of Particle Motion in Aerodynamic Lenses and Nozzle Expansions AU - Liu, Peng." Aerosol Science and Technology **22**(3): 293-313.

Ziemann, P. J., D. B. Kittelson and P. H. McMurry (1995). "Generating Particle Beams of Controlled Dimensions and Divergence: II. Experimental Evaluation of Particle Motion in Aerodynamic Lenses and Nozzle Expansions AU - Liu, Peng." Aerosol Science and Technology **22**(3): 314-324.